Control of stoichiometry and observation of spin excitations in the S = 1/2 bilayer triangular lattice antiferromagnet LiZn2Mo3O8

PhD Thesis

Control of stoichiometry and observation of spin excitations in the $S = 1/2$ bilayer triangular lattice antiferromagnet $LiZn_2Mo_3O_8$

($S = 1/2$二層三角格子反強磁性体$LiZn_2Mo_3O_8$の化学量論比の制御とスピン励起の観測)

SANDVIK, Kim Eric Andreas

Department of Physics
Graduate School of Science
Tohoku University

2019

Control of stoichiometry and observation of spin excitations in the $S = 1/2$ bilayer triangular lattice antiferromagnet $LiZn_2Mo_3O_8$

Kim E. Sandvik[1]

[1] *Institute of Multidisciplinary Research for Advanced Materials, Tohoku University*

INTRODUCTION

Geometrically frustrated quantum magnetism is an intriguing topic in condensed matter physics that has attracted continuous interest for many decades [1]. In frustrated systems, such as triangular- or kagome-lattice antiferromagnets (TLAF or KLAF), because of the competing interactions, conventional magnetic long-range order was supposed to be strongly suppressed; in KLAF, several intriguing quantum disordered states are proposed theoretically, whereas recent study indicates that noncollinear 120° spin order may be realized even in the quantum limit ($S = 1/2$) for TLAF [2].

Recently the study on the frustrated magnetism has expanded to cluster magnetic compounds where the magnetic moment is delocalized over a group of atoms, called a cluster, instead of being localized on a single atom. Compared to single ion magnets, cluster magnets tend to have a lesser on-site Coulomb repulsion U, as the unpaired electron responsible for the magnetism may spread much widely, making cluster magnets also a platform to study Mott-insulator physics. One group of cluster magnets is the family of transition metal trimer compounds M_3X_8, (M = transition metal, X = anion). The pioneering compound of this group where geometric frustration was first studied is $LiZn_2Mo_3O_8$ (LZMO). This compound has magnetic Mo_3O_{13} clusters forming triangular lattice planes that are stacked with the layers of Li^+ and Zn^{2+} ions in between. Ideally, the total electronic configuration of the system is such that one unpaired electron will be localized on each Mo_3O_{13} cluster ($[Mo_3]^{11+}$, $S = 1/2$). The magnetic susceptibility on LZMO shows two distinct temperature ranges with two different moment sizes. With this fact together with the lack of magnetic order down to $T = 0.05$ K, it was inferred that an intriguing condensed valence-bond state is formed in LZMO at low temperatures [3].

If the compound certainly has the stoichiometry composition $LiZn_2Mo_3O_8$, then all the Mo_3O_{13} clusters will have $S = 1/2$ quantum spins, and hence this system may be an ideal quantum TLAF. However, LZMO has chemical disorder of Li and Zn atoms. This easily leads to off-stoichiometry that will introduce hole doping to Mo_3O_{13} resulting in non-magnetic clusters. Indeed, it was shown that the chemical compositions of the samples used in the earlier work may deviate from the ideal one even in their neutron diffraction results [3,4]. This casts serious doubts on the compositional reliability of the earlier work, and consequently to the condensed valence-bond state conjectured there as it totally relies on the formation of the ideal TLAF in this material.

In view of the above incomplete situation for the LZMO research, we have undertaken the thorough solid-state chemistry research to control the composition of the LZMO compound. Using the compositionally well-characterized samples prepared in this work, we have conducted various bulk magnetic property measurements. In addition, with the sample which has the composition closest to the stoichiometry, we have performed both polarized and unpolarized neutron scattering experiments. Those results strongly suggest that the true ground state of the ideal LZMO can be rather simple dimer singlets than the condensed valence-bond state conjectured earlier.

EXPERIMENTAL

The polycrystalline samples of different compositions $Li_{1+x}Zn_{2-y}Mo_3O_8$ were prepared by solid-state-reaction technique with improved reaction condition. Crystal structure and chemical compositions were investigated using the inductively coupled plasma atomic emission spectroscopy (ICP), x-ray powder diffraction (XPD) and neutron powder diffraction (NPD). Bulk properties were characterized by measuring high-field magnetization (IMR), electron-spin resonance (IMR), specific heat (ISSP), and magnetic susceptibility (IMRAM). Inelastic neutron scattering experiments were performed using the High Resolution Chopper spectrometer (HRC) at J-PARC, Polarized Neutron Triple-Axis spectrometer (PTAX) at HFIR, ORNL, and Hybrid Spectrometer (HYSPEC) at SNS, ORNL.

STOICHIOMETRY CONTROL OF LZMO

Condition for the solid-state-reaction for preparing LZMO was first revisited. Use of MoO_3 together with MoO_2 instead of just MoO_2 greatly reduces the secondary phase formation. The combined ICP-XPD-NPD characterization confirms the compositions of the primary and secondary phase, as well as the ratio of them, which has never been achieved in the earlier work. By this improvement, we could obtain samples with wide hole doping range $0.4 < p < 0.8$. We emphasize that $p = 0.78(15)$ is much closer to the ideal composition ($p = 1$) than the sample used in the earlier work ($p = 0.54(8)$ in our re-estimation).

MAGNETIZATION MEASUREMENT OF THE SERIES OF LZMO WITH DIFFERENT p

Shown in Fig. 1 is the result of the magnetic susceptibility measurements for almost all the samples prepared in the present work, ranging from $p = 0.42$ to $p = 0.78$. It can be seen that for $p < 0.6$ the inverse susceptibility exhibits two linear regions, *i.e.* the high temperature ($T > 150$ K) and low-temperature ($T < 100$ K) regions, being very similar behavior observed in the earlier work. On the other hand, when p becomes close to the unity (ideal value), clearly distinct behavior shows up in the high-temperature region around $T = 200$ K, which is a very broad peak with decreasing magnetic susceptibility for decreasing temperature (Fig.1 inset).

The temperature dependence of the magnetic susceptibility for the ideal composition can be well reproduced by assuming the three components: (i) lowest temperature upturn obeying the Curie law ($\chi \propto C/T$); (ii) weak upturn below $T \simeq 50$ K obeying Cuire-Weiss law ($\chi \propto C/(T-\Theta)$); (iii) broad peak behavior which can be well accounted for the dimer susceptibility ($\chi \propto 1/T\,(3 + e^{J'/T})^{-1}$). The above three-component model was also used for all the samples with different p; it satisfactorily reproduces the magnetic susceptibility and the (number) fractions for the

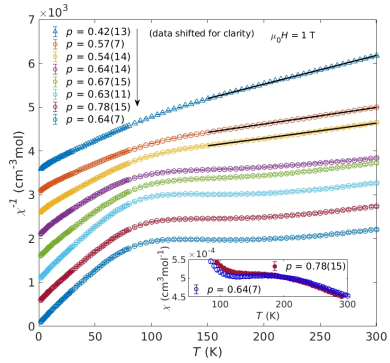

FIG. 1. Inverse magnetic susceptibility χ^{-1} of $LiZn_2Mo_3O_8$ samples with $0.42 \leq p \leq 0.78$. For $p < 0.6$ two Curie-Weiss temperature regions at $T < 100$ and $T > 150\,\mathrm{K}$ are shown as solid black lines. The inset shows magnetic susceptibility χ of samples $p = 0.78$ and $p = 0.64$ with a broad peak around $T = 200\,\mathrm{K}$.

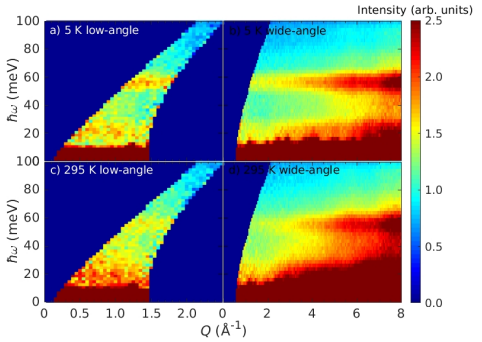

FIG. 2. Neutron scattering intensity at 5 K (a, b) and 295 K (c, d) obtained by incident neutron energy $E_i = 311$ meV using HRC low-angle (a, c) and wide-angle (b, d) detectors. All intensities have been normalized by proton count and have had background subtracted.

magnetic moments participating in the three components were estimated.

From the number fractions, we found that as the system becomes closer to the ideal composition, the fraction of the dimer components increases, whereas the other two components decrease. This strongly suggests that the intrinsic magnetism of LZMO is dimer formation, not the condensed valence-bond state as conjectured earlier. On the other hand, the two-temperature-region behavior reproduced in the samples with p away from unity is found to originate from the weakened dimer contribution, which accidentally forms linear inverse susceptibility in the high-T range.

In the thesis, we also discuss other bulk property measurements, such as high-magnetic-field magnetization, ESR and specific heat, which are mostly consistent with the above three-component model.

NEUTRON SCATTERING

Using the best composition sample ($p = 0.78$), we have performed several neutron scattering experiments. Fig. 2 shows overall neutron-inelastic-scattering spectra measured at $T = 5\,\mathrm{K}$ and $295\,\mathrm{K}$ using HRC. We have clearly observed enhancement of inelastic signal at $T = 5\,\mathrm{K}$ around $\hbar\omega \simeq 20$ meV in the low-Q region ($Q < 1$ Å^{-1}), where magnetic signal should be located due to the quickly decreasing magnetic form factor. In view of the temperature dependence, as well as its Q dependence, we believe the 20 meV peak is of magnetic origin. Furthermore, since the energy splitting is quite close to that estimated in the magnetic susceptibility study, this would be the singlet-triplet excitation from the dimers formed in the near-ideal LZMO compound.

We have also performed neutron scattering in the low-energy region, and the results are basically consistent with the three-component model; we have observed weakly correlating fluctuations in the low-energy region, which can be the same as those reported in the earlier neutron scattering study.

DISCUSSION

The dimer may be formed along the inter-layer c-direction, in striking contrast to the earlier conjecture of intra-layer dimers. The p dependence of the number fraction may be related to the probability of finding two $S = 1/2$ spins along the c-direction forming a dimer. Quantum chemistry calculation also suggests singlet-triplet excitation may be possible in a reasonable energy splitting (~ 10 meV). Hence, we now speculate that the dimers may be formed in the vertical direction, which is indeed, related to the bilayer nature of the crystal structure.

Nonetheless, detailed microscopic (electronic) understanding of the mechanism which makes inter-layer interaction much stronger than the intra-layer interaction is totally unclear, and further study to confirm the bilayer dimer formation is apparently necessary.

CONCLUSION

In this work, we found a method to improve the stoichiometry to $p = 0.78(15)$ in LZMO which is much closer to the ideal composition ($p = 1$) than the sample used in the earlier work. We found that the magnetic susceptibility of the off-stoichiometric LZMO can be explained by three different magnetic components. One of the components, dimer formation, seems to become dominant over the two other magnetic components as p is increased closer to the ideal value. This suggests that the intrinsic ground-state of the stoichiometric LZMO is dimer singlet formation instead of the condenced valence-bond state conjectured in earlier work. By using inelastic neutron scattering we observed magnetic excitations with energy splitting close to the singlet-triplet splitting energy estimated in the magnetic susceptibility.

REFERENCES

[1] L. Balents, Nature **464** (2010) 199−208.
[2] D. A. Huse, V. Elser, Phys. Rev. Lett. **60** (1988) 2531−2534.
[3] J. P. Sheckelton, J. R. Neilson, D. G. Soltan, T. M. McQueen, Nat. Mater. **11** (2012) 493496.
[4] J. P. Sheckelton, J. R. Neilson, T. M. McQueen, Mater. Horizons **2** (2015) 76−80.

PUBLISHED ARTICLES

[1] K. E. Sandvik, D. Okuyama, K. Nawa, M. Avdeev, T. J Sato, J. Solid State Chem. **271** (2019) 216−221.

Contents

1 Introduction

Generally, a many-body system shows a phase transition from a disordered to an ordered state by lowering temperature. One representative example is water; the gaseous phase (steam) condenses into the liquid phase (water) when the temperature is decreased. It transforms into the solid phase (ice) on further cooling. There are systems that do not order even at very low temperatures, ideally down to the absolute zero temperature, due to various reasons. One representative example is the one-dimensional spin chain in which because of very small number of nearest-neighbor bonds (indeed, only two) the system is supposed to fluctuate even at the base temperature. Higher-dimensional systems tends to order. However, in special cases where the pairwise interactions in the system cannot be simultaneously satisfied due to geometrical restrictions, an ordering is suppressed down to the base temperature. Such systems are now called "geometrically frustrated systems", and are the topic of the present study.

1.1 Geometrically frustrated $S = 1/2$ triangular lattice antiferromagnet

Geometrically frustrated quantum magnetism is an intriguing topic in condensed matter physics that has attracted continuous interest for many decades [1]. When spin magnetic moments are on geometrically frustrated lattices, where the antiferromagnetic pairwise interactions cannot be simultaneously satisfied, the ground states become macroscopically degenerated. The remaining entropy prohibits the system to establish long-range magnetic order down to the base temperature. When quantum fluctuations set in to such highly degenerated ground states, a highly entangled superposition of classically degenerated states may be formed as a quantum disordered ground state. Such a disordered ground state, or sometimes called quantum spin liquid (QSL) state, has been expected to be highly exotic, such as the putative resonating valence-bond (RVB) state. Furthermore, the quantum disordered ground state may host fractionalized excitations, such as $S = 1/2$

spinon excitations. It is at the heart of the modern condensed matter physics to find the putative QSL states and related fractionalized excitations.

The two-dimensional triangular lattice antiferromagnet (TLAF) with Ising spins was shown to lack magnetic ordering [2]. The $S = 1/2$ Heisenberg TLAF was thought to be a good candidate to study frustrated magnetism because the three key characteristics, *i.e.*, the low-dimensionality, geometrically frustrated lattice and non-classical spins are all included in the system [3]. However, after several theoretical studies [4–6], the consensus today is that the $S = 1/2$ TLAF shows the long-range magnetic order with the 120° spin structure. An illustration of this 120° structure is shown in Fig. 1.1

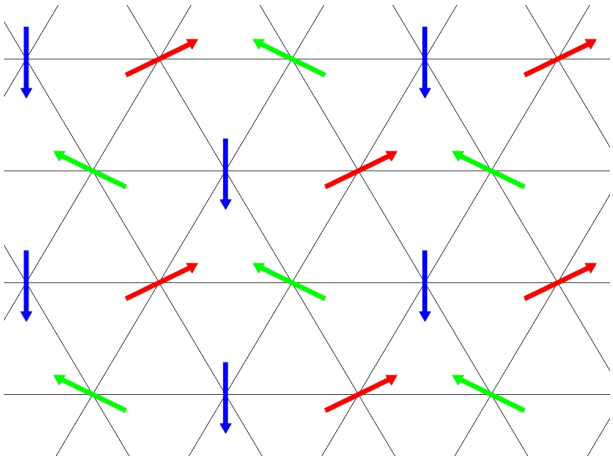

Figure 1.1: 120° spin structure. The red, green and blue arrows represent spin magnetic moments that are on the three different sub-lattices and that are aligned in a 120° angle to each other.

The magnetic ordering of the $S = 1/2$ TLAF can be destroyed allowing the formation of a quantum disordered state by adding perturbations to the system such as next-nearest-neighbor interactions [7], spatially anisotropic interactions [8] and random strength interactions [9]. Another perturbation is to bring the Hubbard U (on-site Coulomb potential) from the infinite limit to finite, allowing site-to-site charge hopping. Theoretical studies [10–12] predict a phase transition from the 120° structure to a non-magnetic insulating (NMI) phase at some finite U-value. This transition could also be into a spin liquid state [13] with a spinon Fermi surface [14, 15].

To access a smaller on-site Coulomb repulsion in order to have a good TLAF spin liquid candidate, one may use magnetic clusters instead of magnetic ions. Compared to magnetic ions, magnetic clusters tend to have smaller on-site Coulomb repulsion because the magnetic moment is delocalized over a group of atoms instead of being localized on a

single ion. Organic Mott insulators are one group of cluster magnets that are good TLAF spin liquid candidates, such as $\kappa-(BEDT-TTF)_2Cu_2(CN)_3$ [16].

Another group of TLAF cluster magnets is the family of transition-metal trimer compounds M_3X_8, (M = transition metal, X = O and Cl) [17–30]. Depending on the crystal structure and constituent ions, these compounds show a variety of ground states and magnetic behaviors. Notable members of the M_3X_8 family with an unpaired $S = 1/2$ per cluster are 1) $Li_2AMo_3O_8$ (A = In and Sc) [17–20], 2) $Na_3A_2(MoO_4)_2Mo_3O_8$ (A = In and Sc) [21], and 3) Nb_3Cl_8 [22, 23].

The first compound in the M_3X_8 family where geometrically frustrated magnetism was studied is $LiZn_2Mo_3O_8$ (LZMO) [25–30]. As the possible ground state, an intriguing condensed valence-bond (CVB) state was proposed [25] where two-thirds of the $S = 1/2$ condense below $T = 96\,K$ into a resonating-valence-bond state [3], while one-third of $S = 1/2$ remains paramagnetic. This compound will be the focus of this thesis.

1.2 Quantum triangular lattice antiferromagnet candidate $LiZn_2Mo_3O_8$

1.2.1 Earlier studies on $LiZn_2Mo_3O_8$

$LiZn_2Mo_3O_8$ compound has magnetic Mo_3O_{13} clusters forming triangular lattice planes that are stacked along the c-axis with the interspacing non-magnetic layers of Li^+ and Zn^{2+} ions (Fig. 1.2). Ideally, the total electronic configuration of the system is such that one unpaired electron will be localized on each Mo_3O_{13} cluster ($[Mo_3]^{11+}$, $S = 1/2$). If this condition is satisfied, then this system may be an ideal quantum triangular-lattice antiferromagnet (TLAF).

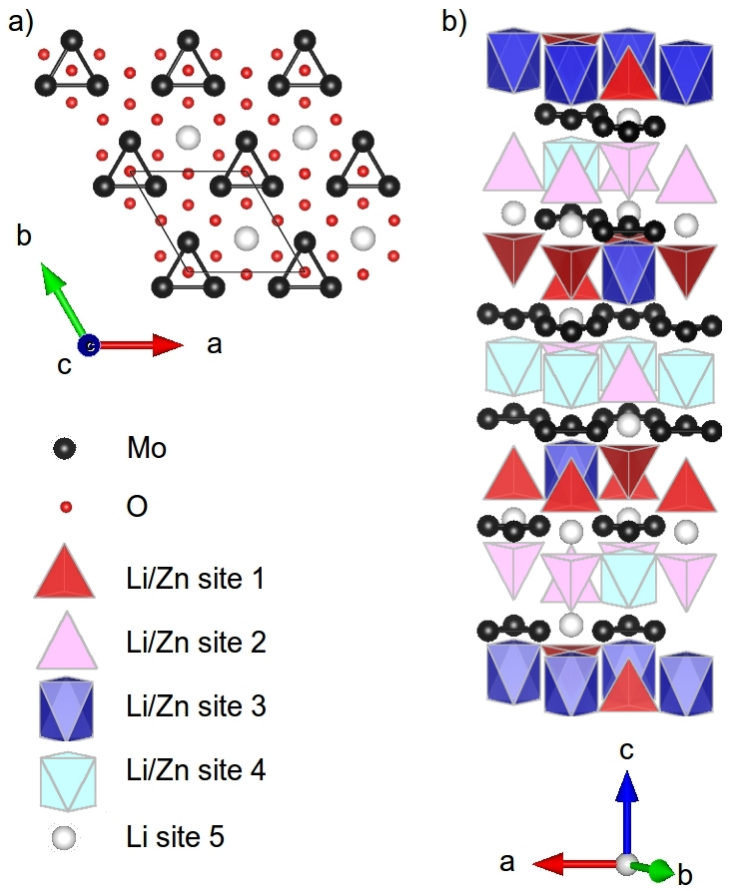

Figure 1.2: Crystal structure of $LiZn_2Mo_3O_8$ (space group $R\bar{3}m$ with $a = 5.8\,\text{Å}$ and $c = 31.1\,\text{Å}$). (a) Illustration of the triangular lattice in the ab plane. The thin black lines show the unit cell. Molybdenum sites in black are shown as clusters of three atoms aligned in ab plane. Oxygen sites are shown as red spheres. (b) The alternating stacking of the Mo_3O_8 triangular lattice layers and layers of Li/Zn atoms along the c-axis. Li and Zn sites $1 - 4$ have chemical disorder. Tetrahedral sites 1 and 2 in red and magenta, respectively, tend to be Zn rich while octahedral sites 3 and 4 in blue and cyan, respectively, tend to be Li rich. Li site 5 is presented in white in the Mo planes.

In the first paper by Sheckelton on LZMO [25], molecular orbital quantum chemistry calculations were performed, and the result supports that a single spin with spin quantum number $S = 1/2$ is delocalized among a totally symmetric (A_1 irreducible representation) orbital (Fig. 1.3(a)), which consists of a linear combination of molybdenum d-orbitals and oxygen p-orbitals. The calculation also predicts an on-site Hubbard $U \sim 1.2\,\text{eV}$. Experimentally, on the other hand, resistivity measurement indicates that LZMO is an electric insulator. All the results support the idea that the valence electrons remain contained within the Mo_3O_{13} clusters instead of being itinerant.

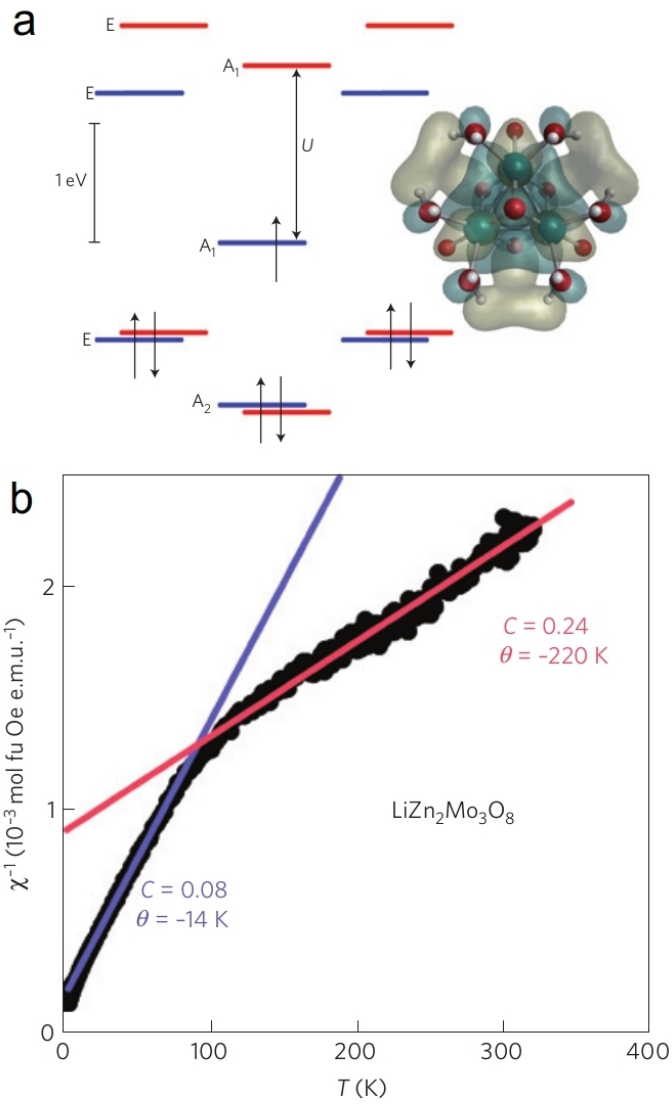

Figure 1.3: (a) A spin polarized molecular orbital diagram for $Mo_3O_{13}H_{15}$. There is one unpaired electron per cluster, distributed over all Mo atoms, with a large energy gap to the next available state. (b) Inverse magnetic susceptibility as a function of temperature in LZMO. Curie-Weiss fits to the two distinct linear portions are shown. Reprinted with permission from Ref. [25]. ©2012 Springer Nature.

The magnetic susceptibility of LZMO shows two distinct temperature ranges with approximately three times higher moment size in the higher temperature region compared to the lower temperature region (Fig. 1.3(b)). The heat capacity measured down to T = 0.05 K shows no evidence of long-range magnetic ordering which is also consistent with susceptibility (lowest T = 1.8 K), neutron powder diffraction (lowest T = 12 K) and resistivity measurements (lowest T = 50 K). The drastic disappearance of the two-thirds

of spins are indicative of the formation of spin singles, whereas the lack of magnetic long-range order indicates that the remaining one-third of spins are reasonably isolated. From these experimental results, an intriguing CVB state was inferred where two-thirds of spins form dynamical valence-bond states in which remaining minority fluctuating spins are embedded (see Fig. 1.4). As this CVB state is quite intriguing, shortly after the first report, many studies have been performed to confirm it, but its origin is still debated both theoretically and experimentally.

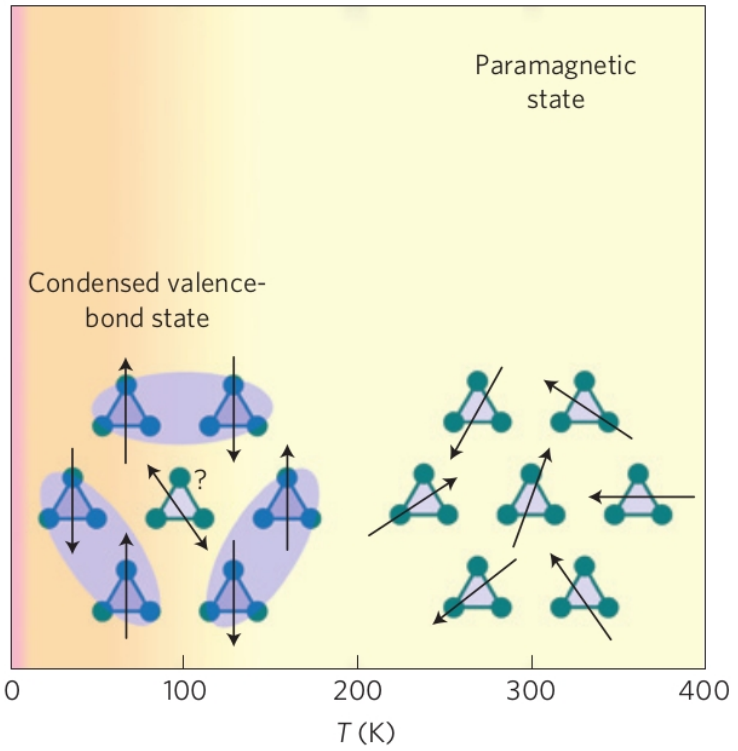

Figure 1.4: Illustration of the proposed CVB gound state. One-third of the spins are isolated and paramagnetic while two-thirds of the spins form dynamical singlets. At higher temperature the system enter a paramagnetic state. Reprinted with permission from Ref. [25]. ©2012 Springer Nature.

In order to study spin dynamics in LZMO microscopically, powder inelastic neutron scattering (INS) experiments were performed using Multi-Analyzer Crystal Spectrometer (MACS), installed at NIST Center for Neutron Research, National Institute of Standards and Technology, and the Wide Angular-Range Chopper Spectrometer (ARCS) installed at Spallation Neutron Source, Oak Ridge National Laboratory [27]. The former was used to study the low-energy spectrum (Fig. 1.5(a-c)) using $E_\mathrm{f} = 2.5$, 3.7, and 5.0 meV, and at $T \leq 30$ K, whereas the latter was used to study the high-energy spectrum using E_i

= 154 meV at $T = 1.7$, and 200 K (Fig. 1.5(d)). Apparently gapless ($\Delta < 0.2$ meV) and continuous spin excitations were observed at least up to 2.5 meV. Since its Q-dependence is compatible with the nearest- and next-nearest-neighbor path lengths between Mo_3O_{13} clusters (Fig. 1.5(c)), the low-energy gapless excitations were related to corresponding valence bonds possibly formed in the CVB state. In the high energy regime, the observed spectrum for LZMO is similar to that for the non-magnetic $Zn_2Mo_3O_8$. Thus, it was concluded that no magnetic excitations were observed (Fig. 1.5(d)).

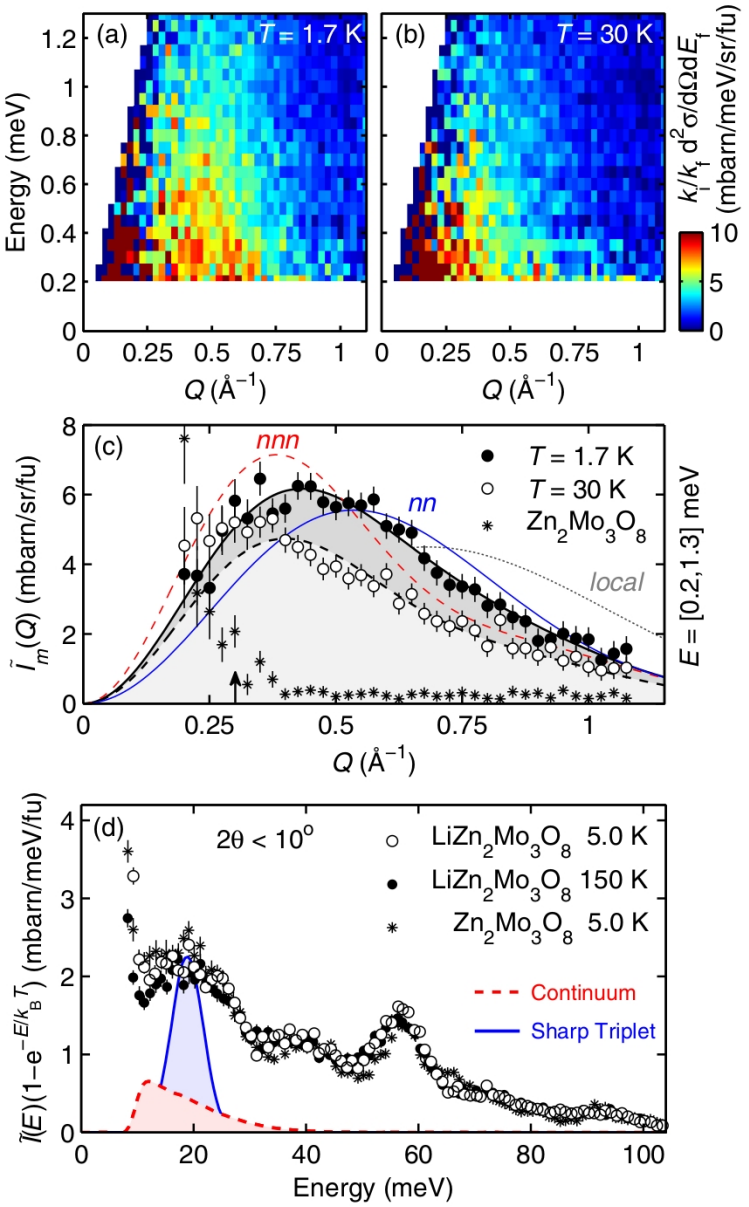

Figure 1.5: Inelastic neutron scattering spectra in LZMO at $E_f = 2.5$ meV at (a) $T = 1.7$ K and (b) $T = 30$ K corrected for the incoherent scattering by subtracting the non-magnetic $Zn_2Mo_3O_8$ incoherent scattering. (c) Momentum dependence of (a) and (b) integrated over $0.2 \leq E \leq 1.3$ meV compared to that of $Zn_2Mo_3O_8$ (integrated over $0.2 \leq E \leq 0.8$ meV). The fits are made to powder averaged valence bonds with different distances between the antiferromagnetically interacting spins. The dotted gray line, solid blue line and the red dashed line represent the intra molecular distance (2.6 Å), the nearest-neighbor (5.8 Å), and the next-nearest-neighbor molecular distance (10.0 Å), respectively. The actual fits are linear combinations of the next-nearest-neighbor and nearest-neighbor fits for $T = 1.7$ K and $T = 30$ K in solid black line and dashed black line, respectively. (d) Energy dependence of the neutron scattering intensity at $E_i = 154$ meV at low scattering angles ($2\theta < 10°$) in LZMO at 5 K (open circles) and 150 K (black circles), and $Zn_2Mo_3O_8$ at 5 K (black stars). The solid blue and dashed red lines are predictions for sharp triplet excitation and continuum, respectively. The integrated intensity is normalized by the Bose temperature factor. Reprinted with permission from Ref. [27]. ©2014 by the American Physical Society.

Electron spin resonance (ESR), ^{7}Li nuclear magnetic resonance (NMR), and muon spin rotation (μSR) (Fig. 1.6) spectroscopies were perfomed by Sheckelton [28]. As a representative result, the time dependence of μSR asymmetry is shown in Fig. 1.6 for $T = 120\,\mathrm{K}$, and $0.07\,\mathrm{K}$. There appears no significant difference between the two different temperatures. The μSR result clearly excludes the possibility of long-range magnetic order in LZMO down to $T = 0.07\,\mathrm{K}$. In addition, the similar relaxation behavior at the two temperatures suggests no significant change of spin fluctuation time scale in such a wide temperature range, which is puzzling behavior of this compound. The ESR result confirms that the magnetism of LZMO arises from the $S = 1/2$ spin with the g-factor being close to 2.

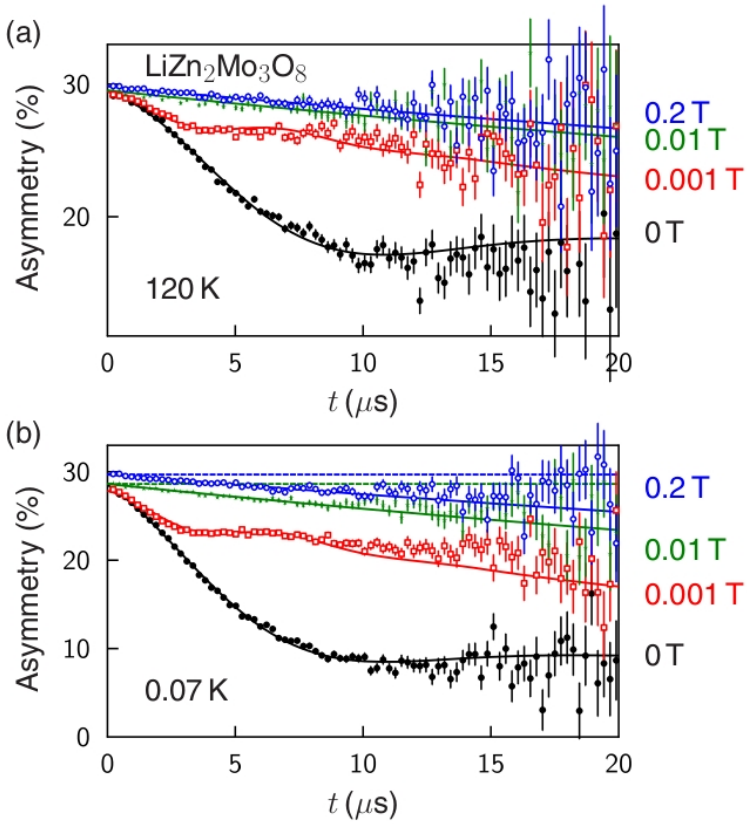

Figure 1.6: μSR asymmetry spectra in LZMO measured at (a) $T = 120\,\mathrm{K}$ and (b) $T = 0.07\,\mathrm{K}$ in zero field and various external magnetic fields. Reprinted with permission from Ref. [28].

It has been known from the beginning that this compound has significant chemical disorder in the interspacing Li/Zn sites. Hence, by controlling the ratio of the Li and Zn ions, which indeed have different valence states, hole doping may become possible to

the otherwise ideal $S = 1/2$ TLAF. Aiming at this point, Sheckelton performed the hole doping study by removing Zn^{2+} from the LZMO samples using the oxidizing agent I_2 [29]. In that study, it was claimed that the hole concentration is controlled from $[Mo_3O_{13}]^{12+}$ ($S = 0$) to $[Mo_3O_{13}]^{11+}$ ($S = 1/2$). It may be noted that no itinerant metallic state was induced by the hole doping. Instead, the two Curie-Weiss-regimes in the inverse magnetic susceptibility eventually merge into one regime as the hole doping increases. X-ray pair-distribution function analysis do not present any evidence of crystal lattice symmetry lowering in the hole doped LZMO samples.

1.2.2 Importance of chemical disorder in $LiZn_2Mo_3O_8$

In most of the experimental studies performed so far, LZMO has been assumed to be an ideal model $S = 1/2$ TLAF compound. That is, LZMO has fully occupied $S = 1/2$ spins on all the Mo_3O_{13} clusters. However, in the earlier studies it was known that due to the chemical disorder, the spin concentration per Mo_3O_{13} cluster (p, see Eq. 2.5 in Sect. 2.1.1) is far from the ideal value. In the first report [25], the chemical composition was estimated by neutron powder diffraction (NPD) as $Li_{1.2(1)}Zn_{1.8(1)}Mo_3O_8$. This composition corresponds to the spin concentration $p = 0.8(2)$, *i.e.*, 80% Mo_3O_{13} clusters are in the $S = 1/2$ state, and the remaining Mo_3O_{13} clusters are non-magnetic. It must be noted here that the Li and Zn compositions were apparently linearly constrained to 3.

In the later hole doping study [29], the authors reported much elaborate combination of NPD and synchrotron x-ray diffraction (SXRD). Shown in Fig. 1.7 are the resulting NPD and SXRD patterns together with their Rietveld profile fitting results. The fitting was satisfactorily performed, and the refined parameters are given in Table 1.1. From the site occupancy given in the table, one can estimate the chemical composition of the starting $LiZn_2Mo_3O_8$ used in the hole doping study to be $Li_{1.03(8)}Zn_{1.756(10)}Mo_3O_8$ in reality. The resulting spin concentration $p = 0.54(8)$ shows clearer departure from the ideal value ($p = 1$); indeed, 46% of Mo_3O_{13} clusters are non-magnetic.

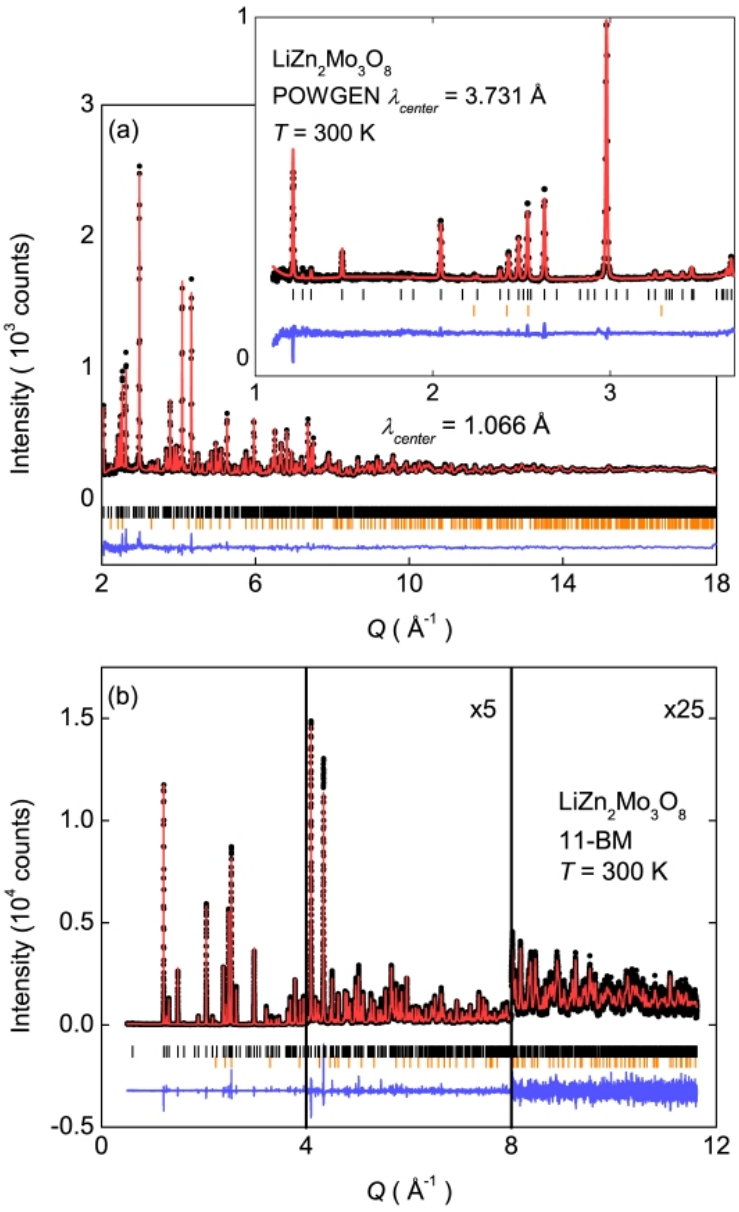

Figure 1.7: A combined Rietveld refinement of NPD (a) and SXRD (b) datasets on the undoped LZMO. Black dots are observed data, red line is Rietveld fit, blue line is the difference, black thick lines correspond to LZMO reflections in the $R\bar{3}m$ spacegroup, and orange lines are ZnO impurity reflections. Reprinted with permission from Ref. [29]. ©2015 by The Royal Society of Chemistry 2015.

Table 1.1: Atomic parameters of $Li_{1.0(1)}Zn_{1.8(1)}Mo_3O_8$ from combined SXRD/NPD Rietveld refinement at $T = 300\,K$. The space group is $R\bar{3}m$, Z is 6, the lattice constants are $a = 5.80163(3)\,Å$, and $c = 31.0738(2)\,Å$, and the global weighted χ^2 is 6.870. Reprinted with permission from Ref. [29].

Atom, i	Site	a_i/a	b_i/b	c_i/c	$U_{iso}(Å^2)$	occupancy
Mo1	18h	0.18504(8)	0.81496(8)	0.08393(4)	0.0016(2)	1
O1	18h	0.8445(2)	0.1555(2)	0.04850(6)	0.0017(3)	1
O2	18h	0.4920(2)	0.5080(2)	0.12438(7)	0.0047(4)	1
O3	6c	0	0	0.1185(1)	0.0054(7)	1
O4	6c	0	0	0.3715(1)	0.0053(6)	1
Zn1	6c	1/3	2/3	−0.64176(7)	0.0038(4)	0.879(6)
Li1	6c	1/3	2/3	−0.64176(7)	0.0038(4)	0.00(4)
Zn2	6c	0	0	0.1813(1)	0.0038(4)	0.679(5)
Li2	6c	0	0	0.1813(1)	0.0048(4)	0.22(4)
Zn3	3a	0	0	0	0.0038(4)	0.265(7)
Li3	3a	0	0	0	0.0038(4)	0.58(6)
Zn4	6c	0	0	0.5070(8)	0.0038(4)	0.065(4)
Li4	6c	0	0	0.5070(8)	0.0038(4)	0.43(3)
Li5	6c	2/3	1/3	0.08392(4)	0.0038(4)	0.09(3)

These earlier studies strongly suggest existence of partial deficiency of the $S = 1/2$ spins on the Mo_3O_{13} clusters. Hence, it is highly desired to revisit the magnetic study using the LZMO compound with much ideally tuned chemical composition.

1.2.3 Theoretical studies on $LiZn_2Mo_3O_8$

Since the putative CVB state is quite intriguing, several theoretical models have been proposed to explain it. Here, we will briefly summarize theoretical achievements so far made.

In 2013, Flint [26] proposed the mechanism of the disappearance of two-thirds of the spins in LZMO using the emergent honeycomb lattice model. In this theory three inequivalent sublattices of Mo_3O_{13} clusters is assumed. Clusters of the first and second sublattices turn in a finite angle around the c-axis clockwise and counterclockwise, respectively, while the third sublattice cluster is unchanged. This changes the bond lengths in such a manner that the spin exchange coupling becomes stronger between the first and second sublattices and weaker between the third and the other sublattices. This happens in a honeycomb pattern leaving one-third of the spins orphan just as in the CVS state.

In 2016, Chen [30] proposed a single band extended Hubbard model with 1/6 electron filling on an anisotropic kagome lattice to explain the low temperature phase in LZMO. The model Hamiltonian is presented as follows:

$$\hat{H} = \sum_{<i,j>\in \mathrm{u}} [-t_1(\hat{c}^{\dagger}_{i\sigma}\hat{c}_{j\sigma}+\mathrm{H.c.})+V_1\hat{n}_i\hat{n}_j] + \sum_{<i,j>\in \mathrm{d}} [-t_2(\hat{c}^{\dagger}_{i\sigma}\hat{c}_{j\sigma}+\mathrm{H.c.})+V_2\hat{n}_i\hat{n}_j] + \sum_i \frac{U}{2}(\hat{n}_i-\frac{1}{2})^2, \tag{1.1}$$

where definitions of t_1 ,V_1, t_2, and V_2 are given in Fig. 1.8. $\hat{n}_i = \sum_\sigma \hat{c}^{\dagger}_{i\sigma}\hat{c}_{i\sigma}$ is the electron occupation number at site i. Since there exists only one unpaired electron in each kagome lattice unit cell, the electron filling for this Hubbard model is 1/6. Intersite repulsive interactions were necessary to keep the electrons localized on clusters rather than on lattice sites. A parameter λ to describe the anisotropy of the kagome lattice was introduced as the ratio of the distance of Mo atoms in the down-pointing triangles ("d") between the distance of Mo atoms in the up-pointing triangles ("u"):

$$\lambda = \frac{[\mathrm{Mo}-\mathrm{Mo}]_{\mathrm{d}}}{[\mathrm{Mo}-\mathrm{Mo}]_{\mathrm{u}}}. \tag{1.2}$$

Large anisotropy tends to make a single electron to be localized on a single up triangle (Fig. 1.8(a)) while allowing the electron count to fluctuate heavily on the down triangles by decreasing the parameters t_2 and V_2 and increasing the parameters t_1 and V_1. Likewise, small anisotropy tends to make the electron count of both the up and down triangle to be one. Thus, the only degree of freedom for the charge fluctuation is a collective tunneling. This can induce a long-range plaquette charge order (PCO) (Fig. 1.8(b)). The explanation for the two Curie-Weiss regimes is that the lowest spinon band in this PCO model is slit to three sub-bands and 2/3 of the spinons occupy the lowest of these sub-bands thus being inert to an external field. The second and third sub-bands are partially occupied by the remaining 1/3 spinons which makes them active to an external field. With increasing thermal fluctuations the PCO is destroyed allowing all the spinons to be active to an external magnetic field. In the weak Mott regime the ground state is expected to be the U(1) quantum spin liquid with spinon Fermi surface.

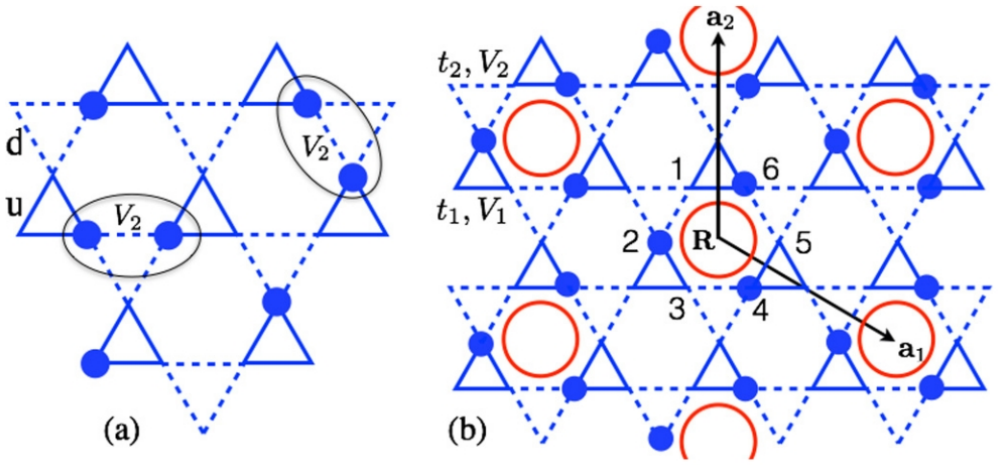

Figure 1.8: (a) The electron configuration in the cluster Mott insulator without the PCO when $V_2 \ll t_1$ and $V_1 \gg t_2$. (b) The electron configuration in the cluster Mott insulator with the PCO. Three electrons hop resonantly in each hexagon that is marked by a red circle. These marked hexagons form an emergenet $\sqrt{3} \times \sqrt{3}$ extended triangular lattice with lattice vectors $\mathbf{a}_1$, $\mathbf{a}_2$. Reprinted with permission from Ref. [30]. ©2016 by the American Physical Society.

1.2.4 $Li_2AMo_3O_8$ (A = In, and Sc)

The compounds $Li_2InMo_3O_8$ and $Li_2ScMo_3O_8$ have the same Mo_3O_{13} cluster with $S = 1/2$ in the same triangular lattice structure as LZMO. On the other hand, the stacking of the triangular lattices and cations are different resulting in the different space group ($P6_3mc$ #186) (Fig. 1.9). The compounds $Li_2AMo_3O_8$ (A = In, and Sc) lack chemical disorder which might make them a more ideal platform to study intrinsic magnetism of the TLAF compared to LZMO.

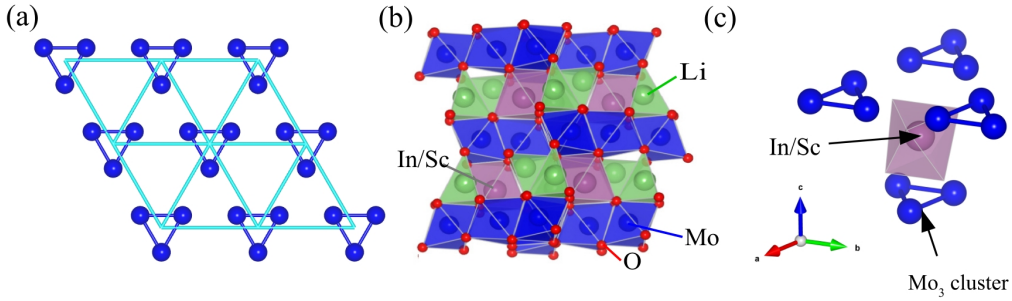

Figure 1.9: Structure of $Li_2AMo_3O_8$ (A = In, and Sc). (a) $[Mo_3]^{11+}$ trimers forming a triangular lattice. (b) Crystal structure of $Li_2AMo_3O_8$ viewed along the b-axis. (c) Coordination of Mo_3 clusters around the In/Sc ion. Reprinted from Ref. [31] (a, c) licensed under CC BY 3.0 (https://creativecommons.org/licenses/by/3.0/). Reprinted with permission from Ref. [17] (b). ©2015 by the American Physical Society.

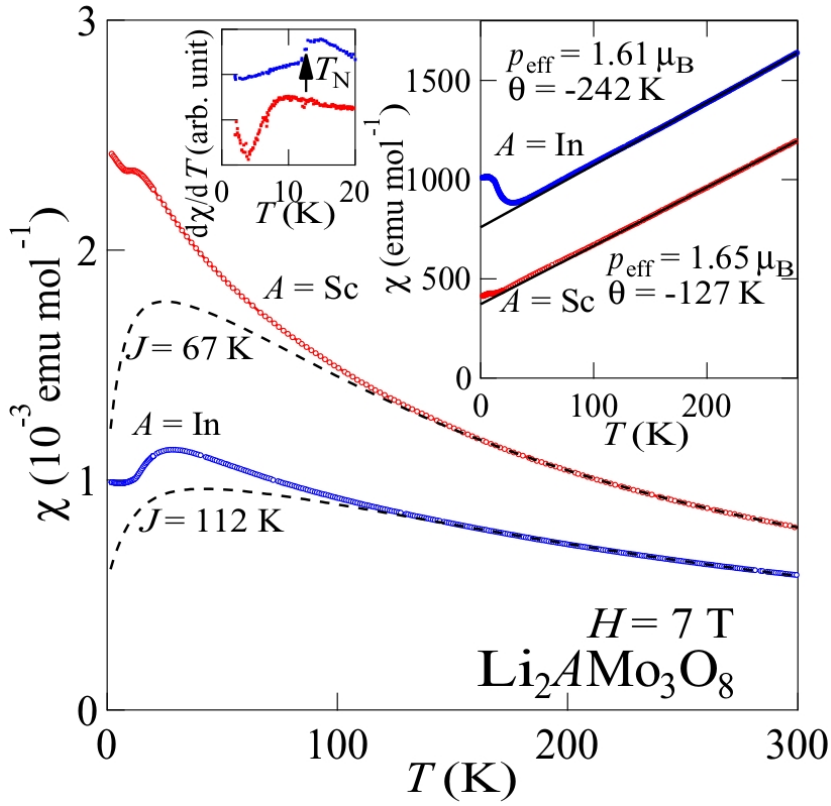

Figure 1.10: Magnetic susceptibility of $Li_2AMo_3O_8$, A = In and A = Sc presented in blue markers and red markers, respectively. The applied external magnetic field is 7 T. The dashed lines show the result using high-temperature series expansions of the $S = 1/2$ Heisenberg triangular lattice model with the exchange interaction of $J = 112$ and 67 K for A = In and A = Sc, respectively. The right inset shows the inverse magnetic susceptibility. The left inset shows the temperature derivative of the magnetic susceptibility in the low temperature region indicating a discontinuity for A = In at T_N. Reprinted with permission from Ref. [17]. ©2015 by the American Physical Society.

Magnetic properties of $Li_2AMo_3O_8$ (A = In, and Sc) were investigated by Haraguchi [17]. $Li_2InMo_3O_8$ shows magnetic ordering at $T_N \sim 12$ K with the ordered 120° spin structure. On the other hand, no magnetic ordering was observed down to 0.5 K in $Li_2ScMo_3O_8$. The magnetic susceptibility of both the compounds lacks an apparent low temperature Curie upterm. Fitted to the high temperature series expansions for the $S = 1/2$ Heisenberg TLAF, the exchange interactions were estimated as $J = 112$ K and 67 K for $Li_2InMo_3O_8$ and $Li_2ScMo_3O_8$, respectively (Fig. 1.10). The ^{7}Li NMR measurements were also performed. The NMR spectra, as well as the spin-lattice relaxation rate ($1/T_1$), provide direct microscopic evidence of the disordered ground state in $Li_2ScMo_3O_8$.

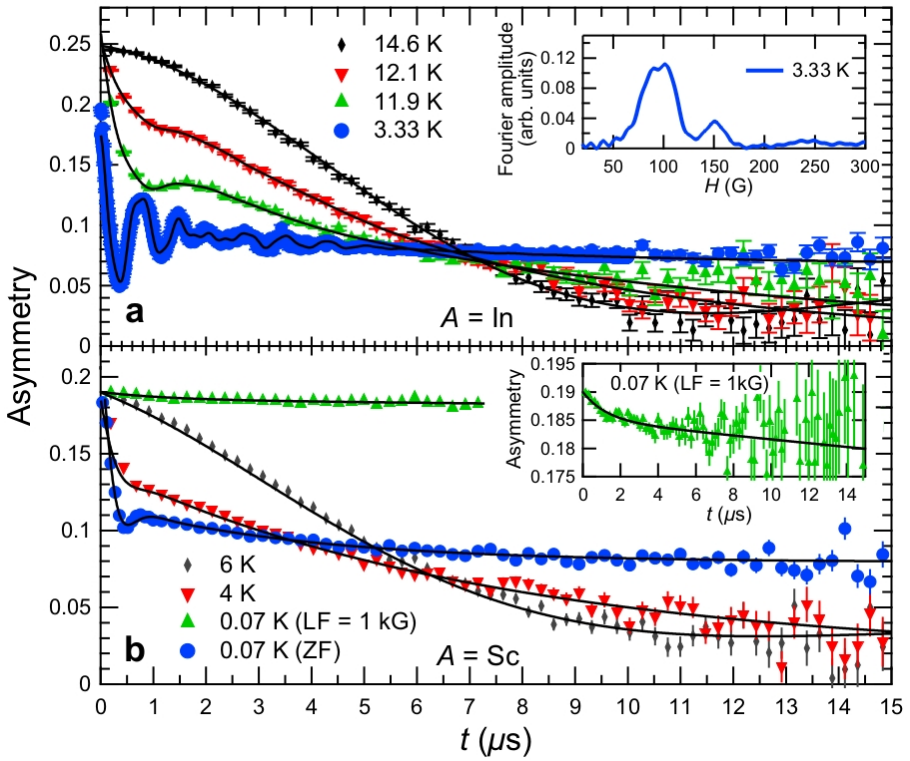

Figure 1.11: Time dependence of the μSR asymmetry in $Li_2AMo_3O_8$ (A = In, and Sc) for (a) A = In at zero field and for (b) A = Sc at both zero and longitudinal field (LF = 1 kG). (a) The spectra shows a damping around $T = 12$ K. The inset shows a Fourier transform of the time dependent signal showing three local magnetic fields at 84.9(3), 103.1(2), and 151.5(5) G at $T = 3.3$ K. (b) The spectra show a damping at $T = 4$ K. The inset shows a magnified view of the spectrum at $T = 0.07$ K under $H_{LF} = 1$ kG. Reprinted from Ref. [20] licensed under CC BY 4.0 (https://creativecommons.org/licenses/by/4.0/).

As for the microscopic understanding of magnetism, INS and μSR experiments were performed on $Li_2AMo_3O_8$ (A = In, and Sc) polycrystalline samples by Iida [20]. The μSR and INS results are shown in Figs. 1.11 and 1.12, respectively. $Li_2InMo_3O_8$ shows spinwave excitations which can be well reproduced by a model Hamiltonian consisting of the nearest-neighbor anisotropic exchange interactions, as well as assuming the 120° structure as a ground state. On the other hand, quantum-spin-liquid-like magnetic fluctuations was observed in $Li_2ScMo_3O_8$ characterized by the development of the short-range magnetic order below 4 K.

The electron doping dependence of magnetic properties in $Li_2Sc_{1-x}Sn_xMo_3O_8$ was studied by Haraguchi [18]. The increasing of Sn would introduce non-magnetic $[Mo_3]^{10+}$ trimers ($S = 0$) instead of the $[Mo_3]^{11+}$ trimers ($S = 1/2$). At all the doping levels, the system does not show magnetic ordering. The partial spin disappearing behavior (Fig. 1.13) is

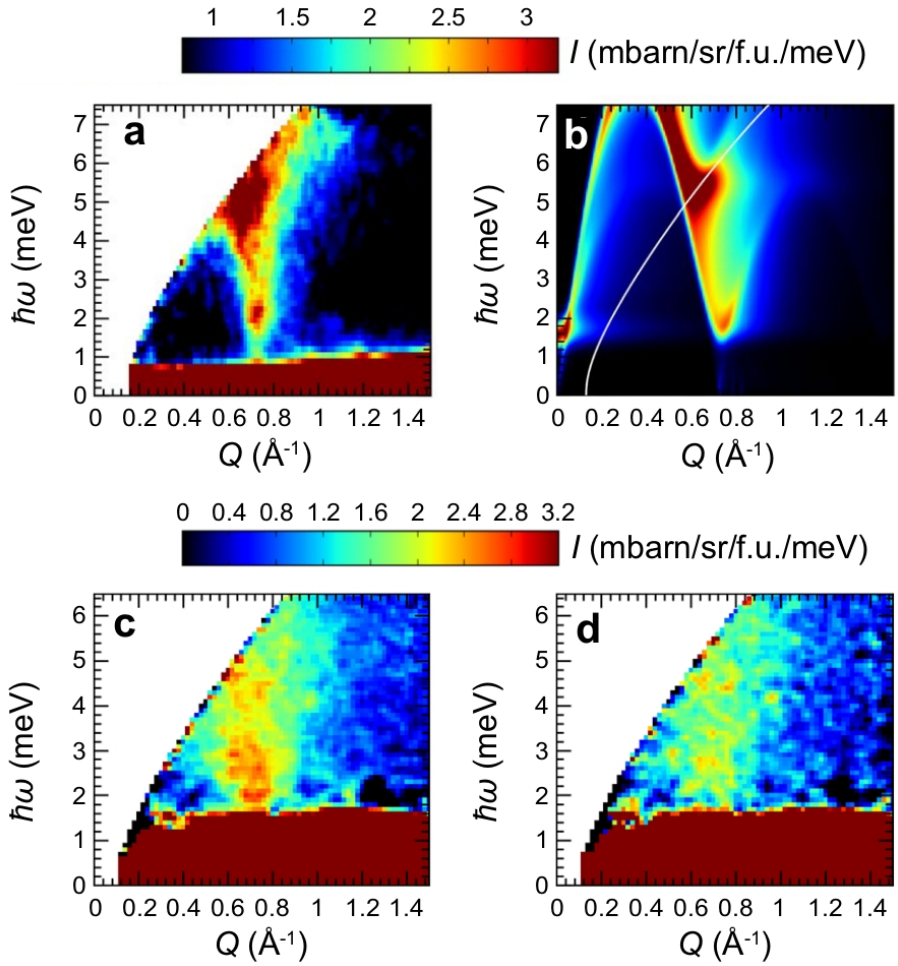

Figure 1.12: Low energy INS cross section of $Li_2AMo_3O_8$ taken by the 4SEASONS time-of-flight spectrometer at MLF, J-PARC for A = In (a) measured at $E_i = 11.9$ meV and $T = 4.6$ K and for A = Sc (c,d) measured at $E_i = 10.3$ meV and $T = 0.3$ K (c) and $T = 22$ K (d). (b) Calculated inelastic neutron scattering cross section at $E_i = 11.9$ meV and $T = 4.6$ K using a model consisting of the nearest-neighbor anisotropic exchange interactions. Reprinted from Ref. [20] licensed under CC BY 4.0 (https://creativecommons.org/licenses/by/4.0/).

found in all the Sn-substituted compounds except $x = 0$ which is also the case for LZMO. The partial spin disappearance was explained by a formation of the valence bond glass possibly stabilized by the randomness effect [9].

Doping dependence study was further performed with different dopant elements as $Li_2In_{1-x}Sc_xMo_3O_8$ by Akbari-Sharbaf [19]. This In to Sc substitution introduces neither electron nor hole doping but generates chemical pressure in an intriguing manner. Indeed, in this work, the nonmonotonic change of breathing parameter (*i.e.* ratio of the edge lengths of the large and small triangles in Fig. 1.14) was reported as In is replaced with

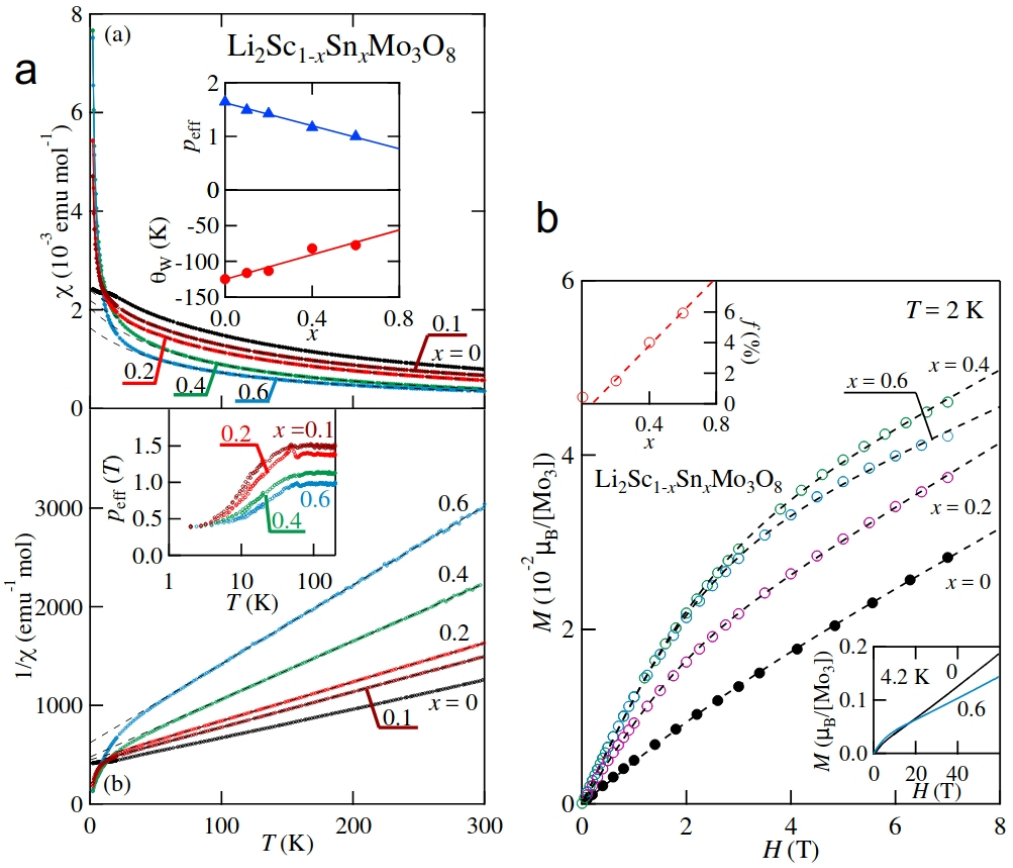

Figure 1.13: (a) The non-inverse and inverse magnetic susceptibility of $Li_2Sc_{1-x}Sn_xMo_3O_8$. The upper inset shows the composition dependence of the effective magnetic moment size and the Curie-Weiss temperatures estimated in the high-temperature region. The lower inset shows the temperature dependence of the size of the normalized effective magnetic moment. (b) The isothermal field dependent magnetization of $Li_2Sc_{1-x}Sn_xMo_3O_8$ at $T = 2\,K$ shown as circles. The fit shown as dashed lines involves a model with contribution from two components: nearly free spins and singlet forming spins. The upper inset shows the percentage of free spins. The lower inset shows the isothermal magnetization up to $H = 60\,T$ at $T = 4.2\,K$ for $x = 0$ and $x = 0.6$. Reprinted from Ref. [18] licensed under CC BY 3.0 (https://creativecommons.org/licenses/by/3.0/).

Sc. The chemical pressure also brings the system away from antiferromagnetic long range order ($x = 0$) with an introduction of a mixture of frozen and dynamic components of spins, as was indicated in the zero field μSR measurements (see Fig. 1.15 for μSR results). The $x = 0.6$ compound shows the smallest breathing parameter being the most closest to the symmetric kagome lattice. At this composition $x = 0.6$, the frozen component was not observed, in striking contrast to the samples with other compositions. It is noteworthy that the μSR asymmetry profile for the $x = 0.6$ sample is very similar to that of LZMO reported in [28]. Furthermore, all the compounds in the range $0.4 \leq x \leq 0.8$

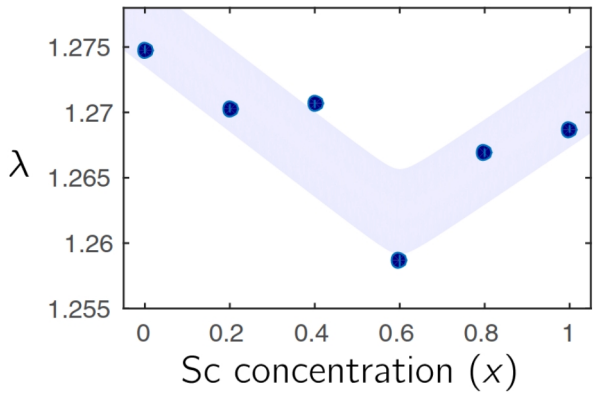

Figure 1.14: Anisotropy or breathing parameter λ as a function of x in $Li_2In_{1-x}Sc_xMo_3O_8$. The shaded region is a guide to the eye. Reprinted with permission from Ref. [19]. ©2018 by the American Physical Society.

show two Curie-Weiss regions as was the case in LZMO. From these two similarities, a strong relation between the magnetic ground states in the two different compounds ($Li_2In_{1-x}Sc_xMo_3O_8$ at $x = 0.6$ and LZMO) was suggested. It was further argued that the disappearance of the two-thirds of the spins in $Li_2In_{1-x}Sc_xMo_3O_8$ at $x = 0.6$ and LZMO may be commonly understood using the PCO model with strong PCO regime [30]. In this regime, a single resonating hexagon with three coupled spins with $S_{\mathrm{tot}} = 1/2$ and $S_{\mathrm{tot}} = 3/2$ as the ground and excited states, respectively, may be the origin for the low temperature magnetism. Along this line, an exellent fit to the magnetic susceptibilities of the compounds $0.4 \leq x \leq 0.8$ as well as LZMO in Ref. [25] was made using the localized resonating hexagon model with the trimer gap Δ and Weiss temperature θ_{W} as adjustable parameters.

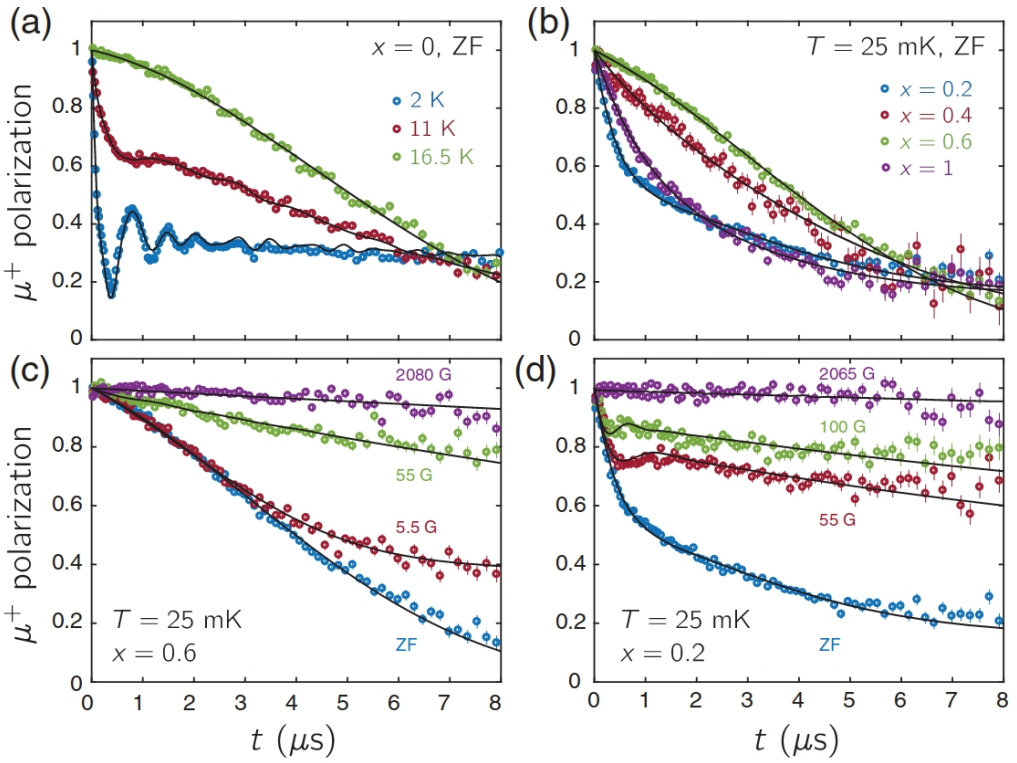

Figure 1.15: Zero field μSR polarization in $Li_2In_{1-x}Sc_xMo_3O_8$ for (a) $x = 0$ and for (b) other values of x at $T = 25$ mK. Longitudinal field measurements for (c) $x = 0.6$ and (d) $x = 0.2$. Reprinted with permission from Ref. [19]. ©2018 by the American Physical Society.

1.3 Aims of the present study

As summrized in this chapter, LZMO was proposed to form the condensed valence-bond ground state at low temperatures; it lacks the long-range magnetic ordering down to $T = 0.05\,\mathrm{K}$. At low temperatures, the number of spins estimated from the bulk magnetic susceptibility decreases significantly to one-third of the high temperature value [25]. Two theoretical explanations for the condensed valence-bond state were proposed: an emergent honeycomb lattice model involving three sub-lattices [26] and a 1/6-filled extended Hubbard model in an anisotropic kagome lattice that stabilizes a plaquette charge order [30, 32, 33]. From a hole doping dependence study by chemically removing Zn from the sample, it is concluded that no metallic state is induced at all the doping levels, while the primary effect of the hole doping is to decrease the number spins participating in the condensed valence-bond state [29].

If the compound certainly has the stoichiometry composition $LiZn_2Mo_3O_8$, then all Mo_3O_{13} clusters will have $S = 1/2$ quantum spins, and hence the system may be an ideal quantum TLAF. However, chemical disorder of Li and Zn atoms in shared Li/Zn sites easily leads to offstoichiometry. This will introduce non-magnetic $[Mo_3O_{13}]^{12+}$ $(S = 0)$ clusters that will reduce the number of magnetic $[Mo_3O_{13}]^{11+}$ clusters $(S = 1/2)$ from the ideal value. It is noteworthy that even in the earlier work, NPD/SXRD combined Rietveld refinement [29] of undoped sample clearly indicates that the number of magnetic $(S = 1/2)$ clusters is less than 60%. This possibly supports that the chemical compositions of earlier works deviate from the ideal value, casting serious doubts on the compositional reliability of the earlier works. This consequently suggests that the condensed valence-bond state conjectured there may not be the intrinsic ground state of the stoichiometric LZMO, as it totally relies on the formation of the ideal TLAF in this material.

In the view of the above incomplete situation for the research on $LiZn_2Mo_3O_8$, we have undertaken the thorough solid-state chemistry research to control the Li and Zn composition. By achieving the stoichiometry control by solid-state-reaction we study the doping dependence of the magnetism of $LiZn_2Mo_3O_8$ in the composition range much closer to the ideal stoichiometry compared to earlier works. This will also allow us to tune the composition as close to the stoichiometry as possible which might help to shed light on the intrinsic ground state of $LiZn_2Mo_3O_8$. Using the best possible sample we will also perform inelastic neutron scattering in the hope to observe the intrinsic excited state.

In this work, we first report the improved method of preparing the polycrystalline samples of different compositions $Li_{1+x}Zn_{2-y}Mo_3O_8$. Crystal structure and chemical compositions

were investigated using the inductively coupled plasma atomic emission spectroscopy (ICP), x-ray powder diffraction (XPD) and neutron powder diffraction (NPD). Bulk properties were characterized by measuring high-field magnetization, electron-spin resonance (ESR), specific heat, and magnetic susceptibility. Inelastic neutron scattering experiments were performed using High Resolution Chopper spectrometer (HRC) at J-PARC, Polarized Triple-Axis Spectrometer (PTAX) at HFIR, ORNL, and Hybrid Spectrometer (HYSPEC) at SNS, ORNL.

The main finding of this work is that the magnetism of $LiZn_2Mo_3O_8$ can be modelled with three components, *i.e.*, free paramagnetic spins, spins obeying the Curie-Weiss law with $\theta < -20\,\mathrm{K}$, and isolated spin dimers with exchange constant of $J/k_\mathrm{B} \sim 400\,\mathrm{K}$. When the Li and Zn composition becomes closest to the stoichiometry, the dimer component becomes dominant compared to the other components. This suggests that the true ground state of the ideal $LiZn_2Mo_3O_8$ might be rather simple dimer singlets than the condensed valence-bond state conjectured earlier.

The layout of the thesis is the following. Chapter 2 describes the experimental details used in the present study. Chapter 3 provides experimental results, and are divided into three parts. In Chapter 3.1, stoichiometry control of $Li_{1+x}Zn_{2-y}Mo_3O_8$ will be described, while in Chapter 3.2 magnetic measurements of the series of $Li_{1+x}Zn_{2-y}Mo_3O_8$ with different compositions will be explained. In Chapter. 3.3 the neutron scattering result of the best composition $Li_{1+x}Zn_{2-y}Mo_3O_8$ will be described. This will be followed by the discussion in chapter 4. The conclusions will be given in Chapter 5.

2 Experimental Details

This chapter explains the experimental methods used in this work. There are four subsections: first subsection deals with the sample preparation, second subsection with crystal structure and elemental composition characterization, third subsection with bulk magnetization, specific heat, and electron spin resonance measurements and forth subsection with inelastic neutron scattering measurements.

2.1 Polycrystalline $Li_{1+x}Zn_{2-y}Mo_3O_8$ synthesis

Polycrystalline samples of $Li_{1+x}Zn_{2-y}Mo_3O_8$ were prepared by modifying the previously reported solid-state-reaction method [25]. The starting ingredients are Li_2MoO_4 (99+%), ZnO (99.9%), MoO_2 (99.9+%), MoO_3 (99.9+%) and Mo (99.9%). Three different procedures in the solid-state-reaction procedure were tried in the present study. In the following they are referred to as *procedure Ref* (almost the same procedure as reported in Ref. [25]), *procedure A*, and *procedure B*. Assuming that the occupancy of the disordered Li and Zn sites could be controlled by increasing Li_2MoO_4 while decreasing ZnO, we varied the nominal composition as:

$$\mathrm{Li} : \mathrm{Zn} : \mathrm{Mo} : \mathrm{O} = 1 + w : 2.8 - w : 3 : 8.6 + \sigma, \tag{2.1}$$

where $w = 0.4$ and $\sigma = 0$ (*procedure Ref*), $-0.3 \leq w \leq 0.3$ and $\sigma = 0$ (*procedure A*) or $-0.45 \leq w \leq -0.2$ and $\sigma = 0.175$ (*procedure B*). The molar ratio of the starting chemicals in terms of w are listed below. For *procedure A*:

$$
\begin{aligned}
n(\mathrm{Li_2MoO_4}) &= \frac{1}{2}(1+w), \\
n(\mathrm{ZnO}) &= 2.8 - w, \\
n(\mathrm{MoO_2}) &= \frac{1}{4}(3.8-w), \\
n(\mathrm{MoO_3}) &= \frac{1}{6}(3.8-w), \\
n(\mathrm{Mo}) &= \frac{1}{12}(11-w).
\end{aligned} \tag{2.2}
$$

The ratio for *procedure B* is:

$$
\begin{aligned}
n(\mathrm{Li_2MoO_4}) &= \frac{1}{2}(1+w), \\
n(\mathrm{ZnO}) &= 2.8 - w, \\
n(\mathrm{MoO_2}) &= \frac{1}{2}(3.975-w), \\
n(\mathrm{Mo}) &= 0.5125.
\end{aligned} \tag{2.3}
$$

A mixture of the Li_2MoO_4, ZnO, MoO_2, and Mo powders with the above molar ratio was used as the initial material for the solid-state-reaction for *procedure Ref* and *procedure B*. For *procedure A*, MoO_3 is additionally used with a molar ratio of MoO_2:MoO_3 = 3:2, in addition to the Li_2MoO_4, ZnO, and Mo. MoO_3 was not used in the original method [25]. However, we found that when Zn is increased (while Li is decreased) in the starting composition by reducing the w parameter, an increasing amount of non-magnetic secondary phase $Zn_2Mo_3O_8$ is observed in the final product. By adding MoO_3, which has a considerably lower melting temperature (795 °C) compared to MoO_2 (1100 °C), the formation of the secondary phase was suppressed at smaller w values. The minimization of the secondary phase was found to be a key in controlling the Li and Zn concentration of the primary phase.

Except for ZnO and Li_2MoO_4 which were dried at 160 °C before using, all the starting chemicals were used as received. The mixture of the chemicals was grinded, pelletized, and put into an Al_2O_3 crucible which was then evacuated and sealed in a quartz tube. For most of the solid-state-reactions the heat-treatment sequence (see Fig.2.1) was started with a 100 °C/h ramp to 600 °C, and then keeping the temperature for 24 h, before ramping up with 10 °C/h to the final temperature of 1050 °C. After keeping the final temperature for 12 h, the reaction vessel was quenched into water. The final temperature of 1000 °C instead of 1050 °C was used for two samples: *procedure A* with

$w = 0$ and *procedure Ref.* A regrinding and second reaction sequence were done only for *procedure Ref*, otherwise only one reaction sequence was performed. As the final step, the reacted powder would be grinded until it would be fine enough to pass through a 50 micron mesh and then washed with 3M HCl and rinsed with pure water several times to remove unreacted ingredients. The purpose for using the 50 micron mesh is solely to make a more homogeneous distribution of grain sizes of the sample for x-ray scattering. Almost all *procedure A* has a small and *procedure B* a large amount of secondary phase which was identified as non-magnetic $Zn_2Mo_3O_8$. As a reference for the non-magnetic secondary phase, a polycrystalline sample of $Zn_2Mo_3O_8$ compound was also separately synthesized as previously reported in Ref. [25].

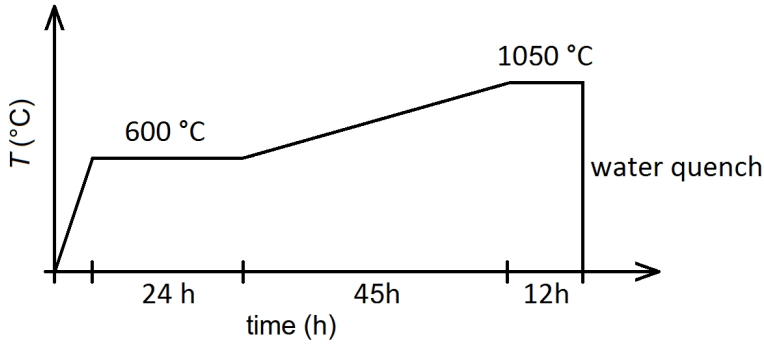

Figure 2.1: Heat treatment sequence for the solid-state-reaction of LZMO.

After the HCl wash, the polycrystalline product including the primary phase and the secondary non-magnetic phase was obtained. Chemical formula for the two phases as well as their phase fraction were defined as:

$$z(\mathrm{Li}_{1+x}\mathrm{Zn}_{2-y}\mathrm{Mo}_3\mathrm{O}_8) + (1-z)(\mathrm{Zn}_2\mathrm{Mo}_3\mathrm{O}_8), \tag{2.4}$$

where x are y are doping parameters for Li and Zn, respectively, and z and $(1-z)$ are the primary phase and secondary phase fractions, respectively. In the Sect. 2.2 we shall describe how we experimentally estimate these parameters using the combined analysis of three methods: neutron powder diffraction, x-ray powder diffraction, and elemental analysis techniques. From the primary phase Li and Zn concentrations we can estimate the number of unpaired $S = 1/2$ fraction per Mo_3O_{13} clusters, *i.e.*, the fraction of magnetic $[Mo_3O_{13}]^{11+}$ $(S = 1/2)$ clusters as:

$$p = n(\mathrm{Li}) + 2n(\mathrm{Zn}) - 4, \tag{2.5}$$

where $n(\mathrm{Li})$ and $n(\mathrm{Zn})$ are the composition parameters for Li and Zn, respectively, and are $n(\mathrm{Li}) = 1 + x$ and $n(\mathrm{Zn}) = 2 - y$. Hence, we have:

$$p = 1 + x - 2y. \tag{2.6}$$

2.1.1 ^{7}Li enriched polycrystalline $LiZn_2Mo_3O_8$ synthesis

For the LZMO samples used in the inelastic neutron scattering experiment, two additional steps in the preparetion were introduced. First one is to replace the natural Li by the isotope enriched ^{7}Li to reduce the neutron absorption cross section in the samples. Second one is to wash the samples with heavy water D_2O. This is to eliminate the remaining hydrogen in the sample, which would be the origin of tremendous background due to its large neutron incoherent scattering cross section. It should be noted here that for the ^{7}Li enriched LZMO powder samples, the *procedure A* with $w = -0.1$ was used and two reaction sequences were performed instead of one.

^{7}Li enriched lithium was received as 99% isotopic purity $^7Li_2CO_3$. Reacting it into the desired starting chemical $^7Li_2MoO_4$ was started by evaporating the lithium carbonate for 3 hours at 120 °C. After this it was weighted and grinded in a mortar together with isomolar amount of MoO_3 using small amount of ethanol to make the mixing easier. Then this mixture was pressed into a pellet and reacted in an unsealed alumina crucible with the following heat treatment sequence: first a ramp up to 400 °C in 5 hours followed by a second ramp up to 650 °C during 80 hours, and a last ramp down to room temperature in 2 hours. This resulted in a solid white product of $^7Li_2MoO_4$ and evaporated side-product CO_2.

After the ^{7}Li enriched LZMO had been reacted twice and HCl washed, the D_2O rinse followed. This was done inside a disposable glove-bag filled with the argon gas to minimize hydrogen contamination. After the rinse, the sample was left inside the bag for a few days to dry.

2.2 Crystal structure and elemental composition characterizations

For the characterization of the crystal structure and elemental composition of LZMO samples, we used three different techniques: neutron powder diffraction (NPD), x-ray powder diffraction (XRD) and inductively coupled plasma (ICP) atomic emission spectroscopy. All the techniques were used in complement with each other as we shall explain later. Some of the advantages of NPD over XRD are: easier observation of Bragg peaks at high-momentum transfers than x-rays because of the practically Q-independent form factor for atomic scattering, high sensitivity for the detection of lighter elements, such as Li, and capability of detecting magnetic moment through the magnetic scattering cross section originating from the dipolar interaction.

ICP atomic emission spectroscopy (Arcos EOP, Spectro) was used to determine the elemental ratios of Li, Zn, and Mo of the LZMO powder samples. The preparation for the measurement began with weighting 6 mg of powder sample into a sealed vapor pressure vessel with 6 ml 30% HNO_3 solution. After the sample had decomposed overnight under 160°C vapor pressure it was made into a 100 ml solution, which of 10 ml were consumed in the experiment that included three repeated measurements. Three standard solutions with Li, Zn, and Mo concentrations being (i) 0, 0, 0 ppm, (ii) 0.508, 10.04, and 20.06 ppm, and (iii) 1.016, 20.08, and 40.12 ppm, were measured together with 1.8% HNO_3 so that the experimental data were evaluated on a calibration curve using the variance-covariance matrix error analysis [34]. Assuming Mo to be stoichiometric, relative amounts of Li and Zn were obtained.

XRD was performed using the Cu K_α radiation (Ultima IV, Rigaku and RINT-V, Rigaku). The scattering angle range of $5 \leq 2\theta \leq 90°$ was scanned in steps of 0.02° at room temperature. The former diffractometer was used for the actual data acquisition in this work as it is equipped with a 1-dimensional detector enabling better statistics at less acquisition time compared to the latter diffractometer with a point detector which was only used for quick checks of the sample quality.

NPD was performed using the high resolution powder diffractometer ECHIDNA [35], installed at the OPAL research reactor, Australian Nuclear Science and Technology Organisation. Figure 2.2 shows the layout of the diffractometer. The angular range of $6.5 \leq 2\theta \leq 164°$ was scanned in steps of 0.05° at room temperature. Neutrons with the wavelength of $\lambda = 2.4395(5)$ Å were selected by the Ge monochromator using the 331 reflections.

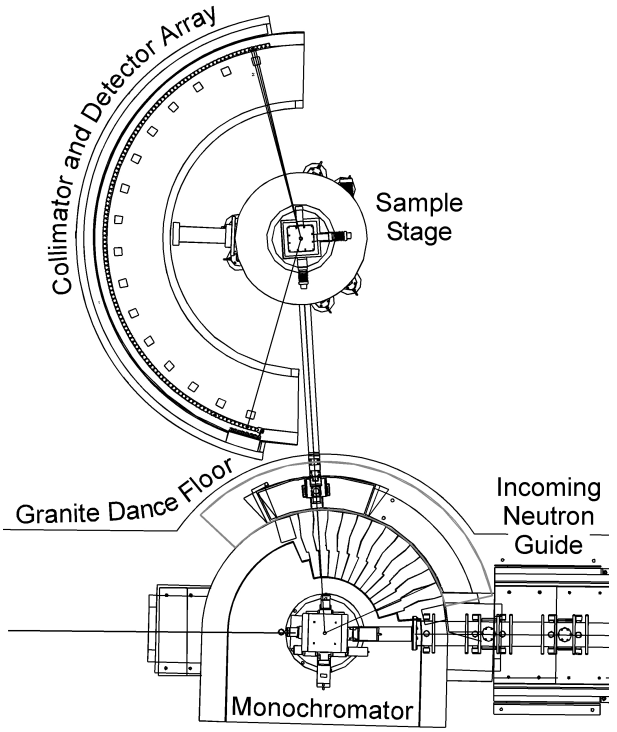

Figure 2.2: Layout of the high resolution neutron powder diffractometer ECHIDNA. The incident neutron wavelength is chosen from the incoming white neutron beam by the monochromator crystal. The scattered neutrons are collimated for improved resolution before detected by an array of 128 position sensitive ^{3}He detector tubes. Reprinted with permission from Ref. [35].

.

Utilizing the difference in the scattering lengths for the neutrons and x-rays, we performed combined XRD + NPD Rietveld analysis using the Fullprof software [36] to obtain the Li and Zn compositions in the primary phase, as well as to determine the fraction of the secondary phase. The details of the Rietveld refinement will be described further in the experimental result chapter. In the Rietveld analysis, first, linear restrains were put on the total Li and Zn composition in the primary phase. After the initial refinement cycle was finished, a script was run to calculate the total Li and Zn compositions in both the primary and secondary phases. Then, by comparing the resulting total Li and Zn compositions to those obtained in ICP, we adjusted the linear restrains on the first phase accordingly. By running the refinement and the script in iteration until convergence, the ICP results were effectively used to constrain the total Li and Zn compositions. Initial refinement parameters were taken from [29] and [37] for the primary and secondary phase, respectively.

2.3 Magnetization, specific heat, and electron spin resonance measurements

2.3.1 Magnetization measurement

Magnetic property measurement systems (MPMS) are high precision magnetometers based on a superconducting quantum interference device (SQUID) [38]. The magnetometer (MPMS-XL, Quantum Design) shown in Fig. 2.3 was used to measure the magnetic susceptibility in the range of $2 < T < 300\,\mathrm{K}$ under 1 T magnetic field. We decompose the observed magnetization as $M_{\mathrm{obs}} = B(\chi_{\mathrm{cell}} + m_{\mathrm{tot}}[z\chi_{1\mathrm{st}}/\mathcal{M}_{1\mathrm{st}} + (1-z)\chi_{2\mathrm{nd}}/\mathcal{M}_{2\mathrm{nd}}]/SF)$, where B, χ_{cell}, m_{tot}, $\chi_{1\mathrm{st}}$, $\chi_{2\mathrm{nd}}$, $\mathcal{M}_{1st}$, $\mathcal{M}_{2nd}$, and SF are the magnetic field, magnetic susceptibility of the sample cell, total mass of the sample, magnetic susceptibilities of the primary and secondary phases, molar masses of the primary and secondary phases, and sample shape factor [39], respectively. After obtaining $\chi_{1\mathrm{st}}$ from the observed M_{obs}, we estimate the intrinsic magnetic susceptibility of the primary phase as $\chi = \chi_{1\mathrm{st}} - \chi_0$, where $\chi_0 = -3.68(1) \times 10^{-5}$ emu is the diamagnetic contribution which we approximate to be the same as for the non-magnetic secondary phase $Zn_2Mo_3O_8$ ($\chi_0 \sim \chi_{2\mathrm{nd}}$).

Figure 2.3: Magnetic property measurement system MPMS-XL.

The MPMS-XL magnetometer was also used to measure isothermal field dependent magnetization up to $H = 5\,\mathrm{T}$.

2.3.2 High field magnetization and electron spin resonance measurements

The 15T-CSM cryogenic free superconducting magnet at the Institute for Materials Research (IMR), Tohoku University was used together with a helium cryostat to measure the high-field magnetization. Two different samples were used in this study prepared using slightly different solid-state-reaction recipes. The first sample was made with the natural Lithium, whereas the second sample with enriched Lithum-7 as an ingredient. The diamagnetic background of the empty Teflon sample cell is subtracted from the data. It was estimated to be $\chi_{0\text{cell}} = -1.236\times10^{-7}$ emu Oe^{-1} by measuring the sample cell using MPMS at $T = 300\,\text{K}$ under $5\,\text{T}$ magnetic field. Using $28\,\text{T}$ pulse field magnet (IMR), electron paramagnetic resonance and high-field magnetization were measured for the Li-natural sample.

The 20T-CSM cryogenic free superconducting magnet at IMR was used together with a helium cryostat to measure field dependent magnetization at different temperatures in the range of $50 < T < 210\,\text{K}$. The background signal was estimated by measuring the empty sample cell at $T = 153(5)\,\text{K}$, and assuming it is temperature independent, it was subtracted from all the data. The data were normalized to the low-field results obtained by MPMS (IMRAM) up to 5 T. Using the transmission setup, the electron spin resonance was also measured using 20T-CSM.

2.3.3 Specific heat measurement

The physical property measurement system (PPMS) at the Institute for Solid State Physics, University of Tokyo was used to measure the specific heat. The sample for the specific heat measurement was prepared by pressing the powder into thin flakes to maximize the heat conduction from the sample to the cell, as well as to minimize the internal heat gradient inside the sample. The powder sample *procedure A* with $w = -0.1$ which is most closest to the stoichiometry was selected for the experiment.

2.4 Inelastic neutron scattering measurement

2.4.1 Neutron scattering experiment at the High Resolution Chopper spectrometer

Neutron inelastic scattering was performed to study the spin excitations in the polycrystalline improved stoichiometry LZMO using the High Resolution Chopper spectrometer (HRC) at the Material and Life Science Experimental Facility (MLF), J-PARC [40, 41]. The schematic drawing of the HRC spectrometer is shown in Fig. 2.4. The unique feature of this spectrometer is the small-angle detector bank covering the scattering angle range $0.6 < 2\theta < 3\,^{\circ}$. With the capability for choosing the high-incident energy and also high relative energy resolution $\mathrm{d}E/E_{\mathrm{i}}$, this spectrometer enables us to reach very small Q region ($Q < 1\text{Å}^{-1}$) with sufficiently high energy transfer. The energy-momentum-transfer coverage of the representative two cases was calculated, and shown in Fig. 2.5, together with the calculation for the condition used in the previous report [27]. It is clear that the HRC spectrometer provides a much wider accessible range in energy and momentum-transfer space with incident neutron energies $E_{\mathrm{i}} = 300\,\mathrm{meV}$ and $500\,\mathrm{meV}$. It may be noted that the magnetic form factor decays quite rapidly as Q becomes larger for the Mo_3O_{13} clusters in the LZMO; the red gradient in Fig. 2.5 represents the magnetic form factor estimated in Ref. [27]. It can be clearly seen that the low-Q capability of the HRC spectrometer is the key to observe the postulated magnetic excitation which may appear around $\hbar\omega \sim 37\,\mathrm{meV}$ in LZMO.

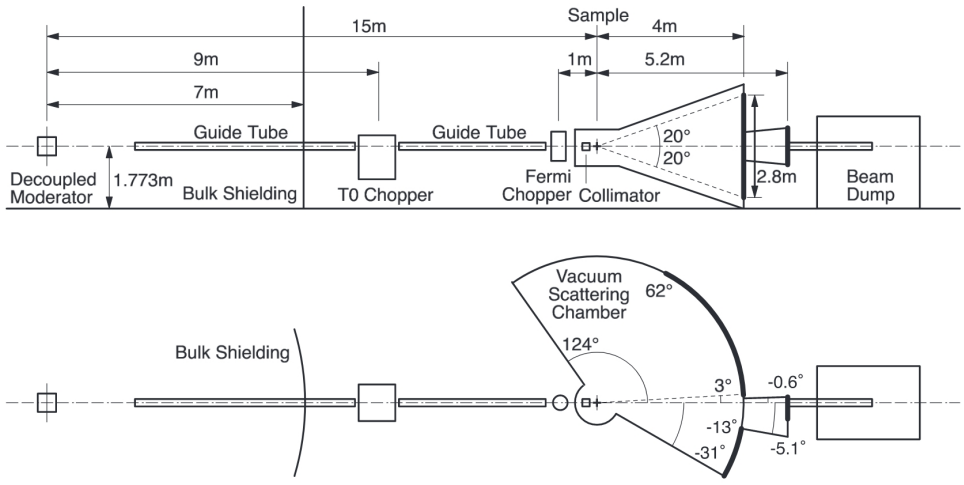

Figure 2.4: The schematic drawing of HRC. Thick lines indicate detector arrays of ^{3}He position sensitive detectors. Reprinted with permission from Ref. [42]. ©2019 The Physical Society of Japan

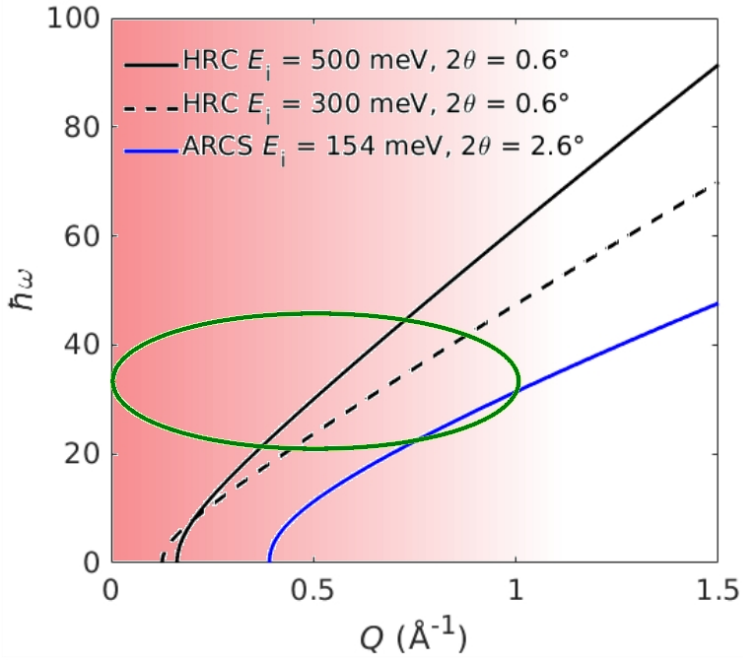

Figure 2.5: Calculated accessible momentum (Q) and energy-transfer ($\hbar\omega$) space for the High Resolution Chopper speactrometer. Calculations were done for the two incident energies E_i = 500 meV and 300 meV , shown by the black solid and dashed lines, respectively. Calculation for the ARCS spectrometer with E_i = 154 meV, which is the condition used in the previous work [27], are also shown by the as blue solid lines. The red gradient represents the magnetic form factor for Mo_3O_{13} clusters calculated in Ref. [27]. The green ellipse marks our initial guess for the postulated magnetic excitation.

43 g of powder ^{7}Li enriched LZMO was prepared in the method that produced the composition most closest to the stoichiometry. The powder was pressed into a 34 mm diameter and 12 mm thick pellet by a custom made pelletizer. The pellet was mounted on a flat neutron Brillouin scattering sample can (See Fig. 2.6). Some exploratory runs were performed using the high incident energy E_i = 500 meV. The main part of the experiments was done using the moderate E_i = 311 meV, with tighter incident collimation of 0.3° divergence. With this incident neutron energy, we performed the two runs; the base-temperature (5 K) run for 46 hours, and the room-temperature (295 K) run for 47 hours. The raw data were processed and analyzed using the HANA software provided on-site.

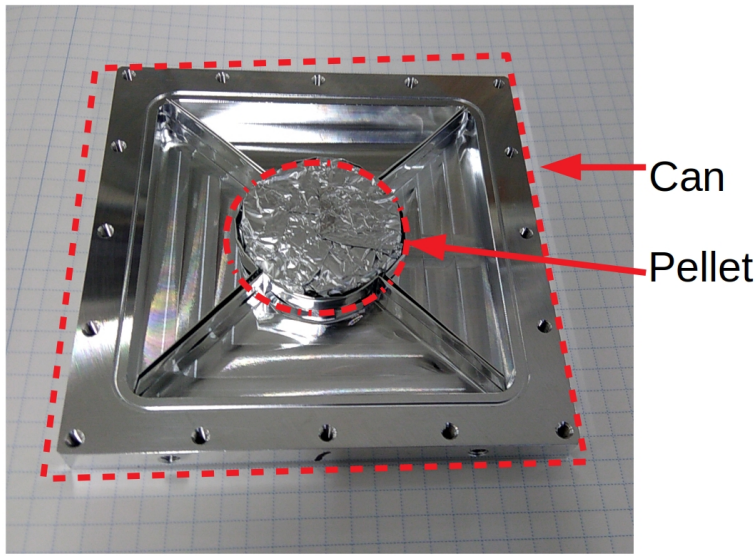

Figure 2.6: Neutron Brillouin flat sample cell used at for the HRC experiment. The sample is a pressed pellet wrapped in aluminum foil and fixed by aluminum plates to the center of the can.

2.4.2 Neutron scattering experiments at the Polarized Triple-Axis Spectrometer and the Hybrid Spectrometer

Polarized Triple-Axis Spectrometer (PTAX) at the High Flux Isotope reactor (HFIR) and Hybrid Spectrometer (HYSPEC) [43] at the Spallation Neutron Source (SNS) both at Oak Ridge National Laboratory (ORNL) were also used to measure the spin excitations in LZMO. The LZMO sample measured both at PTAX and HYSPEC were the same ^{7}Li enriched with the *procedure A* with $w = -0.1$. This sample preparation method produced the best Li and Zn composition with acceptable amount ($\sim$10%) of the secondary non-magnetic $Zn_2Mo_3O_8$. The powder was pressed into pellets and assembled into 4 cm long rods by wrapping them into aluminum foil. One 5 mm diameter rod weighting 5 g and three 8 mm diameter rods weighting 8 g were made and assembled together using aluminum foil and wire as shown in Fig. 2.7. The sample setting shown was used in the HYSPEC experiment and this allowed the switching between the thinner 5 mm diameter and thicker cluster of three 8 mm rods by moving the sample cell vertically. Also, the wall thickness of the soda-can is only 0.33 mm to reduce the background. For the PTAX experiment, the soda-can sample cell was replaced by conventional aluminum sample can and the neutron beam center was fixed to the thicker three rod cluster.

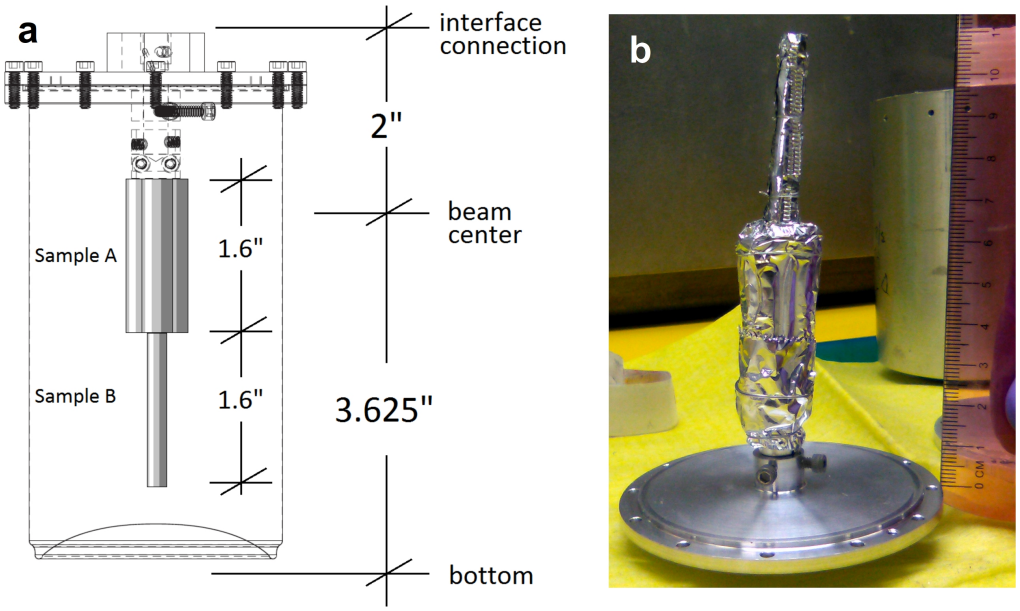

Figure 2.7: (a) Schematic drawing of the ^{7}Li enriched LZMO powder sample in the soda-can type sample cell used in the HYSPEC experiment. Sample A is a cluster of three 4 cm long 8 mm diameter rods each weighting 8 g. Samble B is a single 4 cm long 5 mm diameter rod weighting 3 g. The sample cell can be adjusted vertically by changing the beam center position from Sample A to Sample B. The dimensions are shown in inches. (b) Photograph of the sample being up-side down and connected to the soda-can sample cell lid.

For the PTAX experiment, the collimations of 48'-40'-60'-240' were used for most of the scans, whereas some exploratory scans were done with 48'-80'-60'-240' to increase the flux. The incident and outgoing beam slits were 1 1/2" x 45 mm and 19 mm x 2 1/4", respectively for most of the scans. The spectrometer was operated in the triple-axis mode, where the final energy was fixed to $E_f = 30.5$ meV or 41 meV. When the elastic signal was measured, the lower final energy $E_f = 13.7$ meV was used to obtain much better energy resolution. The polarization analysis mode was used, where the monochromator and analyzer utilize the Heusler 111 reflections. Spin flippers were inserted before and after the sample to control the spin polarization direction of neutrons, and a Helmholtz coil was placed around the sample so that the neutron polarization at the sample position can be set either parallel or vertical to the scattering-vector direction. This setup enables us to perform the full one-dimensional xyz polarization analysis. For the PTAX experiment, the sample, which was set in the standard aluminum can as described above, was set in the closed-cycle ^{4}He refrigerator with the base temperature $T = 4.5$ K. This sample environment in the polarized neutron setting is seen in Fig. 2.8.

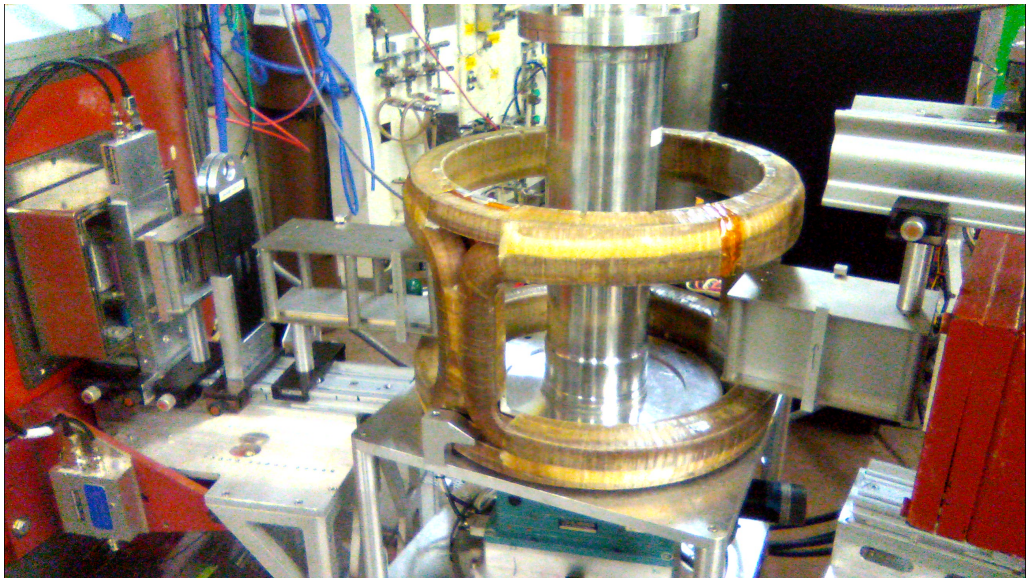

Figure 2.8: Neutron guides and the Helmholz coil around the sample environment CCR-P cryostat in the Polarized Triple-Axis Spectrometer (PTAX).

For the HYSPEC experiment, the two incident energies of $E_\mathrm{i} = 60$, and 9 meV were selected using the combination of the PG monochromator and the Fermi chopper. For this spectrometer, the energy resolution is primarily given by the selected incident energy and chopper frequency; in this experiment we use $f_\mathrm{chopper} = 180$, and 240 Hz, which results in the energy resolution at the elastic position as $\mathrm{d}E = 6$ meV ($E_\mathrm{i} = 60$ meV) and $\mathrm{d}E = 0.3$ meV ($E_\mathrm{i} = 9$ meV). The experiment was performed with the unpolarized mode. The sample, loaded in the soda-can-type sample can as described above, was set in the Orange cryostat with the base temperature being 1.7 K.

In the HYSPEC experiment, as noted above we used two incident energies, $E_\mathrm{i} = 60$, and 9 meV. For the high-incident energy experiment, aiming at reaching the lowest Q attainable with this spectrometer, we used thinner sample (sample B) to reduce the angle ambiguity originating from the sample size. This way, one can measure lower-Q range closer to the direct beam position. For the lower-energy scans, since the incident flux is quite limited, we use the larger volume sample (sample A). The obtained raw data were reduced to the spe files on-site using the Mantid software suites [44].

3 Experimental Results

In this chapter, we will describe experimental results and related analyses. This chapter is divided into three parts. The first part describes the study of improving sample preparation, which enables us the hole doping study of LZMO in a wider hole concentration range than the earlier work. The second part reports the results of magnetic measurements on the the series of $Li_{1+x}Zn_{2-y}Mo_3O_8$ samples obtained using the improved sample preparation technique. The final part contains the results of the neutron scattering study using the $Li_{1+x}Zn_{2-y}Mo_3O_8$ sample that has the closest composition to the ideal $LiZn_2Mo_3O_8$.

3.1 Chemical composition control of $Li_{1+x}Zn_{2-y}Mo_3O_8$

Chemical compositions of all the obtained powder samples were checked by the ICP atomic emission spectroscopy. Elemental compositions for Li and Zn obtained in the present ICP analysis are summarized in Table. 3.1. It may be repeated here that the sample prepared in the present study is a mixture of the major amount of the primary $Li_{1+x}Zn_{2-y}Mo_3O_8$ phase and minor amount of the secondary $Zn_2Mo_3O_8$ phase. Hence, the elemental compositions obtained in the ICP analysis are the phase-ratio-weighted average of the primary and secondary phase compositions, *i.e.* $z(1+x)$ and $(2-zy)$ for Li and Zn, respectively (see Eq. 2.4 in Sect. 2.1.1). To visualize the nominal-composition-parameter (w) dependence, the elemental compositions are plotted as a function of w in Fig. 3.5 (see Eq. 2.1 in Sect. 2.1.1 for the definition of w). Both the Li and Zn compositions show linear w dependence of opposite sign. Shown by the red and blue solid lines are the ratios of Zn and Li elements in the starting materials (see Eq. 2.1 for the composition of the starting materials). The Li composition in the final product is almost the same as that of the starting material (solid line), while there is a large decrease in the Zn composition from the starting material to the final product, as unreacted ZnO has been removed by the HCl wash. As a result, Zn does not surpass the stoichiometric value (dash-dotted

line) while Li does so. It may be noted that the Zn composition starts to decrease when Li surpasses the stoichiometric line. This suggests that excess Li may replace the Zn atoms at the Li/Zn mixed sites.

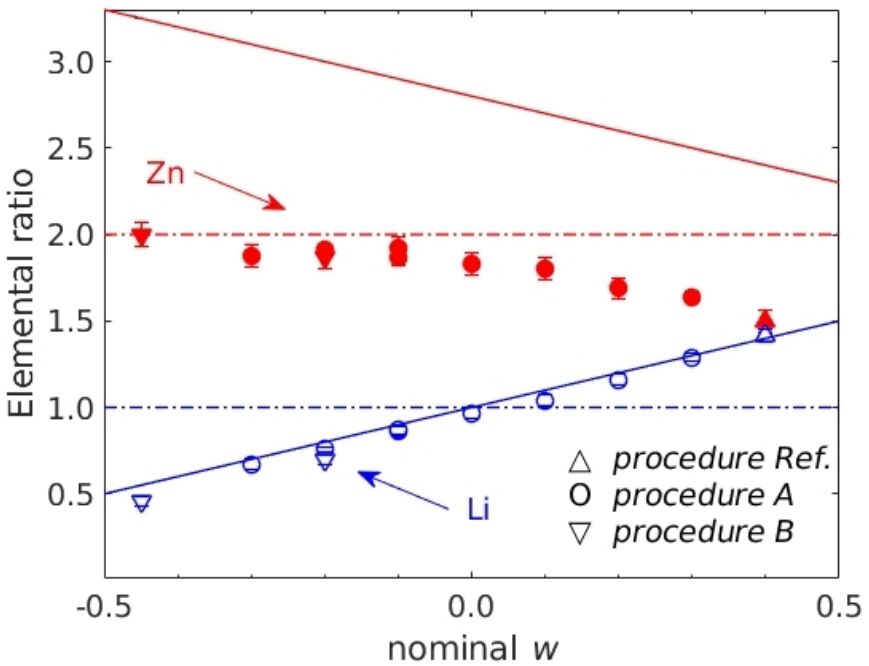

Figure 3.1: Nominal starting composition w dependence of the elemental ratio of Li (Blue open markers) and Zn (red filled markers) obtained from ICP data in relation to postulated stoichiometric Mo concentration. Dash-dotted lines and solid lines are the stoichiometric ratio and nominal starting ratio, respectively. Up-pointing triangle, circle, and down-pointing triangle markers are associated with the *procedure Ref*, *procedure A*, and *procedure B* samples, respectively.

Table 3.1: Crystallographic data of $Li_{1+x}Zn_{2-y}Mo_3O_8$ at 300 K from the combined NPD + XRD Rietveld refinement with the ICP data being used as constrains when determing x and y. Z is 6 and space group is $R\bar{3}m$ (No. 166). Unpaired spin 1/2 concentration per Mo_3O_{13} cluster is given as $p = 1 + x - 2y$. a, c and V are the lattice constants along the a- and c-axes, and the unit cell volume, respectively. B_{Mo}, B_O, and $B_{Li/Zn}$ are the isotropic atomic displacement parameters for the atoms specified by the subscripts. Variables is the number of free parameters used for the Rietveld refinement in its final iteration. NPDs and XRDs are the number of Bragg-reflections in the x-ray and neutron diffraction data that were included in the Rietveld refinement. The agreement between observed and calculated peaks is quantified by the parameter R_p, R_{wp}, R_{exp}, and χ^2, which are the profile factor, weighted profile factor, expected weighted profile factor, and Chi-squared, respectively.

procedure	*Ref*	*A*	*A*	*A*	*A*	*A*
w	0.4	0.3	0.2	0.1	0	−0.1
x	0.42(4)	0.29(2)	0.16(4)	0.04(4)	0.02(4)	−0.09(3)
y	0.50(7)	0.36(4)	0.31(7)	0.20(7)	0.17(7)	0.14(5)
z	1	1	1.000(11)	0.998(11)	0.953(11)	0.949(10)
p	0.42(13)	0.57(7)	0.54(14)	0.64(14)	0.67(15)	0.63(11)
a (Å)	5.7843(3)	5.7911(3)	5.7935(3)	5.7968(3)	5.7968(3)	5.8016(3)
c (Å)	31.053(2)	31.082(2)	31.081(2)	31.089(2)	31.082(2)	31.093(2)
V (Å^3)	899.78(9)	902.72(9)	903.48(9)	904.72(9)	904.52(9)	906.33(9)
B_{Mo} (Å^2)	0.42(3)	0.51(3)	0.80(3)	0.67(3)	0.53(3)	0.68(3)
B_O (Å^2)	0.48(4)	0.45(4)	0.57(4)	0.58(4)	0.49(4)	0.60(4)
$B_{Li/Zn}$ (Å^2)	0.59(7)	0.57(6)	0.56(6)	0.60(5)	0.54(6)	0.57(6)
Variables	27	27	30	30	40	40
NPDs	88	88	134	134	134	134
XRDs	257	250	387	386	389	389
R_p (%)	5.89	5.51	5.4	5.41	5.39	5.24
R_{wp} (%)	7.76	7.09	7.17	7.02	7.02	6.81
R_{exp} (%)	3.39	4.02	3.9	4.01	3.9	3.24
χ^2	5.34	3.17	3.37	3.1	3.31	4.59

procedure	*A*	*A*	*A*	*B*	*B*
w	−0.1	−0.2	−0.3	−0.2	−0.45
x	−0.05(4)	−0.16(2)	−0.19(4)	0.03(5)	0.14(6)
y	0.08(8)	0.10(4)	0.14(8)	0.19(10)	0.00(13)
z	0.916(9)	0.899(9)	0.836(10)	0.676(8)	0.528(7)
p	0.78(15)	0.64(7)	0.52(16)	0.65(20)	0.86(26)
a (Å)	5.8016(3)	5.8053(3)	5.8056(3)	5.7968(3)	5.8052(3)
c (Å)	31.094(2)	31.101(2)	31.104(2)	31.091(2)	31.097(2)
V (Å^3)	906.36(9)	907.72(9)	907.91(9)	904.76(9)	907.58(9)
B_{Mo} (Å^2)	0.48(3)	0.58(3)	0.63(3)	0.54(3)	0.57(4)
B_O (Å^2)	0.45(3)	0.61(4)	0.52(4)	0.48(5)	0.57(5)
$B_{Li/Zn}$ (Å^2)	0.46(5)	0.58(5)	0.56(6)	0.47(6)	0.54(7)
Variables	40	40	40	43	43
NPDs	134	134	134	134	134
XRDs	388	389	389	389	391
R_p (%)	4.96	5.22	5.74	4.62	4.52
R_{wp} (%)	6.43	6.68	7.34	6.05	6.05
R_{exp} (%)	3.69	3.82	4.05	3.86	3.73
χ^2	3.05	3.1	3.32	2.52	2.65

Next, to determine the phase fraction of the primary $Li_{1+x}Zn_{2-y}Mo_3O_8$ and secondary $Zn_2Mo_3O_8$ phases, as well as to determine the site occupancies in the primary phase, we have performed the XRD and NPD experiments. Representative XRD and NPD patterns for the sample with $w = -0.1$ prepared using the *procedure A* are given in Fig. 3.2. The XRD and NPD patterns are then simultaneously analyzed using the Rietveld technique. The result of the simultaneous Rietveld fitting is also shown in Fig. 3.2. The XRD and NPD patterns and Rietveld fits for all LZMO samples are shown in Appendix A. Both the

XRD and NPD patterns are satisfactorily reproduced by the Rietveld fitting, confirming the validity of the obtained crystallographic parameters. Fractional coordinates and occupancy parameters for the representative datasets are summarized in Table. 3.2. From these crystallographic parameters, we obtain the composition parameters of the Li and Zn in the primary phase as $x = -0.05(4)$, $y = 0.08(8)$, and the phase fraction of the primary phase as $z = 0.916(9)$ for the $w = -0.1$ powder sample. Applying the same analysis, we obtain the chemical composition parameters for all the other powder samples prepared from different initial composition with different procedures. The resulting chemical compositions, together with main crystallographic parameters, are also shown in Table 3.1. In the table, the experimental uncertainty given in the parentheses for x and y are derived from the ICP results, whereas those for the other parameters are from the Rietveld refinement. The R-factors and χ^2 are reasonably small for all the refinements, indicating that the chemical compositions are accurately obtained in the present analysis.

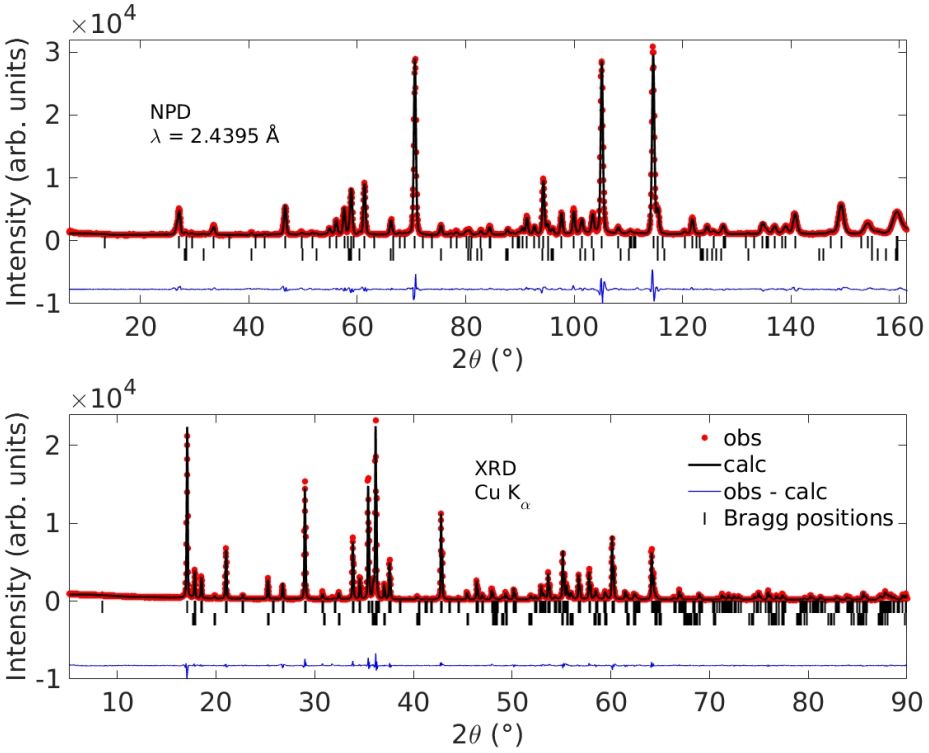

Figure 3.2: Combined Rietveld analysis on $Li_{1+x}Zn_{2-y}Mo_3O_8$, $w = -0.1$ from high resolution powder diffraction at 300 K on ECHIDNA and x-ray diffraction patterns. The bottom blue lines give the difference between the observed (red dots) and calculated (black line) intensities. Bragg positions are shown as vertical bars in the upper and lower row for the primary and secondary phase, respectively.

Table 3.2: Fractional coordinates and site occupancies for $Li_{1+x}Zn_{2-y}Mo_3O_8$, $w = -0.1$, $x = -0.05(4)$, $y = 0.08(8)$, $z = 0.916(9)$. Isotropic atomic displacement parameters are $B_{Mo} = 0.48(3)$, $B_O = 0.45(3)$, and $B_{Li/Zn} = 0.46(5)$ Å^2.

Atom, i	Site	a_i/a	b_i/b	c_i/c	occupancy
Mo1	18h	0.18493(8)	0.81507(8)	0.08372(5)	1
O1	18h	0.8451(3)	0.1549(3)	0.04788(12)	1
O2	18h	0.4924(3)	0.5076(3)	0.12458(12)	1
O3	6c	0	0	0.11841(18)	1
O4	6c	0	0	0.37140(18)	1
Zn1	6c	1/3	2/3	−0.64229(9)	0.933(4)
Li1	6c	1/3	2/3	−0.64229(9)	−0.00(3)
Zn2	6c	0	0	0.18144(10)	0.759(4)
Li2	6c	0	0	0.18144(10)	0.25(3)
Zn3	3a	0	0	0	0.323(6)
Li3	3a	0	0	0	0.48(4)
Zn4	6c	0	0	0.5051(15)	0.063(3)
Li4	6c	0	0	0.5051(15)	0.48(2)
Li5	6c	2/3	1/3	0.08392	−0.003(16)

Before going into details of the achieved composition range, as well as corresponding spin concentration range, let us analyze the nominal-composition-parameter w dependence of the crystallographic parameters, such as lattice constants and occupations. In Fig. 3.3, the lattice constants a and c are plotted against $x + y$, which is the sum of the positive deviation of Li and negative deviation of Zn from the stoichiometry. The plot shows decreasing behavior of a and c on $x + y$. This suggests that the replacement of Zn with Li results in decrease of the lattice constants obeying the Vegard's law. Knowing that both the lattice constants dominantly depend on the total deviation $x + y$, we fit $(x + y)$-dependence of a and c using a linear function. The fitting results are also shown in Fig. 3.3. The lattice constants a and c are found to be linearly approximated to the following functions: $a = -0.020(2)(x + y) + a_0$ and $c = -0.039(6)(x + y) + c_0$, with the estimated lattice constants for the stoichiometric compound $a_0 = 5.8027(6)$ Å and $c_0 = 31.097(3)$ Å.

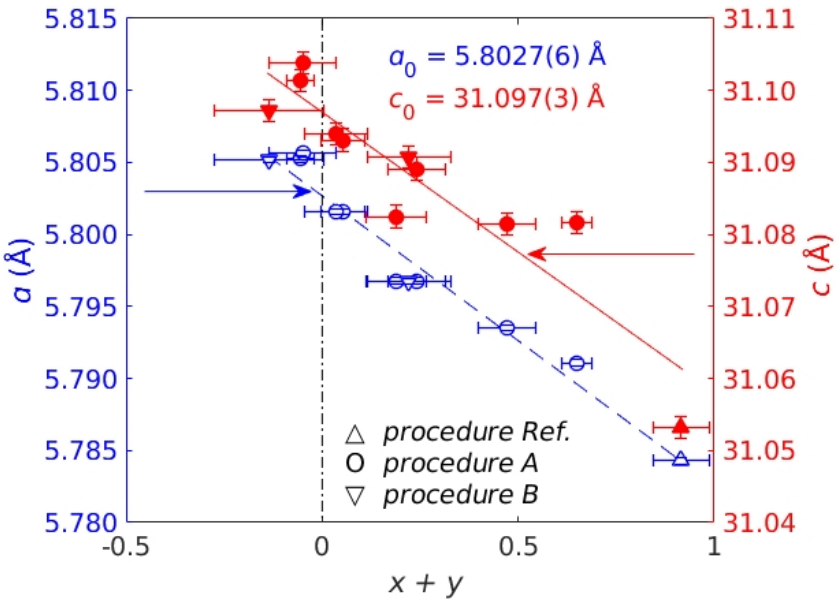

Figure 3.3: Dependence of lattice constants a and c on $x+y$ in open blue markers (left axis) and filled red markers (right axis), respectively. The black dash-dotted line shows the stoichiometric value of $x + y = 0$. Up-pointed triangle, circle and down-pointed triangle markers are associated with the *procedure Ref*, *procedure A*, and *procedure B* samples, respectively.

To investigate the site dependence of the Li and Zn composition variation, the w dependent occupancy of the four Li/Zn sites and fifth Li site is presented in Fig. 3.4. This data can also be found in the tabulated form in Appendix A. Among the Zn rich tetrahedral sites, *site 1* is almost only occupied by Zn, whereas *site 2* have large fluctuation in Li occupation ranging as 0.12 – 0.41. Similarly for the Li rich octahedral sites, there is only a small Zn occupation 0.012 – 0.094 in *site 4* compared to the largely varying Zn occupation 0.087 – 0.367 in *site 3*. *Site 5* has zero occupancy of Li except for the $w = 0.1$, 0.2, and 0.4 samples where tiny inclusion of Li improved the refinement slightly. The site preferences of Li and Zn atoms are consistent with those of previous samples [25, 29].

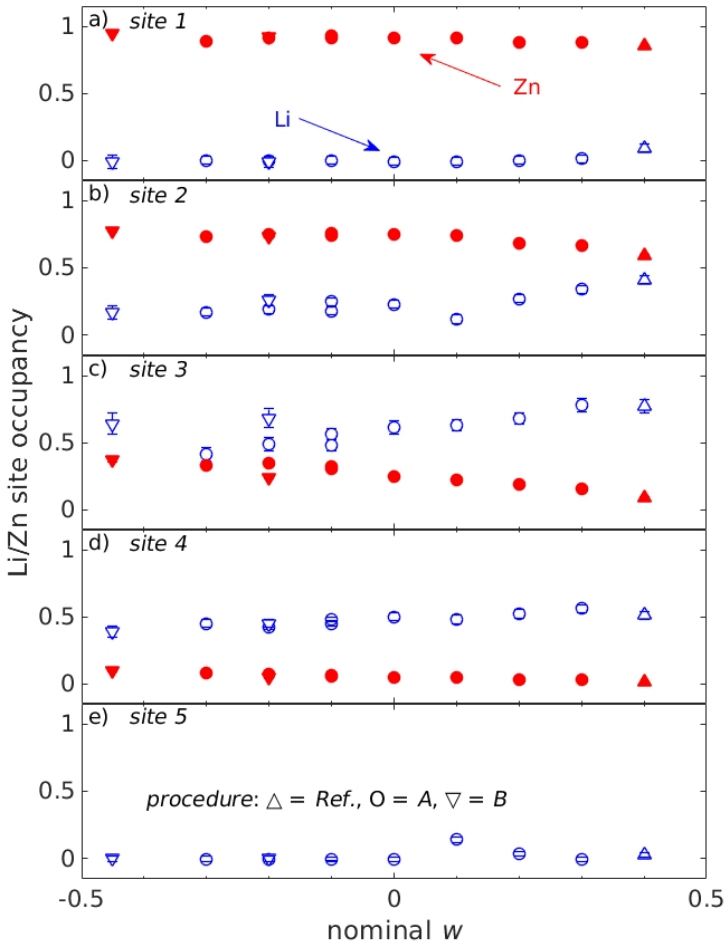

Figure 3.4: w dependence of the occupation of Li/Zn sites. Panels (a) – (e) represent *Sites 1 – 5*, respectively. Up-pointed triangle, circle, and down-pointed triangle markers are associated with the *procedure Ref*, *procedure A*, and *procedure B* samples, respectively.

Here, let us analyze the relation between the nominal composition and the composition of the primary phase obtained in the present improved solid-state-reaction technique. First, to visualize the w-dependence, the parameters x, y, and z are plotted as a function of w in Fig. 3.5. The primary-phase fraction z becomes almost unity for $w > 0$, whereas the fraction of the secondary phase significantly increases as w becomes smaller than 0. The Li concentration parameter x almost monotonically increases as a function of w, with the stoichiometry concentration realized at $w \sim 0$. On the other hand, the Zn concentration parameter y is mostly w-independent for $w < 0$, whereas it shows significant increase as w becomes larger than 0. From those w-dependencies, we conclude that the best sample closest to the stoichiometry is obtained for the starting nominal composition parameter

$w = -0.1$ with the preparation *procedure A*, which was indeed chosen as "representative" in the earlier paragraph. As noted before, the composition and phase-fraction parameters are $x = -0.05(4)$, $y = 0.08(8)$, and $z = 0.916(9)$ for the $w = -0.1$. It may be noteworthy that they correspond to the unpaired spin 1/2 concentration per Mo_3O_{13} cluster as $p = 1 + x - 2y = 0.78(15)$, which is greatly improved from 0.42(13) of the *procedure Ref* sample obtained using almost the same manner as the earlier report [25].

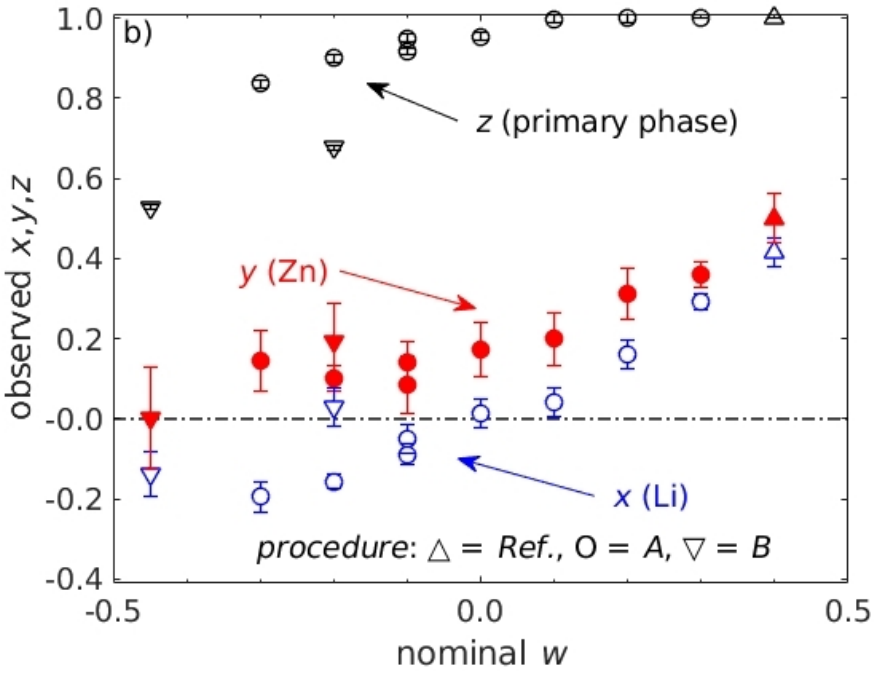

Figure 3.5: Nominal w dependence of observed parameters x (Li) (Blue open markers), y (Zn) (red filled markers), and z (primary phase) (black open markers) obtained by combined XRD + NPD Rietveld analysis. Black dash-dotted line shows the stoichiometric value for x and y.

In Fig. 3.6(top), we plot the total n(Li) + n(Zn) composition as a function of the nominal composition parameter w. It can be clearly seen that for the wide range of $w \geq -0.1$, the total n(Li) + n(Zn) composition is close to 3. This indicates that in our sample the site deficiency is minimized there. The significant deficiency can be seen for the samples with nominal w parameter less than $w \leq -0.1$, where secondary phase fraction becomes much larger.

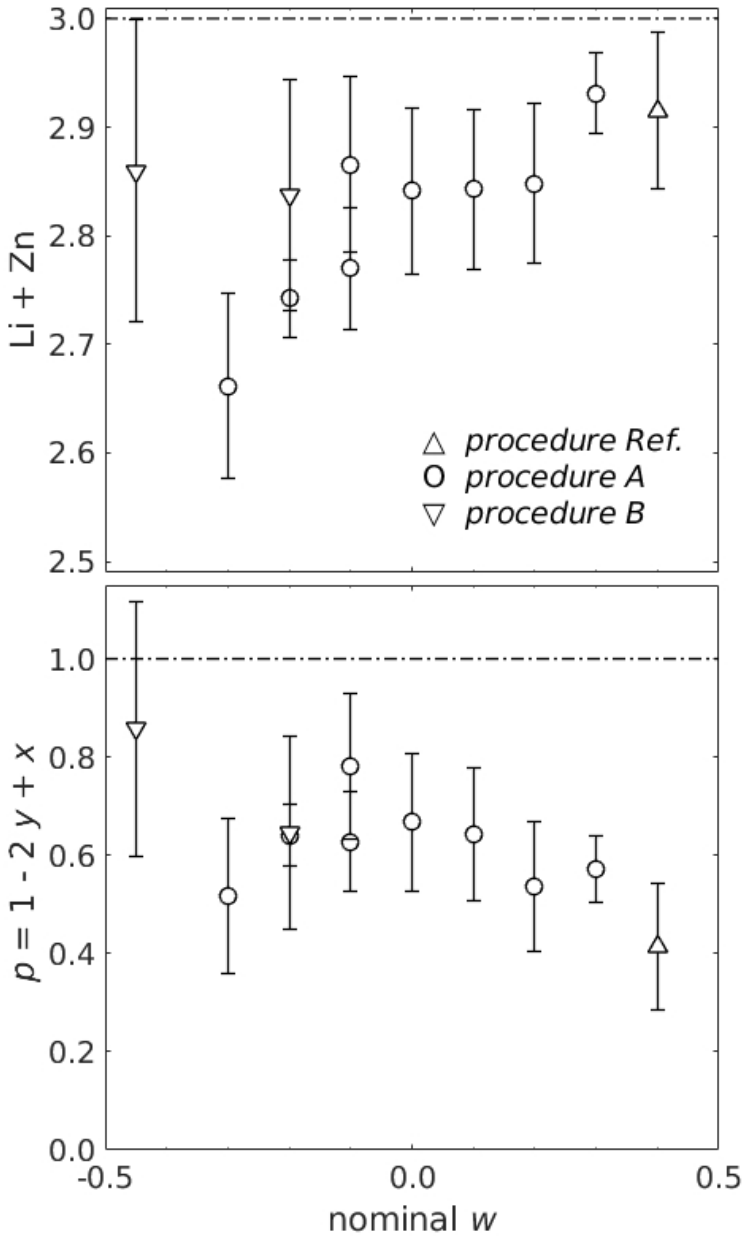

Figure 3.6: Upper panel) w dependence of Li + Zn. Lower panel) w dependence of number of magnetic $[Mo_3O_{13}]^{11+}$ ($S = 1/2$) clusters p. The ideal value is shown as the black dash-dotted lines in both panels.

Also shown in Fig. 3.6(bottom) is the concentration parameter for the $S = 1/2$ spins on Mo_3O_{13} cluster. It can be suggested that p has a linear w dependence for $w \geq -0.1$, where the Li/Zn deficiency is minimized. Therefore, using the samples in this region, we can now perform spin concentration dependence study with minimizing structural

deficiency effect.

After knowing the above results, we may point out two issues in the earlier work. One is the true composition of the $LiZn_2Mo_3O_8$ sample used in the earlier study. In this work, we show that the sample prepared in the similar manner as the Ref. [25] (*procedure Ref*) cannot be the ideal $LiZn_2Mo_3O_8$, but shows significant deviation. It is certainly possible that our *procedure Ref* may not exactly reproduce the sample used in the earlier works. Hence, here we also compare the composition of the presently obtained sample to those estimated using the tabulated parameters in the earlier work [29]. First, for the previously reported sample without doping, the total deviation $x + y$ is estimated as 0.27(8) [29]. This is significantly worse than the $w = -0.1$ sample prepared in the present study ($x + y = 0.03(9)$). Second, on the other hand, the composition estimation from the reported lattice constants $a = 5.80163(3)$ Å and $c = 31.0738(2)$ Å [29] using the Vegard's law dependence shown in Fig. 3.3 gives a puzzling result; the $x + y$ parameter estimated from a is 0.05(3), whereas from c it is 0.60(11). This may indicate that the lattice constants cannot be simply parameterized by the sum $x + y$, but may depend on x and y individually. This would be the case if the deficiency at the Zn/Li sites becomes serious, *i.e.*, $x \gg y$. It should also be noted that in the earlier work [29], the supposedly non-dopoed $LiZn_2Mo_3O_8$ was investigated both by the SXRD and NPD measurements as noted in Sect. 1.2.2. The Li and Zn composition parameters for the primary phase can be evaluated from their structural parameters (occupancies), and are $x = 0.03(8)$ and $y = 0.244(10)$. This is certainly away from the values we have achieved in the present study ($x = -0.05(4)$ and $y = 0.08(8)$ for w = -0.1), indicating clear superiority of the present sample at least in the composition view point.

The second point is that the earlier doping-dependence work has been performed by removing Zn from the non-ideal $Li_{1+x}Zn_{2-y}Mo_3O_8$. As the Zn atoms are removed from the sample, the Li/Zn site deficiency becomes much serious. In contrast to the earlier work, our solid-state reaction technique minimize the deficiency for a large range of the nominal composition parameter w. Hence, from the structural viewpoint, our sample should provide much better playground to study the spin concentration effect to the $S = 1/2$ cluster TLAF.

On top of the above findings, we would like to compare the achieved hole-concentration (p) ranges in the earlier [29] and the present works. Shown in Fig. 3.7 is the schematic drawing of the hole-concentration ranges in the two works. For the estimation of the p-range for the earlier work, we assumed that the starting compound used in the Zn-removal study is the one reported in the SXRD/NPD study, as described above. While the range itself is

wider in the earlier work, the range reaches much closer to the stoichiometric $p = 1$ in the present study. It can be emphasized that from the physics point of view, the sample closer to the ideal composition was desired. It is again noted that our technique introduces less Li/Zn deficiency compared to the Zn removal technique, which is a more suitable condition for the magnetic property study.

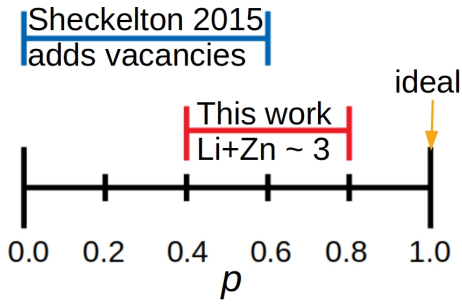

Figure 3.7: Ranges of the spin concentration achieve in the previous work [29] and this work. p stands for the fraction of the magnetic ($S = 1/2$) $[Mo_3O_{13}]^{11+}$ clusters to the total number of Mo_3O_{13} clusters.

3.2 Magnetic measurements of the series of $Li_{1+x}Zn_{2-y}Mo_3O_8$ with different compositions

As described in the previous section in detail, we have achieved polycrystalline sample preparation of $Li_{1-x}Zn_{2+y}Mo_3O_3$ with much closer composition to the ideal $LiZn_2Mo_3O_8$. In this section, we will report the results of the systematic study of magnetic properties for the series of LZMO samples with different spin concentration parameter p.

3.2.1 Magnetic susceptibility

Temperature dependence of the magnetic susceptibility ($\chi = M/H$) was observed for all the prepared samples described in the previous section. The external field for the magnetic susceptibility measurements was fixed to $H_{\mathrm{ext}} = 1\,\mathrm{T}$. The obtained magnetic susceptibility for all the samples is shown in Fig. 3.8. The representative results for selected samples are shown in Fig. 3.9. In the figure, two different groups of the samples were selected; $p = 0.42(13)$ and $0.57(7)$ as representative data for small p region, whereas $p = 0.78(15)$ and $0.64(7)$ as representative data for the samples closer to the ideal composition. Corresponding inverse susceptibility for the low-p samples is shown in Fig. 3.10.

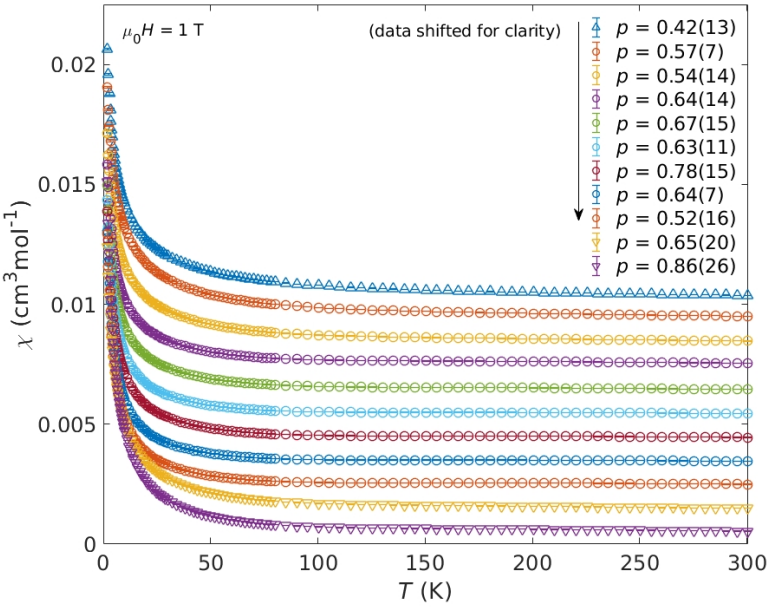

Figure 3.8: Magnetic susceptibility $\chi = M/H$ of all the polycrystalline LZMO samples prepared in the present study. External field of $H_{\text{ext}} = 1\,\text{T}$ was applied. p in the figure stands for the concentration of $S = 1/2$ spins estimated from the chemical composition.

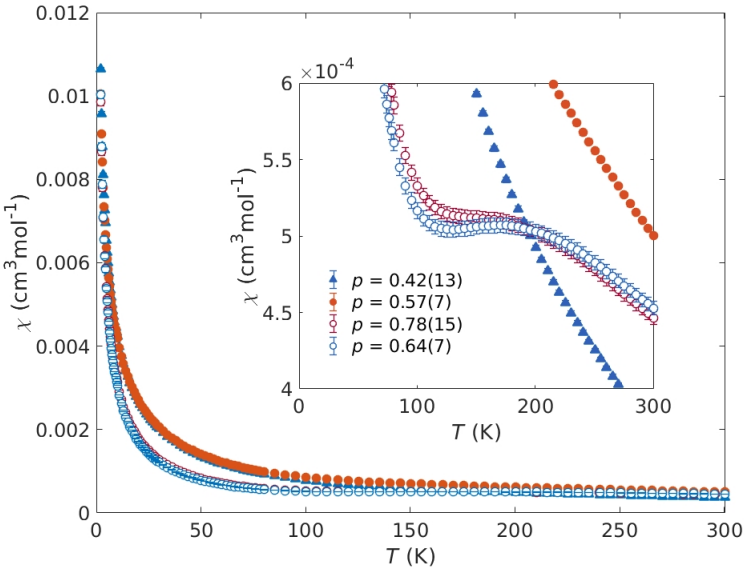

Figure 3.9: Magnetic susceptibility χ of four samples; two samples with $p = 0.42(13)$ and $0.57(7)$ as representatives for $p < 0.6$ region, whereas the two other samples with $p = 0.64(7)$ and $0.78(15)$ as representatives for $p > 0.6$ region. Inset: magnified figure to visualize the broad peak only observed in the $p \geq 0.6$ samples.

For $p = 0.42(13)$, where primary phase shows relatively large deviation from the stoichiometry, inverse susceptibility shows distinct linear behaviors for two temperature ranges; $T > 100\,\mathrm{K}$ and $T < 100\,\mathrm{K}$. The appearance of the two distinct slopes in the Curie-Weiss behavior is in good agreement with the results reported in the earlier study [25]. The Curie-Weiss fitting was performed for the two temperature ranges separately using weighted linear regression with $\chi^{-1} = (T - \theta)/C$ as the model function where the variance of χ^{-1} is used for the weight. From the Curie constant C, we found that the effective moment size for $150 < T < 300\,\mathrm{K}$ is $1.105(3)\,\mu_\mathrm{B}$, whereas it becomes greatly reduced at lower temperature as $0.807(1)\,\mu_\mathrm{B}$ for $10 < T < 70\,\mathrm{K}$ for the $p = 0.42(13)$ sample. This is also quantitatively consistent with the earlier results [25, 29].

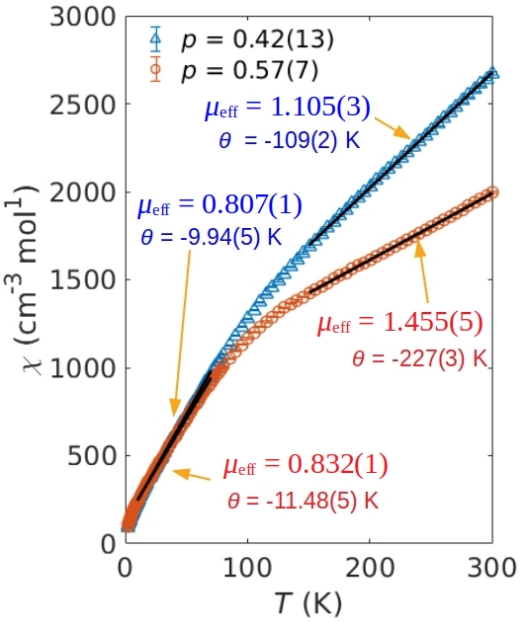

Figure 3.10: Inverse magnetic susceptibility χ^{-1} of two samples with $p < 0.6$. It may be noted that the inverse susceptibility is in good agreement with the earlier work proposing the two Curie-Weiss regimes. The unit for μ_{eff} is in μ_B.

For the samples with better composition $p > 0.6$, however, a prominently different feature was observed in the present study. As shown in Fig. 3.9 (and much clearly in its inset), the magnetic susceptibility exhibits a broad peak around $\sim$200 K, as exemplified by the samples with $p = 0.64(7)$ and $p = 0.78(15)$. Another key difference is the reduced magnetic susceptibility below $T \sim 50\,\mathrm{K}$ (shown in Fig. 3.9) for the improved $p > 0.6$ compared to the unimproved $p < 0.6$ composition samples. It is further suggested that the low-temperature upturn starts below 50 K, indicative of weakly and antiferromagnetically

interacting spins with the Weiss temperature of this temperature scale. In the very low temperature range ($T < 10\,\mathrm{K}$), the divergence of the susceptibility becomes much drastic compared to that expected for the Curie-Weiss behavior with moderate size of antiferromagnetic Weiss temperature. Therefore, in addition to the weakly interacting component, the existence of almost non-interacting spins may be suggested. In the next subsection, we will analyze the temperature dependence of the magnetic susceptibility much quantitatively.

3.2.1.1 Three-magnetic-component model

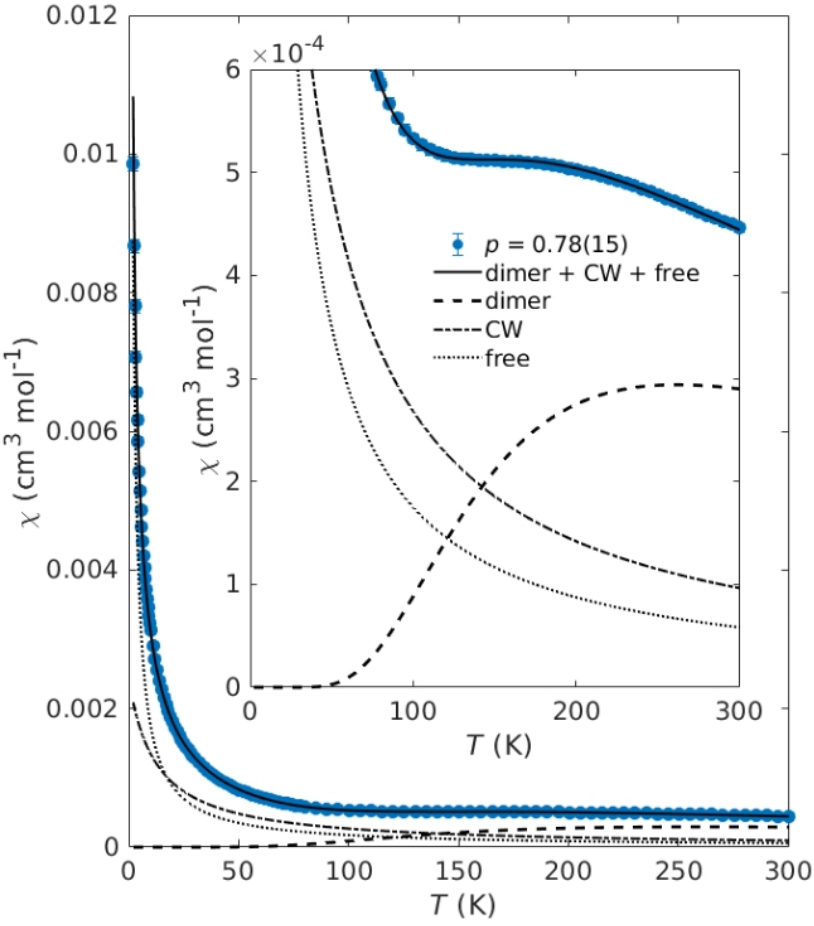

Figure 3.11: Magnetic susceptibility of $p = 0.78(15)$ sample fitted by three components.

As described in the previous section, there appears a new feature in the magnetic susceptibility in the improved composition samples ($p > 0.6$); a broad peak behavior at high temperature range $\sim 200\,\mathrm{K}$. On the other hand, we still noticed that there may

be two different Curie-Weiss behaviors at low-temperature region ($T < 100\,\mathrm{K}$); one is non-interacting C/T upturn, and the other is weakly interacting $C/(T-\theta)$ upturn with $|\theta| \leq 20\,\mathrm{K}$ (negative). This three-component behavior is in striking contrast to the two Curie-Weiss components used in the earlier study, which was indeed the basis for the claim of condensed valence-bond states envisaged in this material.

Here, we will analyze the magnetic susceptibility data for the samples in the whole p range achieved in the present study, and show that the three-component model works for the entire range $0.4 < p < 0.8$. Within the three-component model we assume the temperature dependence of the magnetic susceptibility as follows:

$$\chi = n(\mathrm{free})\frac{N_\mathrm{A} g^2 \mu_B^2}{4k_B T} + n(\mathrm{CW})\frac{N_\mathrm{A} g^2 \mu_B^2}{4k_B (T-\theta)} + n(\mathrm{dimer})\frac{N_\mathrm{A} g^2 \mu_B^2}{k_B T}\frac{1}{3+e^{J'/k_B T}}, \qquad (3.1)$$

where the first, the second and the last terms stand for the non-interacting Curie behavior (free), weakly interacting Curie-Weiss behavior (CW), and broad peak behavior (dimer), respectively. n(free), n(CW), and n(dimer) are the number fractions of $S = 1/2$ per Mo_3O_{13} clusters that contribute to the corresponding magnetic components. N_A, g, μ_B, k_B are the Avogadro constant, Landé splitting factor, Bohr magneton and Boltzmann constant, respectively. For the broad peak part, we tried several different trial functions, and found that the one used for the isolated antiferromagnetic dimers [45] works the best for the present datasets.

It is our final goal to show that the three-component model explains all the magnetic properties consistently for all the range $0.4 \leq p \leq 0.8$. For this purpose, the temperature dependence of the magnetic susceptibility was not sufficient to fix the free and weakly interacting terms. Hence, first, we use the isothermal magnetization measured at low temperatures to estimate the free and weakly interacting parts. A good fit to the isothermal magnetization at low-T can be made using two components: the Brillouin function representing free paramagnetic spin magnetic moments and a linear term that increases with the external magnetic field representing weakly interacting spins $\chi_\mathrm{CW}(T)$. For $S = 1/2$, the isothermal magnetization of the two magnetic components at a given T becomes:

$$M(T) = \frac{n(\mathrm{free}) g \mu_B}{2} \tanh \frac{g \mu_B H}{2k_B T} + \chi_\mathrm{CW}(T) H. \qquad (3.2)$$

At Fig.3.12 all the measured isothermal magnetizations at $T = 2\,\mathrm{K}$ for LZMO samples with $0.4 < p < 0.8$ are shown, together with the fitting results using Eq. 3.2. It can be

see in the figure that the model function Eq. 3.2 reproduces the experimental results very well for all the samples. From the fitting results, we obtained n(free), as will be used and discussed later.

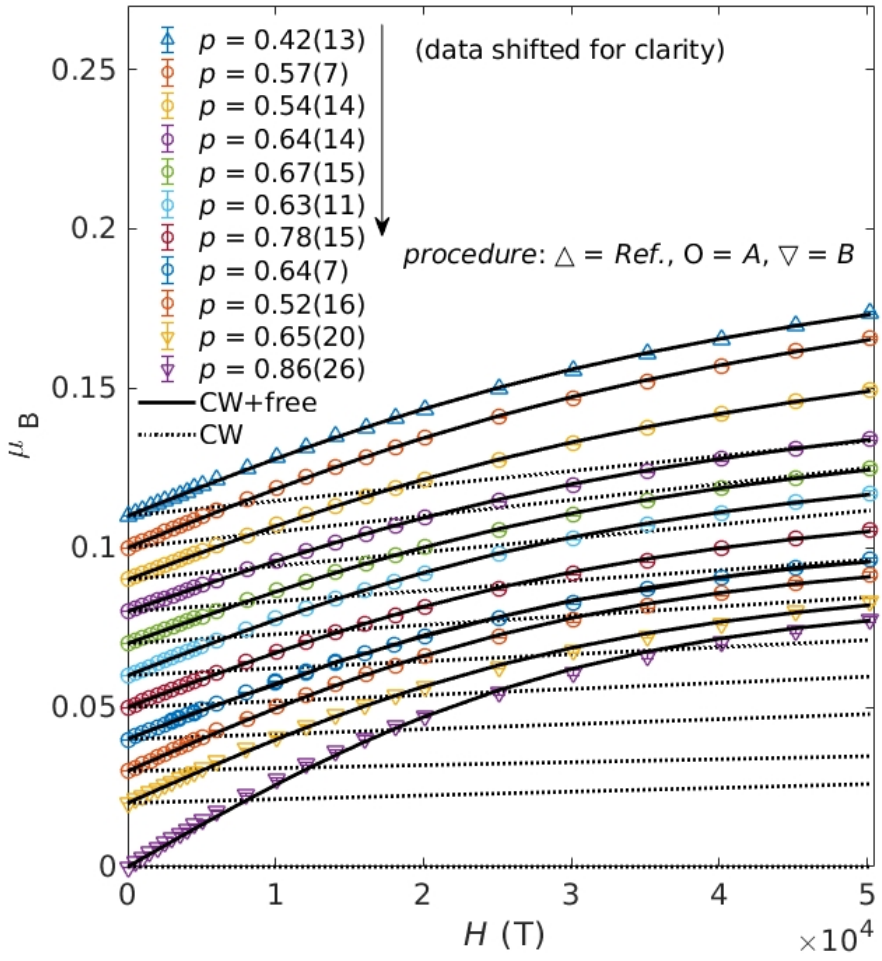

Figure 3.12: Isothermal field dependent magnetization up to $H = 5\,\mathrm{T}$ at $T = 2\,\mathrm{K}$ obtained with MPMS-XL magnetometer. Solid black lines are fits to the data involving the Brillouin function and a part that is linearly proportional to the field. The dashed black lines shows only the linear parts.

In addition to the low-field magnetization, we measured the high-field magnetization up to 28 T for the selected $p = 0.64(7)$ sample. The high-field magnetization for the $p = 0.64(7)$ sample is shown in Fig. 3.13. As can be clearly seen in the figure, there are two components; the low-field and high-field regions which show different bending behaviors. At higher magnetic field, the weakly interacting part should also deviate from

the linear behavior assumed in Eq. 3.2. Hence, to analyzer the high-field magnetization, we assume the two Brillouin functions as follows:

$$M(T) = \frac{n(\text{free})g\mu_B}{2} \tanh \frac{g\mu_B H}{2k_B T} + \frac{n(\text{CW})g\mu_B}{2} \tanh \frac{g\mu_B H}{2k_B (T-\theta)} \tag{3.3}$$

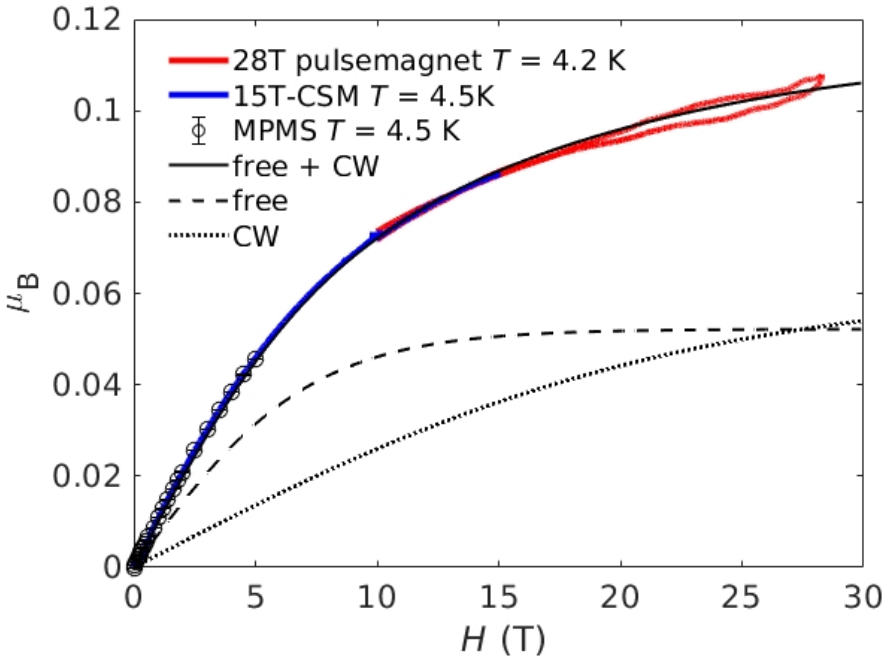

Figure 3.13: Isothermal magnetization of $p = 0.64(7)$ sample up to $\mu_0 H = 28\,\text{T}$ combined from data from three different magnets: 28T pulse magnet ($T = 4.2\,\text{K}$), 15T-CSM ($T = 4.5\,\text{K}$), and MPMS ($T = 4.5\,\text{K}$).

The fitting result is also shown in Fig. 3.13. Satisfactorily correspondence can be seen between the observation and fitting, indicating that indeed the low-temperature magnetization is dominated by the two (free and weakly interacting) component.

After knowing the n(free) for all samples by fitting the low-T magnetization measurements as described above, we tried to fit the temperature dependence of the magnetic susceptibility for all the p samples using the three-component model described by Eq. 3.1. The fitting results for all the p samples are shown in Fig. 3.14. It can be apparently seen that the three-component model explains very well the observed temperature dependence. The good correspondence unambiguously indicates that the dominant factor in the low-T and high-T region is the Curie-Weiss upturns and the dimer susceptibility, respectively.

It should be noteworthy that the broad peak behavior in the high temperature region can be captured by the three-component model. This cannot be achieved by the earlier two-Curie-Weiss-region model, and confirms the superior validity of the present three-component model. The resulting parameters from the fits to the isothermal magnetization and magnetic susceptibility are listed in Table 3.3.

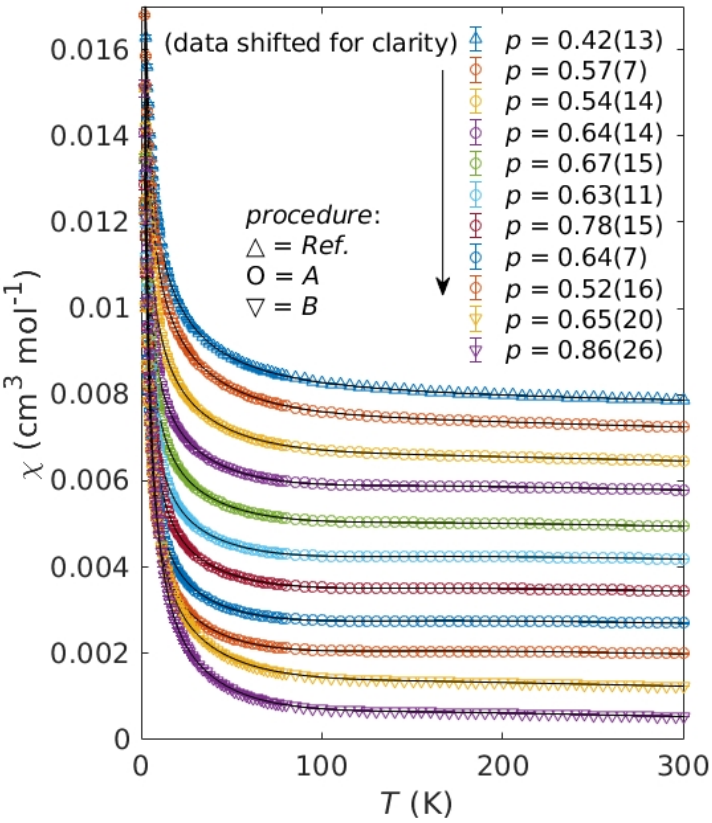

Figure 3.14: Magnetic susceptibility of all samples fitted by three components.

Table 3.3: Summary of the number of $S = 1/2$ per Mo_3O_{13} cluster contributing to three magnetic components in series of LZMO samples ($0.4 \leq p \leq 0.8$).

procedure	*Ref*	*A*	*A*	*A*	*A*	*A*
p	0.42(13)	0.57(7)	0.54(14)	0.64(14)	0.67(15)	0.63(11)
$n(free)$	0.046(1)	0.046(1)	0.043(1)	0.044(1)	0.046(1)	0.053(1)
$n(CW)$	0.211(1)	0.233(1)	0.181(1)	0.150(1)	0.117(1)	0.085(1)
Θ (K)	-16.2(1)	-19.9(1)	-18.1(2)	-18.6(3)	-15.6(3)	-13.9(3)
$n(dimer)$	0.165(2)	0.337(2)	0.369(5)	0.521(5)	0.436(4)	0.465(4)
$n(J'/k_B$ (K))	-433(3)	-430(2)	-426(4)	-412(3)	-420(3)	-422(3)
procedure	*A*	*A*	*A*	*B*	*B*	
p	0.78(15)	0.64(7)	0.52(16)	0.65(20)	0.86(26)	
$n(free)$	0.053(1)	0.056(1)	0.065(2)	0.065(2)	0.089(4)	
$n(J)$	0.091(1)	0.079(1)	0.087(1)	0.145(1)	0.110(1)	
Θ (K)	-12.4(2)	-12.7(3)	-17.3(4)	-16.9(3)	-11.8(3)	
$n(dimer)$	0.462(4)	0.480(4)	0.513(4)	0.439(5)	0.513(6)	
$n(J'/k_B$ (K))	-420(3)	-414(3)	-413(3)	-433(4)	-423(4)	

The number fractions as well as the Weiss temperature and dimer exchange are plotted in Fig. 3.15. The data from four samples with a large secondary phase ($(1 - z) > 10\%$) are omitted from the figure.

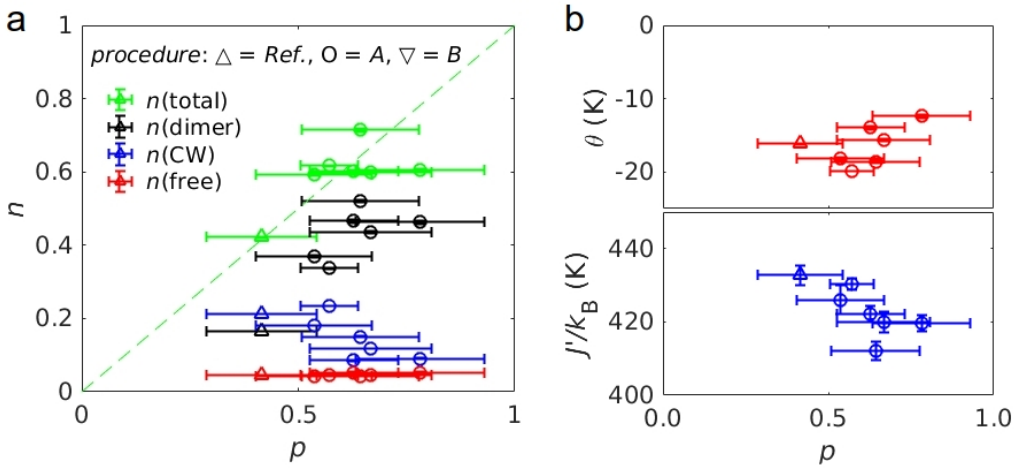

Figure 3.15: (a) The p dependence of the number of spins contributing to free, weakly interacting and dimer spins. Number of total spins per Mo_3O_{13} cluster is also shown. The dashed line stands for the expected total spins in terms of p. (b) The p dependence of the Weiss temperature θ and the dimer exchange J' shown in the upper and lower panel, respectively.

From the parameters summarized in Table. 3.3 and Fig. 3.15 some p dependent trends can be seen. Let us discuss the trends on number fractions one by one. First, n(free) seems p-independent. On the other hand, n(CW) decreases as p becomes larger. This decrease was already expected in the raw susceptibility datasets. Weiss temperature stays within $\theta < 20\,\mathrm{K}$ but scatters. n(dimer) shows clear increase with increasing p. The dimer exchange J' seems to be constant for all the p values. It may be noted that the total number of spins is roughly consistent to that expected from the p value of samples. This

p-dependence of the magnetic components strongly suggests that the dimer spins will become more and more dominant over the other components with increasing p. This indicates that the intrinsic magnetism in LZMO is singlet dimer formation.

3.2.2 Electron spin resonance and specific heat

In order to test the three-magnetic-component model using other experimental data, we will show the ESR and specific heat measurements on selected samples. First, the ESR measurement was performed on the $p = 0.64(7)$ sample. At the base temperature $T = 4.2\,\mathrm{K}$ a broad and a sharp peaks are found for the four different microwave freaquencies $f = 135$, 190, 270, and 360 GHz (Fig. 3.16). Both the broad and sharp peaks are fitted with Gaussian functions. The frequency dependence of the peak center provides g-factors as 2.05(27) and 1.881(8) for the broad and sharp peaks, respectively. The g-factor extracted from the sharp peak is consistent with that reported earlier [28].

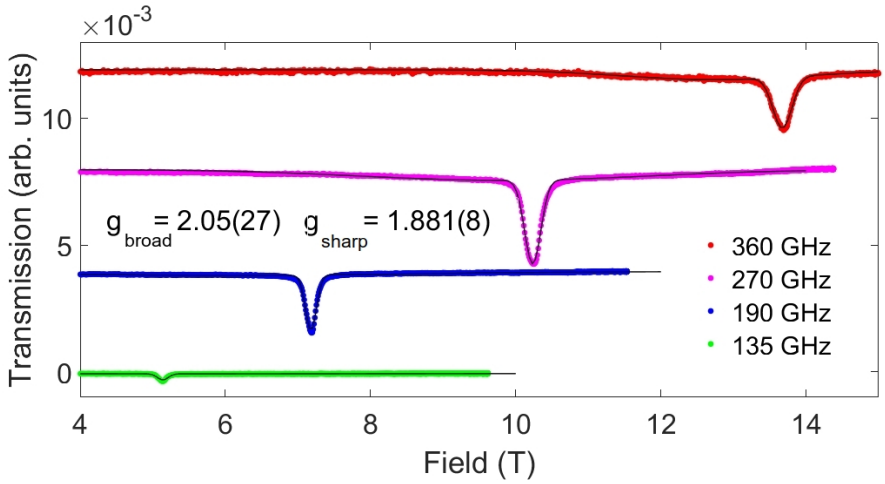

Figure 3.16: Frequency dependence of ESR spectra at $T = 4.2\,\mathrm{K}$ using the LZMO $p = 0.64(7)$ sample.

The temperature dependence ($4.2 < T < 70\,\mathrm{K}$) of the ESR spectrum with $f = 360\,\mathrm{GHz}$ is also measured (Fig. 3.17). The data are treated similarly by fitting the broad peak and sharp peaks to Gaussians and their integrated intensities are shown in Fig. 3.18. According to the Boltzmann distribution, the ESR intensity of a $S = 1/2$ free paramagnetic spin can be described as:

$$I(\mathrm{free}) = \tanh \frac{g\mu_\mathrm{B}B}{2k_\mathrm{B}T}. \tag{3.4}$$

We assume that the ESR intensity for the weakly interacting spins may be written by just adding the Weiss temperature:

$$I(\mathrm{CW}) = \tanh \frac{g\mu_{\mathrm{B}} B}{2k_{\mathrm{B}}(T-\theta)}. \tag{3.5}$$

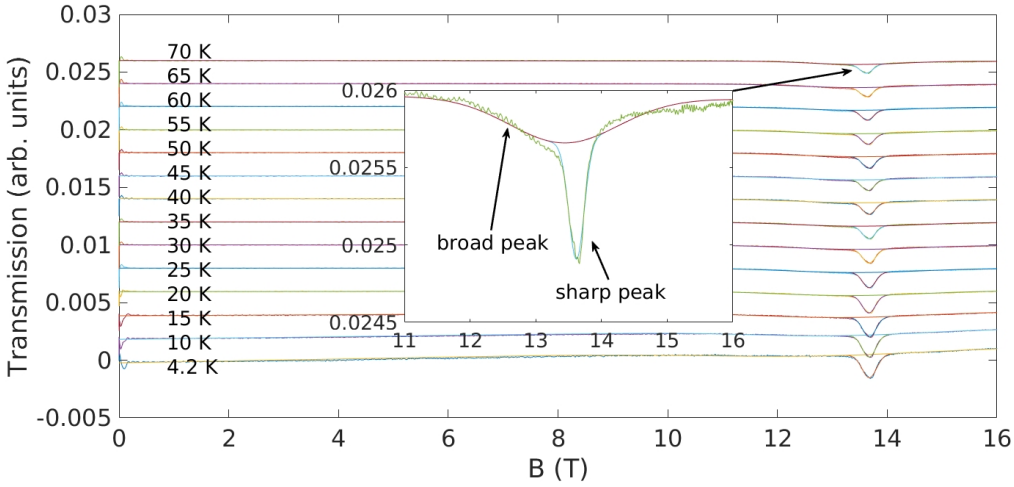

Figure 3.17: Temperature dependence ($4.2 < T < 70\,\mathrm{K}$) of ESR spectra for $p = 0.64(7)$ sample. The inset shows a magnified view of the sharp and a broad peak at $T = 70\,\mathrm{K}$.

As for the dimer spins, we expect that majority of them is in singlet states ($S = 0$ which will show no ESR signal) even at $T = 70\,\mathrm{K}$ with the large $J' \sim 430\,K$. Therefore, we can assign the remaining free spins and weakly correlated spins to the sharp and broad peaks, respectively. The integrated intensities along with their fits (Eqs. 3.4, and 3.5) are shown in Fig. 3.18.

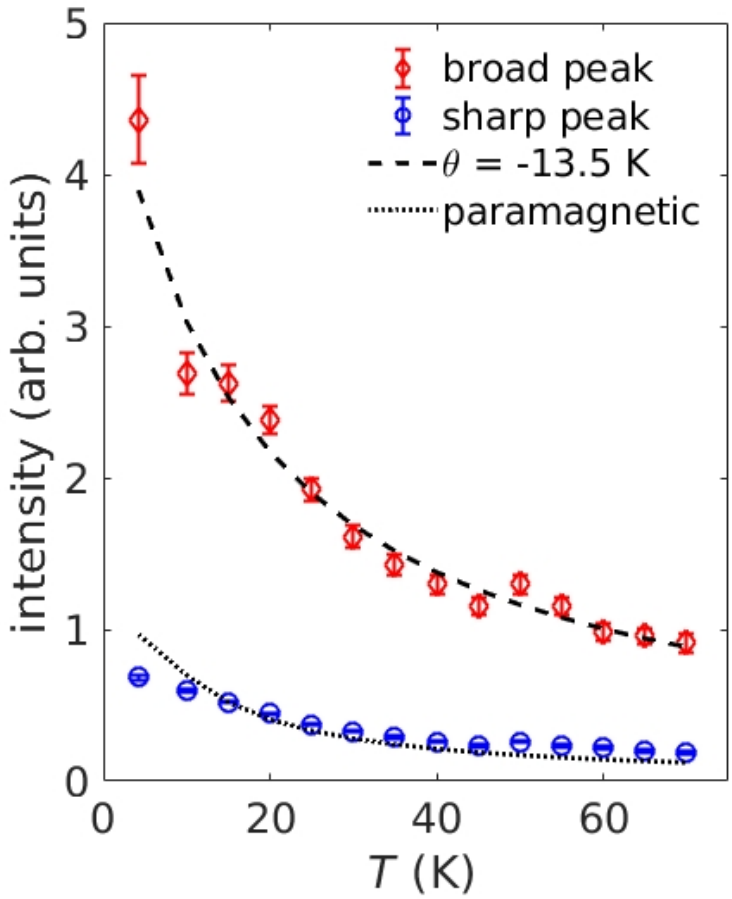

Figure 3.18: The temperature dependency of ESR peak integrated intensities.

We can argue that for suffiently large T the Eqs. 3.4 and 3.5 asymptotically become the Curie and Curie-Weiss laws, respectively. Therefore, the fits to the integrated intensities (Fig. 3.18) are roughly consistent with the three-magnetic-component idea. From this data it is hard to make a quantitative comparison with the free and weakly interacting spins. This is because the absolute value of the integrated intensities of the broad peak heavily depends on how the background of the ESR signal is treated while for the sharp peak integrated intensity is rather well defined.

We also performed the specific heat measurement for the p = 0.78(15) sample below $T < 5\,\mathrm{K}$. The purpose was to measure the magnetic upterm that had been previously reported [25]. The specific heat divided by temperature as a function of the temperature is shown in Fig. 3.19. The previously reported result [25] is also shown. The $p = 0.78(15)$ sample shows a reduction in the size of the magnetic upterm by a factor of 1.5 compared

to the result of [25]. As we have discussed earlier, the sample used in Ref. [25] has likely worse composition compared to the present $p = 0.78(15)$ sample. Therefore, it is natural to assume that the reduction of the magnetic upterm is related to the improvement of composition. Thus, the magnetic upterm might be related to the free spins and weakly interacting spins.

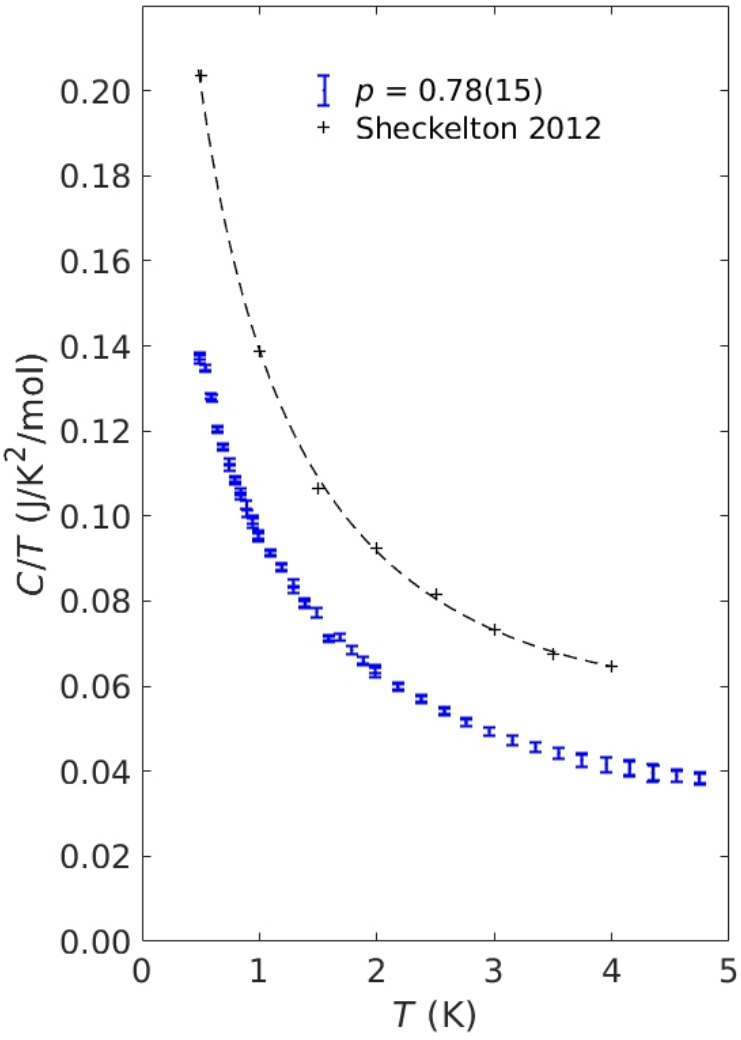

Figure 3.19: Specific heat below $T < 5\,\mathrm{K}$ for $p = 0.78(15)$ shown as blue points. Data taken from the previously reported result [25] is shown as black crosses and connected with a guide to the eye as a black dotted line.

3.3 Neutron scattering of best composition $Li_{1+x}Zn_{2-y}Mo_3O_8$

We have improved the solid state reaction that allowed us to synthesize a series of $Li_{1+x}Zn_{2-y}Mo_3O_8$ samples with a $S = 1/2$ concentration range of $0.4 < p < 0.8$. With these samples, we performed magnetic measurements that suggests the three magnetic components, n(free), n(CW), and n(dimer), in $Li_{1+x}Zn_{2-y}Mo_3O_8$. By increasing the composition closer to the more ideal value, the dimer component became dominant. This suggests that the intrinsic ground state of LZMO might be a dimer singlet. The dimer exchange energy $J' \sim 37$ meV was obtained from the isolated dimer susceptibility [45].

In order to confirm the postulated idea for the singlet dimer formation, it is beneficial to observe the singlet-triplet excitations using spectroscopic means. In this section, we will report results of our neutron inelastic scattering experiments to detect any inelastic scattering signals which can be related to the singlet-triplet excitations.

3.3.1 High Resolution Chopper spectrometer

The magnetic form factor of the Mo_3O_{13} cluster was estimated in Ref. [27]. The form factor decays quickly as Q becomes larger, and indeed even at $Q = 1\,\text{Å}^{-1}$, the magnetic signal may not be observable. This places tight requirements on the momentum-energy-transfer coverage that could be accessed by a given neutron scattering spectrometer (see. Fig. 2.5). As noted in the experimental details, HRC can access a small Q region with a reasonable energy-transfer range by providing a high-incident-energy neutrons and utilizing a small-angle detector banks equipped uniquely to this spectrometer. Using HRC, we investigated neutron inelastic scattering spectrum in a very small Q region, where previous work could not reach.

The momentum-energy range of neutron scattering intensity was measured at $T = 5$ and 295 K. The resulting intensity maps obtained from the low- and wide-angle detectors are shown in Fig. 3.20. The low-temperature (5 K) spectrum in the low-Q range (Fig. 3.20(a)) shows relatively strong scattering intensity around $\hbar\omega \sim 20$ and 55 meV. They are almost Q-independent in this Q-region, suggesting that they originates from localized modes. By increasing the temperature to 295 K (Fig. 3.20(c)), the scattering intensity below 20 meV drastically increases, and the $\hbar\omega \sim 20$ meV peak is smeared into the so-called quasielastic signal, a continuum scattering extending from the elastic position. The $\hbar\omega \sim 55$ meV peak does not show significant change, indicating its temperature independent origin.

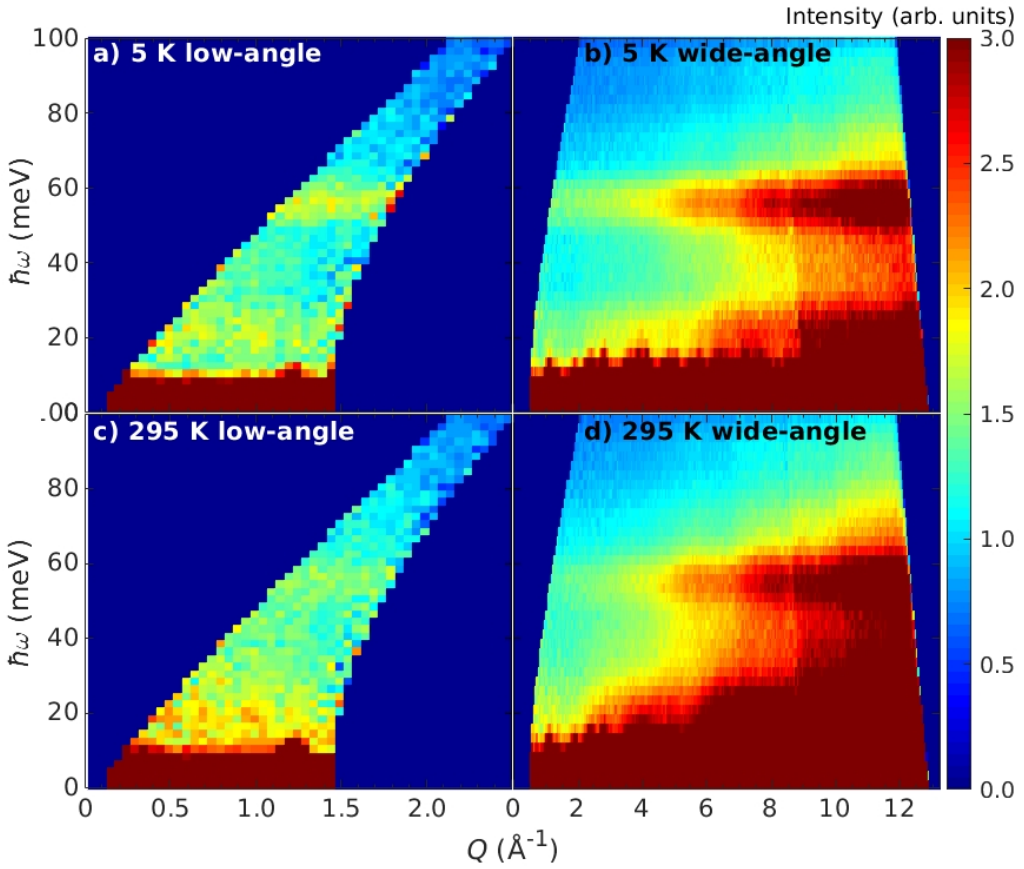

Figure 3.20: Neutron scattering intensity at $T = 5\,\mathrm{K}$ and $T = 295\,\mathrm{K}$ obtained by incident neutron energy $E_\mathrm{i} = 311\,\mathrm{meV}$ using HRC low-angle $0.6 < 2\theta < 7.0°$ and wide-angle $2\theta > 3.0°$ detectors. All intensities have been normalized by proton count and have had background subtracted. Low-angle intensities have been multiplied by a factor of 20 to fit the common scale.

The appearance of the high temperature quasielastic scattering is normal; it indicates that spins are thermally fluctuating at 295 K. On the other hand, appearance of the peak behavior at $\hbar\omega \sim 20\,\mathrm{meV}$ and related decrease of the scattering intensity below 20 meV is not trivial, and indeed suggests formation of spin excitation gap at 5 K.

To show the temperature dependence of the low-Q scattering intensity, the low-angle data in the Q range $0.48 < Q < 1.03\,\mathrm{Å}^{-1}$ have been integrated. The resulting integrated intensity is shown as a function of energy-transfer $\hbar\omega$ in Fig. 3.21. At high energies $\hbar\omega > 20\,\mathrm{meV}$, the scattering intensity seems almost temperature independent, whereas clear gap formation can be seen in the low-energy region $\hbar\omega < 20\,\mathrm{meV}$.

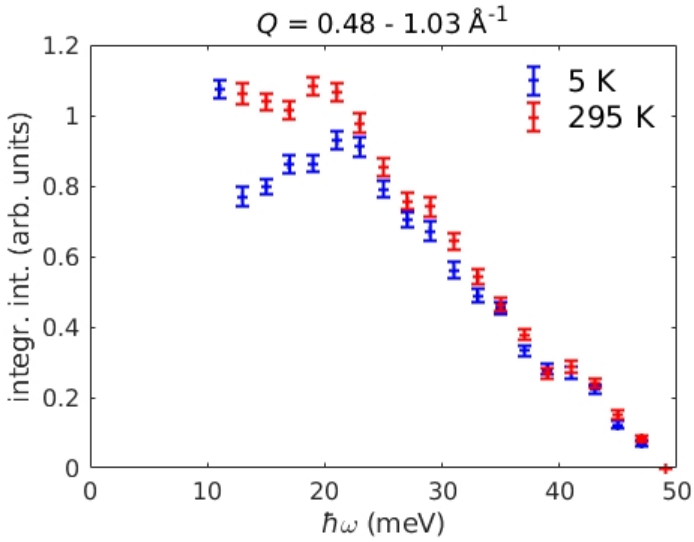

Figure 3.21: Energy dependence of the neutron scattering intensity in the region $0.5 < Q < 1.0$.

To see the origin of the temperature dependence, we convert the scattering intensity to the imaginary part of the dynamical susceptibility using the following relation:

$$S(Q, \hbar\omega) \propto (1 - \exp(-\hbar\omega/k_{\mathrm{B}}T))^{-1}\mathrm{Im}\chi(Q, \hbar\omega), \tag{3.6}$$

where $(1-\exp(-\hbar\omega/k\mathrm{B}T))^{-1}$ is called detailed balance factor. The resulting $\mathrm{Im}\chi(Q, \hbar\omega)$ is shown in Fig. 3.22. It should be noted that if the excitation has bosonic origin, such as phonons and magnons, the dynamical susceptibility may be temperature independent as long as boson density is small. In contrast, the observed $\mathrm{Im}\chi(Q, \hbar\omega)$ shows clear increase at the low temperature, excluding the trivial magnonic or phononic origin of the inelastic intensity in this energy range. It is rather suggested from the raw spectra that a gap with energy scale $\sim 20\,\mathrm{meV}$ is formed at the low temperatures in LZMO with the more ideal composition.

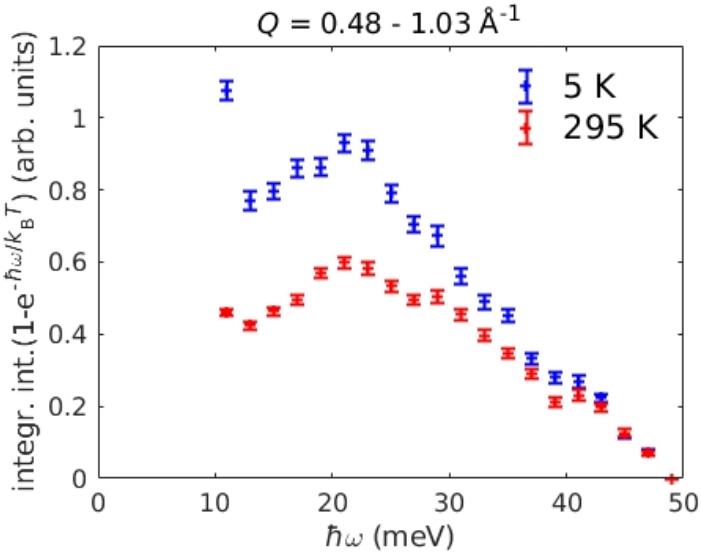

Figure 3.22: Energy dependence of the neutron scattering intensity in the region $0.5 < Q < 1.0$ normalized by the detailed balance factor.

In the high-Q intensity maps shown in Fig. 3.20(b) and Fig. 3.20(d), two clear features may be seen. One is the almost Q-independent inelastic signal at $\hbar\omega \sim 55\,\mathrm{meV}$, which continues to the low-Q region as discussed in the above. The other is strongly enhanced low-energy intensities at the high temperature 295 K in high-Q range. The increasing behavior of the neutron scattering intensity in the high-Q range indicates that both of them are from phonon scatterings. Nevertheless, for the $\hbar\omega \sim 55\,\mathrm{meV}$ peak should be given a further attention, since the intensity still remains at very low-Q range (in the small-angle detector bank). To see the Q-dependence of the 55 meV peak much clearly, we plot the $\hbar\omega$-integrated intensity as a function of Q in Fig. 3.23. It can be clearly seen in the figure that the intensity decreases monotonically to $Q \to 0$, however, somehow it saturates below $Q < 3\,\mathrm{Å}^{-1}$. Also noted is that the temperature dependence starts to appear below this Q. Those two features suggest that a part of the 55 meV intensity may be of magnetic origin. However, judging from the magnetic form factor of the Mo_3O_{13} cluster, this possibility may be unlikely. The origin of the 55 meV peak is unclear at the present moment, and further study is apparently necessary to understand it.

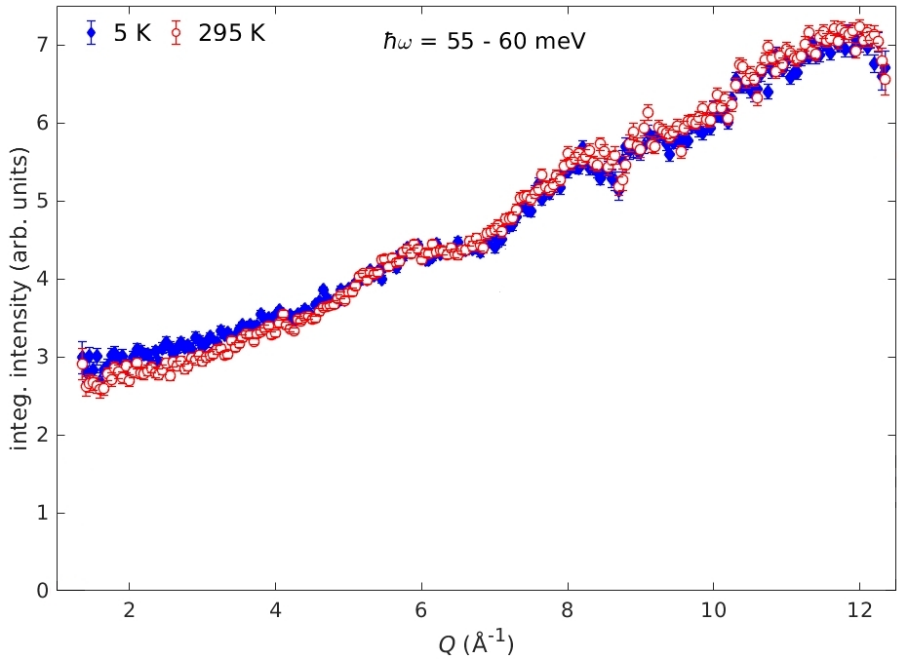

Figure 3.23: Constant $55 \leq \hbar\omega \leq 60\,\text{meV}$ cut along Q. From $Q > 4\,\text{Å}^{-1}$ the intensity stays almost constant.

3.3.2 Polarized triple-axis spectrometer

The magnetic scattering in low-energy range was observed using the PTAX spectrometer with polarization analysis. All four channels with either horizontal or vertical guide field (HF or VF) and either spin flippers on or off are measured in this experiment. The resulting scattering intensity in all the four channels for the, the elastic-position is shown in Fig. 3.24, measured with $E_\text{f} = 13.7\,\text{meV}$. It shows weak but finite magnetic signal at at the base temperature T = 4.5 K. By properly analyzing the intensity from the four channels, we estimate magnetic scattering contribution solely, which is shown in Fig. 3.25. Although statistics is not sufficient, we can conclude that there is a weakly Q dependent magnetic signal developed at 4 K in vicinity of the elastic channel, indicative of the development of weak antfiferromagnetic short-range order. This magnetic signal is related to the one observed as the gapless continuous signal in the earlier work [27], however, here we would like to emphasize that its magnetic origin is for the first time confirmed using the polarization analysis in the present work. In view of the emergence of spin gap behavior in much higher energy range, which should be related to the singlet dimer formation, we now ascribe this low-energy fluctuation to the remaining weakly interacting spins deduced in the magnetic susceptibility study.

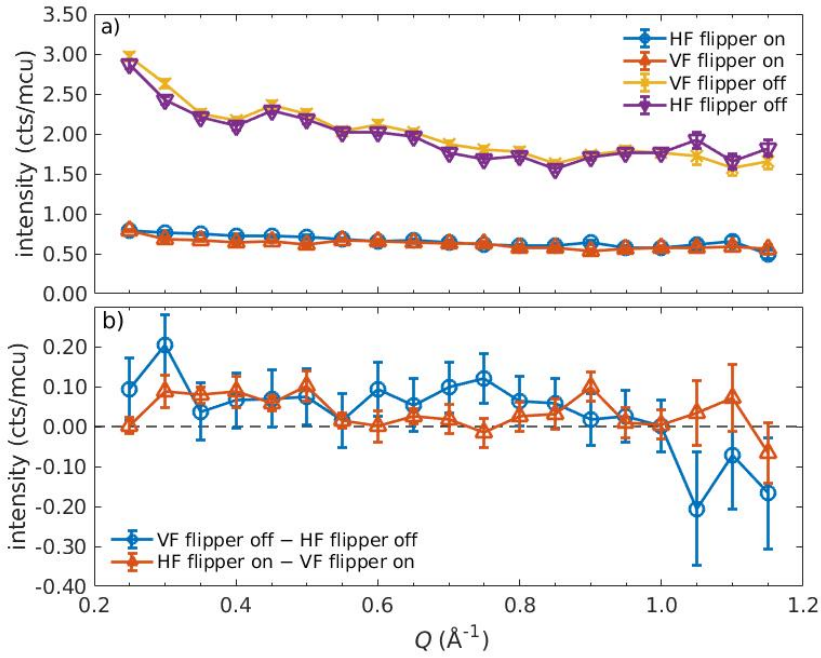

Figure 3.24: (a) Elastic Q-scan at $E_f = 13.7\,\text{meV}$ and at $T = 4.5\,\text{K}$. The four measured channels with either HF (horizontal guide field) or VF (vertical guide field) and either spin flippers on or off are shown. (b) Magnetic contribution by subtraction of the flipper off channels or on channels.

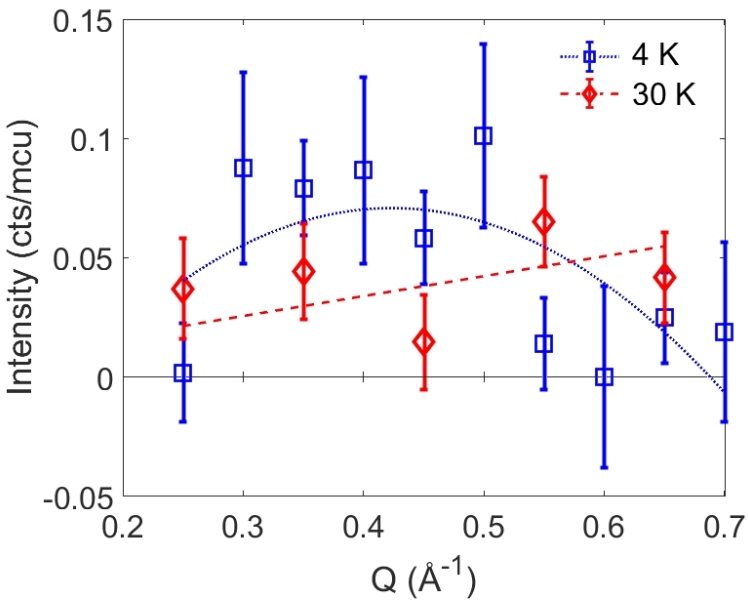

Figure 3.25: Temperature dependence of the magnetic signal at $\hbar\omega = 0$ and at $T = 4.5, 30\,\text{K}$.

3.3.3 Hybrid Spectrometer

Using the Hybrid Spectrometer (HYSPEC) we can observe the $\hbar\omega \sim 20\,\text{meV}$ excitation with better energy resolution but with worse momentum-energy-transfer coverage compared to HRC. This will allow us to see below the $\hbar\omega \sim 20\,\text{meV}$ excitation that is obscured in the data obtained by HRC because of the huge tail of the quasielastic scattering.

The neutron inelastic scattering intensity was measured with incident neutron energy $E_\text{i} = 60\,\text{meV}$ at $T = 1.7$ and $200\,\text{K}$. The resulting intensity maps are shown in Fig. 3.26. The low-temperature ($1.7\,\text{K}$) spectrum shows a lowering of scattering intensity in the low-Q range at $10\,\text{meV}$. This might be that the $\hbar\omega \sim 20\,\text{meV}$ excitation is a gapped excitation. Another feature is the is the phonon mode at $\hbar\omega \sim 20$ extending up to high-Q with increasing intensity.

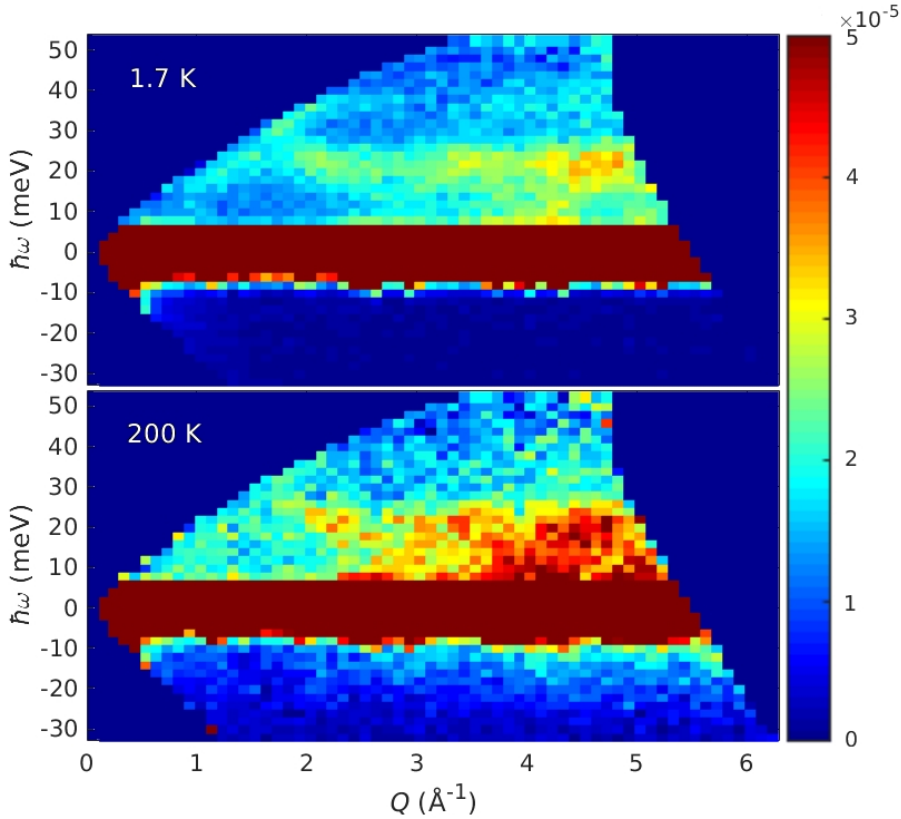

Figure 3.26: Neutron scattering intensity at $T = 1.7$ and $200\,\text{K}$ obtained by incident neutron energy $E_\text{i} = 60\,\text{meV}$.

To observe the temperature dependence of low-energy spin-fluctuations, we measurend inelastic scattering spectra using the low incident neutron energy $E_\text{i} = 9\,\text{meV}$ at the five

temperature points $T = 1.7$, 30, 80, 160, and 300 K. The resulting intensity maps for all temperatures obtained are shown in Fig. 3.27. Unfortunately, there is an apparently temperature independent artifacts at $\hbar\omega \sim 2$ at almost the entire Q-range making the data very challenging to analyze. Nonetheless, comparing the $T = 1.7$ K to the $T = 30$ K data we can see a slightly greater intensity at $Q \sim 0.5\,\text{Å}^{-1}$ at the lower temperature compared to that at the higher temperature for $\hbar\omega < 2$ meV. This is qualitatively consistent with the apparently gappless low-energy spin fluctuations observed in previous work [27].

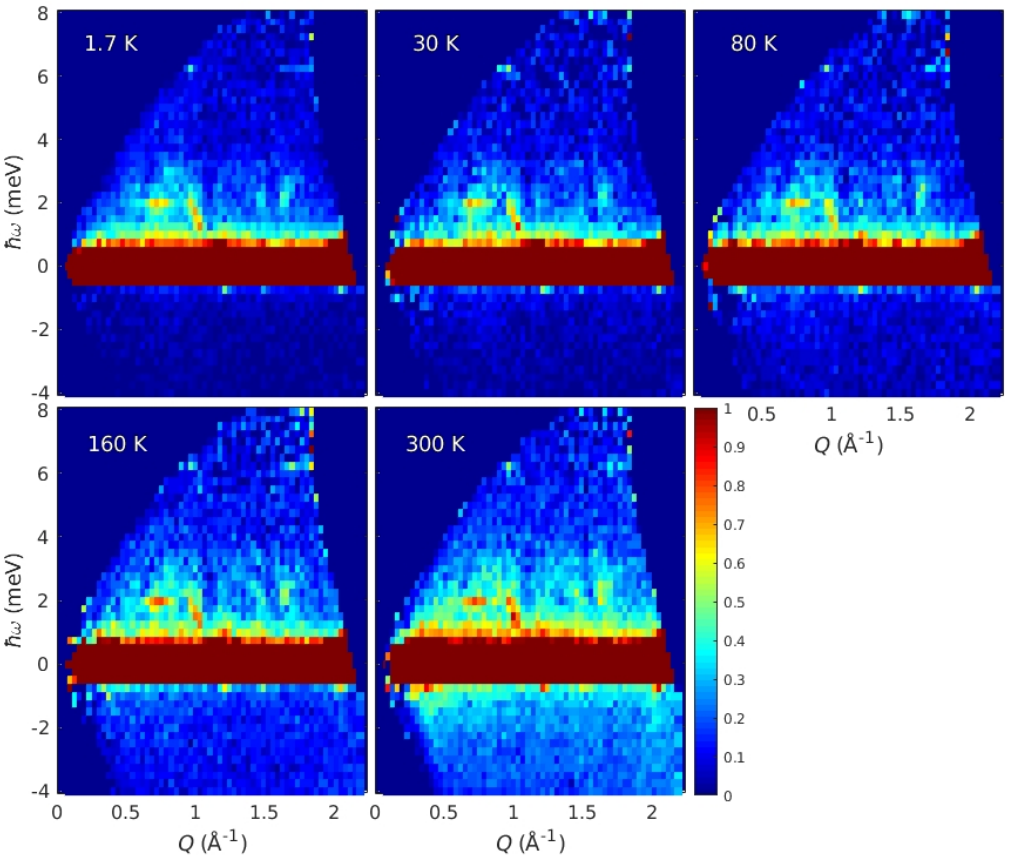

Figure 3.27: Neutron scattering intensity at $T = 1.7$, 30, 80, 160 and 300 K obtained by incident neutron energy $E_\text{i} = 9$ meV. The empty sample cell data has been subtracted.

4 Discussion

Motivated by the exotic condensed valence-bond ground state in $LiZn_2Mo_3O_8$ postulated by earlier work, together with the fact that the offstoichiometric sample used in the study casts some doubt on this intriguing ground state, we conducted this work. First, a thorough study to control the composition of LZMO was done in order to study the magnetic properties of the series of compounds with different composition to investigate what the intrinsic ground state is, and to tune the composition as close to the stoichiometry as possible. Finally, using the best sample, we performed neutron scattering experiments to observe the spin excitations.

All the magnetic studies consistently suggest three spin components, *i.e.*, non-interacting (Curie law), weakly-interacting (Curie-Weiss), and dimer-forming spins. As p becomes closer to the ideal value ($p = 1$), the non-interacting and weakly-interacting components seem to decrease, whereas the dimer spins increase. This suggests that the intrinsic ground state of LZMO may be rather simple dimer singlet state. The neutron inelastic scattering is also qualitatively consistent with the three-component model. In this chapter, we discuss the present results by comparing them to the earlier works, and also discuss possible origin for the dimer formation.

4.1 Comparison to the earlier works

In the ealier work [25], from the two Curie-Weiss regions observed in the inverse magnetic susceptibility, it was concluded that 2/3 of spins disappear below $T \sim 96\,\mathrm{K}$. This was the basis of the argument that LZMO forms the intriguing condensed valence-bond state at the base temperature. In the present work, by increasing the spin concentration per Mo_3O_{13} cluster to $p = 0.78(15)$ (closer to the ideal unity), we clearly observed a broad peak behavior in the temperature dependence of the magnetic susceptibility around $T \sim 200\,\mathrm{K}$. This suggests the formation of dimer singlet in this material. In accordance to the dimer singlet formation, the neutron inelastic scattering indicates possible spin

gap formation of the gap size $\Delta \sim 20\,\mathrm{meV}$.

In the earlier neutron scattering work [27], the low-energy spin fluctuations were detected at the low temperature ($T = 1.7\,\mathrm{K}$) in the energy range of $\hbar\omega < 2\,\mathrm{meV}$ and $Q \sim 0.4\,\mathrm{\AA}^{-1}$. This low-energy scattering was related to the spin excitations in the nearest-neighbor and next-nearest-neighbor dimers in the postulated condensed valence-bond state. We also observed similar magnetic signal in the low energy region, and further confirmed its magnetic origin by using neutron polarization analysis. Nonetheless, we think the low-energy spin fluctuations can be attributed to the other origin, the weakly correlating spins. As the magnetic susceptibility study suggests, the energy scale for the dimer formation is quite large as $J' \sim 400\,\mathrm{K}$. Although not quantitatively consistent, the spin gap detected in the neutron inelastic scattering is also of the order of 20 meV. Hence, we think that the low-energy spin fluctuation cannot be due to the intra-dimer spin coupling. On the other hand, the present magnetic study indicates existence of weakly interacting spin component. The energy scale of the weakly interacting component may be estimated as $\sim 20\,\mathrm{K}$ from its Weiss temperature. This energy scale is in good agreement with the energy range where low-energy spin fluctuation was detected in the earlier and the present works. Hence, we think that the magnetic fluctuations appearing in the low energy range are attributable to the weakly interacting spins. This, in turn, supports the idea of three-component model, from microscopic viewpoint.

Earlier work did doping dependence study in range of $0 < p < 0.6$ by vacating Zn sites. Two Curie-Weiss regions persist with lowering p. We would like to point out that our study largely replaces Zn by Li, instead of just removing Zn, and thus the effect of deficiency at the Li/Zn site should be minimal in our sample. Also noted may be the fact that the three-component model proposed in the present study indeed reproduced well the temperature dependence of the magnetic susceptibility for $0.4 < p < 0.6$, where the two-Curie-Weiss regions were assumed in the earlier work. We could not obtain samples with much lower p, and hence, we cannot conclude how low the three-component model can explain the magnetic behavior. Nonetheless, we would like to argue that the three-component model is a good starting point to discuss the magnetic properties in a wide p range.

4.2 Origin of the dimer formation

Among the three spin components suggested in the above, the key component may be the one forming spin dimers, as this survives and dominates for $p \to 1$. The origin of the

dimer formation is the next question.

As is discussed in the Introduction, there may be a chance for the TLAF with weaker U to form an intriguing non-magnetic insulator phase [10–12]. Hence the dimer formation observed in the present work may be related to this intriguing singlet phase. It should be noted that since our sample was, although becoming much better than those in the earlier work, not perfect, but still $p = 0.78(15)$. Hence, we have 22% of $[Mo_3O_{13}]^{12+}$ non-magnetic clusters. This cluster is electronically "hole", and hence would assist spins around the hole to form spin dimers. This way, the spin dimers may be formed in the triangular lattice plane.

This "in-plane" dimer formation, however, has one counter argument. Electron doping study on the related compound $Li_2Sc_{1-x}Sn_xMO_3O_8$ [18] shows that no dimer formation can be seen in whole electron concentration (see Fig. 1.13). This is clearly different from the present LZMO sample. One significant difference between the $Li_2AMo_3O_8$ and the present LZMO systems is the stacking of the trimer-triangular lattice; in LZMO, we have two-combined-triangular-layers (bilayer) stacking in the ABC sequence, while in $Li_2AMo_3O_8$, the single triangular layer stacks in the AB sequence. Hence, it may be suggested that the bilayer nature is the key to form the dimer singlet in the LZMO system. The arrangement of the two Mo_3O_{13} clusters in the bilayer unit is shown in Fig. 4.1(a), which should be contrasted to the in-plane dimer formed by the two in-plane adjacent clusters shown in 4.1(b).

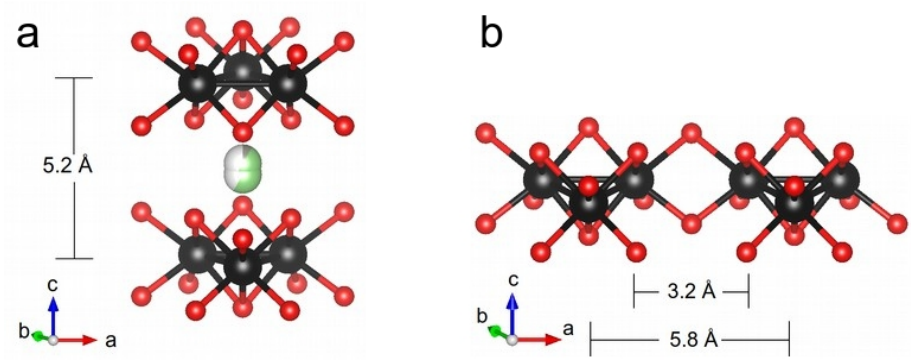

Figure 4.1: Illustration (a) of bilayer Mo_3O_{13} clusters that are each others nearest-neighbors in the c-direction; (b) of in-plane Mo_3O_{13} clusters. For each cluster there are six nearest-neigbors in the ab plane.

In the following, we discuss the bilayer possibility in more detail, however, we would like to state here that the other "in-plane" dimer possibility should, of course, be given equal scrutiny in future.

4.3 Statistical counting of bilayer dimer probability

Here, we discuss the number of bilayer dimers expected solely from the statistical view point, and compare the result with our observations. Assume that the probability of the Mo_3O_{13} cluster to be filled by $S = 1/2$ spin is p. (Note that this p is the same as the p parameter used for the density of the $S = 1/2$ spin per Mo_3O_{13} cluster.) A simple statistical calculation provides the probabilities for appearance of the bilayer dimers, in-plane nearest-neighbor dimer, and non-interacting spins as follows:

$$\begin{aligned} n(\text{dimer}) &= p^2 \\ n(\text{CW}) &= (1-p)p[1-(1-p+p^2)^6] \\ n(\text{free}) &= (1-p)p(1-p+p^2)^6 \end{aligned} \tag{4.1}$$

Figure. 4.2 shows the expected p-dependence of each probability, along with our estimation of corresponding n(free), n(CW) and n(dimer). Although the experimental uncertainty is quite large, at least, our statistical estimate is not so far from the observation. Hence, we could suggest that the bilayer dimers may be formed in LZMO.

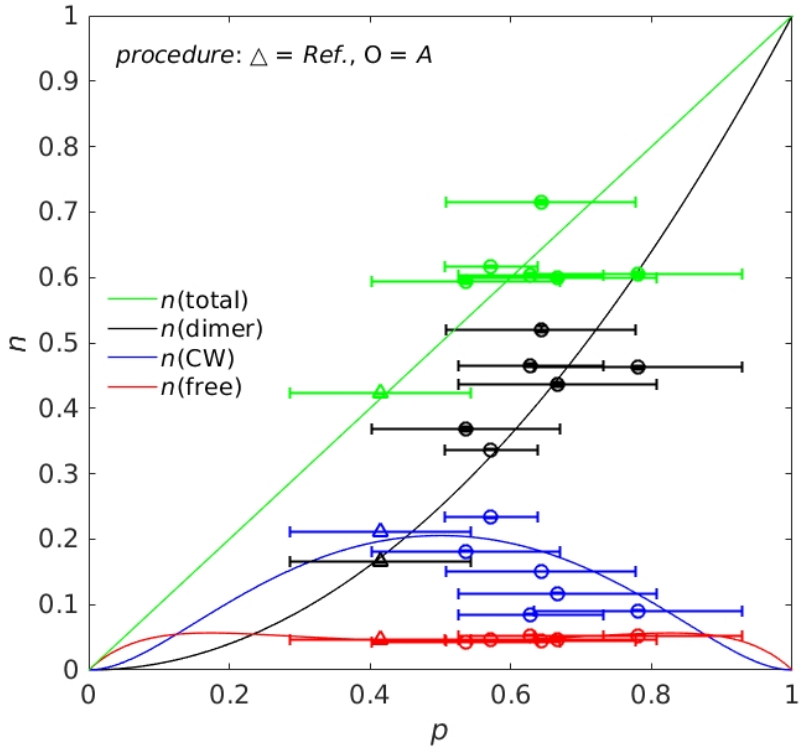

Figure 4.2: The p dependency of the number of spins contributing to the total spins per Mo_3O_{13} cluster, dimer spins, weakly interacting spins, and free spins indicated by green, black, blue, and red colors. The solid lines represents the statistical estimate (Eq. 4.2), while the points with the errorbars are observed data.

4.4 Quantum chemistry molecular orbital calculation of the bilayer dimer

Another support for the bilayer dimer formation may be found in the quantum chemistry calculation, given in the followig. To evaluate the plausibility of a dimer in LZMO we performed molecular orbital calculation utilizing the Unrestricted Hartree-Fock (UHF) theory [46] using the GAMESS software package by modifying the previously published input file [25]. The original input file included a single $Mo_3O_{13}H_{15}$ cluster. We have doubled that cluster into two clusters in the interlayer direction. Figure 4.3 illustrates the two highest occupied molecular orbitals for spin multiplicity 1 (a) $n_\alpha = n_\beta$ and spin multiplicity 3 (b) $n_\alpha = n_\beta + 2$, where α and β refers to spin polarization. In both cases the two highest occupied orbitals have irreducible representation A_1. In the spin multiplicity 1 case the highest occupied alpha and beta orbitals are localized on different clusters,

but in the spin multiplicity 3 case both orbitals are distributed over both clusters. The difference in the final U-PBE0 energy between these two spin multiplicity states are 10 meV which suggests that the oxygen orbital overlap between the two clusters must be sufficient enough to make the dimer exchange plausible. However, it must be noted here that it is a known fact that the UHF wavefunctions are not exactly eigenfunctions of the square of the spin angular momentum operator $\mathbf{S}^2$ [47]. Therefore, we can only speculate that the multiplicities 1 and 3 corresponds roughly to the singlet and triplet ground states, respectively.

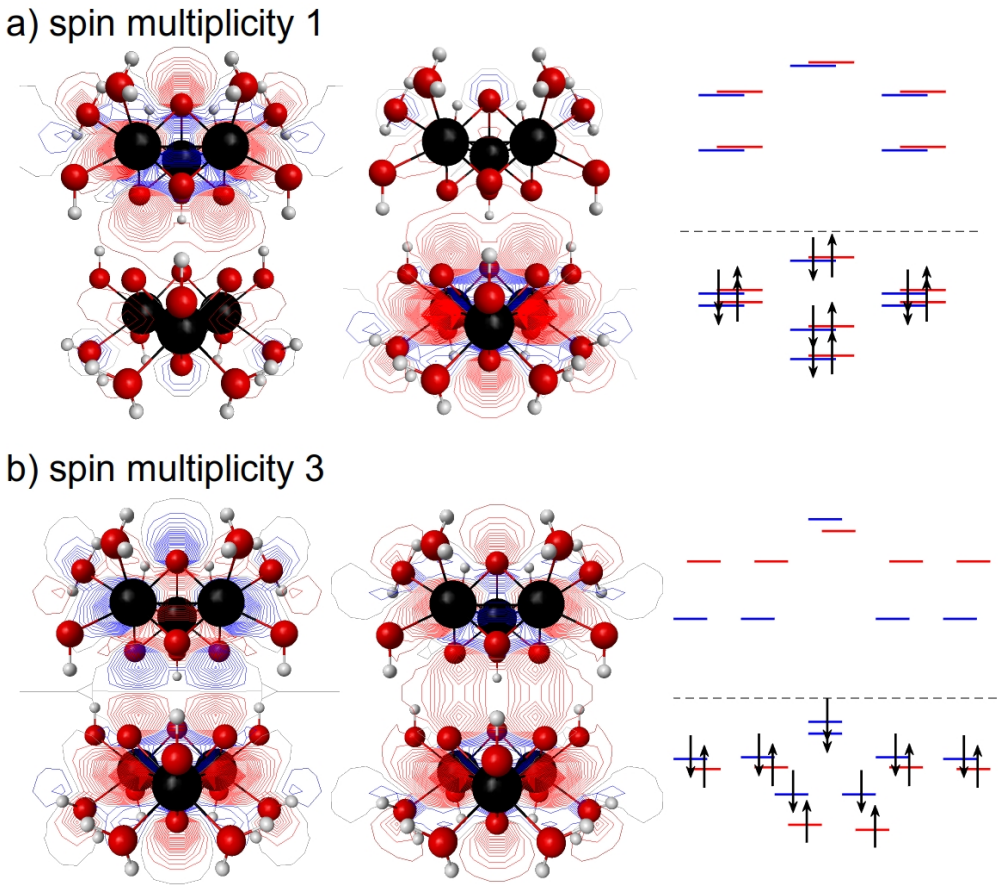

Figure 4.3: From left to right, illustration of the two highest occupied spin polarized molecular orbitals and the spin polarized molecular orbital diagram for $2(Mo_3O_{13}H_{15})$ for the spin multiplicities 1, $n_\alpha = n_\beta$ (a), and 3, $n_\alpha = n_\beta + 2$ (b).

5 Conclusions

We have revisited the solid-state-reaction of LZMO to achieve the control of stoichiometry of Li and Zn. By including MoO_3 as a starting material we were able to suppress the secondary phase formation which allowed us to control the Li and Zn concentrations in the primary phase. We synthesized several compounds with varying unpaired spin 1/2 concentration p. The best sample becomes much closer to the ideal composition as $p = 0.78(15)$.

The magnetic properties were investigated using samples with a wide spin concentration range $0.4 < p < 0.8$. The temperature dependence of the magnetic susceptibility is well explained by the three-component model newly introduced in the present work, which consists of the non-interacting (Curie law), weakly-interacting (Curie-Weiss law), and dimer-forming spins coexisting in the sample. Together with utilizing isothermal magnetization, the three components in the magnetic susceptibility can be unambiguously fitted. This three-magnetic-component model can reproduce the two-Curie-Weiss regions reported by earlier work (samples $p < 0,6$) and the broad peak from the dimer susceptibility (samples $p > 0.6$) newly discovered in the present study. The magnetic susceptibility data suggest that the number of weakly correlating and non-correlating spins contributing to the low-T susceptibility decreases as p becomes closer to unity, while the spins contributing to dimer formation increase. This strongly suggests that the intrinsic magnetism (at $p = 1$) for LZMO may be singlet dimer formation, instead of the putative condensed valence-bond state or the plaquette charge ordered state. We also found that the number of spin magnetic moments contributing to these three magnetic components consistently total to that evaluated in our chemistry work. ESR and specific heat measurements were qualitalively consistent with the three-component model. Two ESR resonant peaks can be distinquished at $T < 70\,\mathrm{K}$ identified as the non-interacting and weakly-interacting spins. Specific heat measurement performed with the best composition LZMO sample below $T < 5\,\mathrm{K}$ indicates that the magnetic upturn previously observed is

reduced by a factor of 1.5. This suggests that the magnetic contributions in the low-T region are reduced by improving the stoichiometry of LZMO.

The neutron inelastic scattering experiments have been performed using three different neutron spectrometers aiming at measuring different $\hbar\omega$-Q space with appropriate Q and $\hbar\omega$ resolutions. The results were described in Chapt. 3.3. The neutron inelastic scattering function $S(Q, \hbar\omega)$ in widest Q-$\hbar\omega$ space was measured using the High Resolution Chopper spectrometer (HRC). With the large incident neutron energy $E_{\rm i} = 311\,{\rm meV}$, together with the very unique small angle detectors down to $2\theta = 0.6°$, we could cover very large Q-$\hbar\omega$ space with reasonably good energy resolution. In the high-Q range measured by the normal detector banks of HRC, we found that the inelastic scattering is dominated by the phonon contribution; a clear increasing intensity was confirmed as Q becomes larger, a typical Q-dependence of the phonon scattering. On the other hand, in the low-Q region measured by the small angle detectors, we clearly see remaining inelastic component around $\hbar\omega = 20\,{\rm meV}$. The scattering intensity at the peak position $\hbar\omega = 20\,{\rm meV}$ is almost the same between the room temperature and the base temperature, whereas the intensity below $\hbar\omega < 20\,{\rm meV}$ decreases significantly, possibly indicating gap formation. By correcting the detailed-balance factor for the neutron inelastic scattering, clear enhancement of the dynamical susceptibility can be envisaged from the data in the low-Q region ($Q < 1\,{\rm \AA}^{-1}$). From the temperature dependence and the peak energy position, we speculate that this inelastic response at 20 meV may be related to the singlet-triplet excitation in the singlet dimer proposed from the magnetic susceptibility study.

It may be noted that the inelastic spectrum observed at $T = 1.7K$ using HYSPEC also indicates decreasing scattering intensity for $\hbar\omega < 20\,{\rm meV}$, being consistent with the HRC result. Therefore, it is strongly suggested that such a spin gap formation is an intrinsic feature of the inelastic scattering spectra in LZMO closer to the stoichiometric composition. In addition to the wider $\hbar\omega$-Q range observation, we have performed inelastic (as well as elastic) scattering experiment using polarized neutrons with PTAX. The result indicates clear development of antiferromagnetic correlations with gapless spectra, being consistent with the earlier work. The magnetic origin of the low-energy gapless component was for the first time confirmed by the neutron polarization analysis for the elastic signal. We assigned the low-energy gapless excitations to the weakly interacting spin component.

We have presented the results of inelastic neutron scattering and other techniques that all measured the magnetism in LZMO. The data suggests three magnetic components in the data: two in the low-T region and one in the high-T region. It is strongly suggested

that the singlet dimer formation may be the key intrinsic characteristic of the LZMO in the $p \to 1$ limit. Hence, the origin of the singlet dimer formation is the next issue. For this issue, we proposed that the bilayer triangular lattice structure of LZMO could be the origin of the spin dimer with the interaction between nearest-neighbor sites between the two layers. This idea of forming bilayer dimers is supported by the observation of the absence of dimer formation behavior in the closely related $Li_2ScMo_3O_8$, in which the only significant difference from LZMO is the absence of the bilayer structure. We also performed the quantum chemistry molecular orbital calculations using the GAMESS software package to simulate singlet-triplet excitation energy in the two interacting $Mo_3O_{13}H_{15}$ clusters aligned in the bilayer direction (the c-axis). We found that the difference in the final U-PBE0 energy between the spin multiplicity 3 ($n_\alpha = n_\beta + 2$) state and the spin multiplicity 1 ($n_\alpha = n_\beta$) state was approximately 10 meV. This could provide a further calculational support that a dimer exchange coupling is plausible between bilayer Mo_3O_{13} clusters.

6 Acknowledgments

I would like to express my deepest gratitude to my research supervisor Prof. T. J Sato at the Institute of Multidisciplinary Research for Advanced Materials (IMRAM), Tohoku University, for his continued help, encouragement and advice throughout the course of this research.

I am especially thankful to Prof. S. Itoh at Institute of Materials Structure Science (IMSS), High Energy Accelerator Research Organization (KEK), Dr. B. Winn and Dr. M. Matsuda at Oak Ridge National Laboratory (ORNL), and Dr. M. Avdeev at Australian Nuclear Science and Technology Organization (ANSTO) for their kind help in the neutron scattering and diffraction experiments.

I would also like to express my sincere thanks to Prof. H. Nojiri at Institute for Materials Research (IMR), Tohoku University, for his kind guidance and advise for the high magnetic field and ESR experiments.

I would like to offer my special thanks to Prof. H. Yoshizawa and Dr. M. Yoshida at The Institute for Solid State Physics (ISSP), The University of Tokyo, for their assistance in measuring the specific heat.

I am particularly grateful for the valuable advice and technical assistance during the sample synthesis, magnetization measurements, and the neutron experiments given by Dr. D. Okuyama and Dr. K. Nawa at IMRAM, Tohoku University.

I would also like to thank my family for their constant encouragement and supports.

Finally, I would like to thank the Almighty God for His blessing of giving me the opportunity and sufficient abilities to undertake this research, and for being my motivation to pursue science.

7 List of Publications

I K. E. Sandvik, D. Okuyama, K. Nawa, M. Avdeev and T. J Sato, "Controlling the stoichiometry of the triangular lattice antiferromagnet $Li_{1+x}Zn_{2-y}Mo_3O_8$," *Journal of Solid State Chemistry*, vol 271, pages 216 – 221, March 2019.

II K. E. Sandvik, et al., "Neutron scattering datasets from HRC, PTAX, and HYSPEC" *In preparation.*

Bibliography

[1] L. Balents, "Spin liquids in frustrated magnets," *Nature*, vol. 464, pp. 199–208, 2010. [Online]. Available: https://doi.org/10.1038/nature08917

[2] G. H. Wannier, "Antiferromagnetism. The triangular Ising net," *Phys. Rev.*, vol. 79, pp. 357–364, 1950. [Online]. Available: https://link.aps.org/doi/10.1103/PhysRev.79.357

[3] P. Anderson, "Resonating valence bonds: A new kind of insulator?" *Materials Research Bulletin*, vol. 8, pp. 153–160, 1973. [Online]. Available: http://www.sciencedirect.com/science/article/pii/0025540873901670

[4] D. A. Huse and V. Elser, "Simple variational wave functions for two-dimensional Heisenberg spin-1/2 antiferromagnets," *Phys. Rev. Lett.*, vol. 60, pp. 2531–2534, 1988. [Online]. Available: https://link.aps.org/doi/10.1103/PhysRevLett.60.2531

[5] B. Bernu, C. Lhuillier, and L. Pierre, "Signature of Néel order in exact spectra of quantum antiferromagnets on finite lattices," *Phys. Rev. Lett.*, vol. 69, pp. 2590–2593, 1992. [Online]. Available: https://link.aps.org/doi/10.1103/PhysRevLett.69.2590

[6] L. Capriotti, A. E. Trumper, and S. Sorella, "Long-range Néel order in the triangular Heisenberg model," *Phys. Rev. Lett.*, vol. 82, pp. 3899–3902, 1999. [Online]. Available: https://link.aps.org/doi/10.1103/PhysRevLett.82.3899

[7] Y. Iqbal, W.-J. Hu, R. Thomale, D. Poilblanc, and F. Becca, "Spin liquid nature in the Heisenberg $J_1 - J_2$ triangular antiferromagnet," *Phys. Rev. B*, vol. 93, p. 144411, 2016. [Online]. Available: https://link.aps.org/doi/10.1103/PhysRevB.93.144411

[8] A. E. Trumper, "Spin-wave analysis to the spatially anisotropic Heisenberg antiferromagnet on a triangular lattice," *Phys. Rev. B*, vol. 60, pp. 2987–2989, 1999. [Online]. Available: https://link.aps.org/doi/10.1103/PhysRevB.60.2987

[9] K. Watanabe, H. Kawamura, H. Nakano, and T. Sakai, "Quantum spin-liquid behavior in the spin-1/2 random Heisenberg antiferromagnet on the triangular lattice," *J. Phys. Soc. Jpn.*, vol. 83, no. 3, p. 034714, 2014. [Online]. Available: https://doi.org/10.7566/JPSJ.83.034714

[10] H. Morita, S. Watanabe, and M. Imada, "Nonmagnetic insulating states near the Mott transitions on lattices with geometrical frustration and implications for κ-$(ET)_2Cu_2(CN)_3$," *J. Phys. Soc. Jpn.*, vol. 71, no. 9, pp. 2109–2112, 2002. [Online]. Available: https://doi.org/10.1143/JPSJ.71.2109

[11] B. Kyung and A.-M. S. Tremblay, "Mott transition, antiferromagnetism, and d-wave superconductivity in two-dimensional organic conductors," *Phys. Rev. Lett.*, vol. 97, p. 046402, 2006. [Online]. Available: https://link.aps.org/doi/10.1103/PhysRevLett.97.046402

[12] T. Yoshioka, A. Koga, and N. Kawakami, "Quantum phase transitions in the Hubbard model on a triangular lattice," *Phys. Rev. Lett.*, vol. 103, p. 036401, 2009. [Online]. Available: https://link.aps.org/doi/10.1103/PhysRevLett.103.036401

[13] H.-Y. Yang, A. M. Läuchli, F. Mila, and K. P. Schmidt, "Effective spin model for the spin-liquid phase of the Hubbard model on the triangular lattice," *Phys. Rev. Lett.*, vol. 105, p. 267204, 2010. [Online]. Available: https://link.aps.org/doi/10.1103/PhysRevLett.105.267204

[14] O. I. Motrunich, "Variational study of triangular lattice spin-1/2 model with ring exchanges and spin liquid state in κ-$(ET)_2Cu_2(CN)_3$," *Phys. Rev. B*, vol. 72, p. 045105, 2005. [Online]. Available: https://link.aps.org/doi/10.1103/PhysRevB.72.045105

[15] S.-S. Lee and P. A. Lee, "U(1) gauge theory of the Hubbard model: Spin liquid states and possible application to κ-$(BEDT\text{-}TTF)_2Cu_2(CN)_3$," *Phys. Rev. Lett.*, vol. 95, p. 036403, 2005. [Online]. Available: https://link.aps.org/doi/10.1103/PhysRevLett.95.036403

[16] Y. Shimizu, K. Miyagawa, K. Kanoda, M. Maesato, and G. Saito, "Spin liquid state in an organic Mott insulator with a triangular lattice," *Phys. Rev. Lett.*, vol. 91, p. 107001, 2003. [Online]. Available: https://link.aps.org/doi/10.1103/PhysRevLett.91.107001

[17] Y. Haraguchi, C. Michioka, M. Imai, H. Ueda, and K. Yoshimura, "Spin-liquid behavior in the spin-frustrated Mo_3 cluster magnet $Li_2ScMo_3O_8$ in contrast to

magnetic ordering in isomorphic $Li_2InMo_3O_8$," *Phys. Rev. B*, vol. 92, p. 014409, 2015. [Online]. Available: https://link.aps.org/doi/10.1103/PhysRevB.92.014409

[18] Y. Haraguchi, C. Michioka, H. Ueda, A. Matsuo, K. Kindo, and K. Yoshimura, "Physical properties in the cluster-based magnetic-diluted triangular lattice antiferromagnets $Li_2Sc_{1-x}Sn_xMo_3O_8$," *J. Phys. Conf. Ser.*, vol. 828, p. 012013, 2017. [Online]. Available: https://doi.org/10.1088/1742-6596/828/1/012013

[19] A. Akbari-Sharbaf, R. Sinclair, A. Verrier, D. Ziat, H. D. Zhou, X. F. Sun, and J. A. Quilliam, "Tunable quantum spin liquidity in the 1/6th-filled breathing kagome lattice," *Phys. Rev. Lett.*, vol. 120, p. 227201, 2018. [Online]. Available: https://link.aps.org/doi/10.1103/PhysRevLett.120.227201

[20] K. Iida, H. Yoshida, H. Okabe, N. Katayama, Y. Ishii, A. Koda, Y. Inamura, N. Mura, M. Ishikado, R. Kadono, and R. Kajimoto, "Quantum magnetisms in uniform triangular lattices $Li_2AMo_3O_8$ (A = In, Sc)," *Sci. Rep.*, vol. 9, 1826, 2019. [Online]. Available: https://doi.org/10.1038/s41598-018-36123-7

[21] Y. Haraguchi, C. Michioka, H. Ueda, and K. Yoshimura, "Highly spin-frustrated magnetism in the topochemically prepared triangular lattice cluster magnets $Na_3A_2(MoO_4)_2Mo_3O_8$ (A = In, Sc)," *Chem.: Eur. J.*, vol. 23, no. 63, pp. 15 879 – 15 883, 2017. [Online]. Available: https://onlinelibrary.wiley.com/doi/abs/10.1002/chem.201703597

[22] J. P. Sheckelton, K. W. Plumb, B. A. Trump, C. L. Broholm, and T. M. McQueen, "Rearrangement of van der Waals stacking and formation of a singlet state at T = 90 K in a cluster magnet," *Inorg. Chem. Front.*, vol. 4, pp. 481 – 490, 2017. [Online]. Available: http://dx.doi.org/10.1039/C6QI00470A

[23] Y. Haraguchi, C. Michioka, M. Ishikawa, Y. Nakano, H. Yamochi, H. Ueda, and K. Yoshimura, "Magnetic – nonmagnetic phase transition with interlayer charge disproportionation of Nb_3 trimers in the cluster compound Nb_3Cl_8," *Inorg. Chem.*, vol. 56, no. 6, pp. 3483 – 3488, 2017. [Online]. Available: https://doi.org/10.1021/acs.inorgchem.6b03028

[24] C. C. Torardi and R. E. McCarley, "Synthesis, crystal structures, and properties of lithium zinc molybdenum oxide ($LiZn_2Mo_3O_8$), zinc molybdenum oxide ($Zn_3Mo_3O_8$), and scandium zinc molybdenum oxide ($ScZnMo_3O_8$), reduced derivatives containing the Mo_3O_{13} cluster unit," *Inorg. Chem.*, vol. 24, no. 4, pp. 476 – 481, 1985. [Online]. Available: https://doi.org/10.1021/ic00198a009

[25] J. P. Sheckelton, J. R. Neilson, D. G. Soltan, and T. M. McQueen, "Possible valence-bond condensation in the frustrated cluster magnet $LiZn_2Mo_3O_8$," *Nat. Mater.*, vol. 11, no. 6, pp. 493–496, 2012. [Online]. Available: https://doi.org/10.1038/nmat3329

[26] R. Flint and P. A. Lee, "Emergent honeycomb lattice in $LiZn_2Mo_3O_8$," *Phys. Rev. Lett.*, vol. 111, p. 217201, 2013. [Online]. Available: https://link.aps.org/doi/10.1103/PhysRevLett.111.217201

[27] M. Mourigal, W. T. Fuhrman, J. P. Sheckelton, A. Wartelle, J. A. Rodriguez-Rivera, D. L. Abernathy, T. M. McQueen, and C. L. Broholm, "Molecular quantum magnetism in $LiZn_2Mo_3O_8$," *Phys. Rev. Lett.*, vol. 112, p. 027202, 2014. [Online]. Available: https://link.aps.org/doi/10.1103/PhysRevLett.112.027202

[28] J. P. Sheckelton, F. R. Foronda, L. Pan, C. Moir, R. D. McDonald, T. Lancaster, P. J. Baker, N. P. Armitage, T. Imai, S. J. Blundell, and T. M. McQueen, "Local magnetism and spin correlations in the geometrically frustrated cluster magnet $LiZn_2Mo_3O_8$," *Phys. Rev. B*, vol. 89, p. 064407, 2014. [Online]. Available: https://link.aps.org/doi/10.1103/PhysRevB.89.064407

[29] J. P. Sheckelton, J. R. Neilson, and T. M. McQueen, "Electronic tunability of the frustrated triangular-lattice cluster magnet $LiZn_{2-x}Mo_3O_8$," *Mater. Horiz.*, vol. 2, pp. 76–80, 2015. [Online]. Available: http://dx.doi.org/10.1039/C4MH00166D

[30] G. Chen, H.-Y. Kee, and Y. B. Kim, "Cluster Mott insulators and two Curie-Weiss regimes on an anisotropic kagome lattice," *Phys. Rev. B*, vol. 93, p. 245134, 2016. [Online]. Available: https://link.aps.org/doi/10.1103/PhysRevB.93.245134

[31] Y. Haraguchi, C. Michioka, H. Ueda, and K. Yoshimura, "Charge fluctuation in $S = 1/2$ triangular lattice cluster antiferromagnets $Li_2ScMo_3O_8$ and $Li_2InMo_3O_8$," *J. Phys. Conf. Ser.*, vol. 868, p. 012022, 2017. [Online]. Available: https://doi.org/10.1088%2F1742-6596%2F868%2F1%2F012022

[32] J. Carrasquilla, G. Chen, and R. G. Melko, "Tripartite entangled plaquette state in a cluster magnet," *Phys. Rev. B*, vol. 96, p. 054405, 2017. [Online]. Available: https://link.aps.org/doi/10.1103/PhysRevB.96.054405

[33] G. Chen and P. A. Lee, "Emergent orbitals in the cluster Mott insulator on a breathing kagome lattice," *Phys. Rev. B*, vol. 97, p. 035124, 2018. [Online]. Available: https://link.aps.org/doi/10.1103/PhysRevB.97.035124

[34] C. Salter, "Error analysis using the variance-covariance matrix," *J. Chem. Educ.*, vol. 77, no. 9, p. 1239, 2000. [Online]. Available: https://doi.org/10.1021/ed077p1239

[35] K.-D. Liss, B. Hunter, M. Hagen, T. Noakes, and S. Kennedy, "Echidna—the new high-resolution powder diffractometer being built at OPAL," *Physica B Condens. Matter*, vol. 385-386, pp. 1010 – 1012, 2006. [Online]. Available: http://www.sciencedirect.com/science/article/pii/S0921452606012233

[36] J. Rodríguez-Carvajal, "Recent developments of the program Fullprof," *Commission on powder diffraction (IUCr)*, vol. 26, pp. 12–19, 2001.

[37] J. Cuny, P. Gougeon, and P. Gall, "Redetermination of $Zn_2Mo_3O_8$," *Acta Crystallogr. E*, vol. 65, no. 7, p. i51, 2009. [Online]. Available: https://doi.org/10.1107/S1600536809021928

[38] R. C. Jaklevic, J. Lambe, A. H. Silver, and J. E. Mercereau, "Quantum interference effects in Josephson tunneling," *Phys. Rev. Lett.*, vol. 12, pp. 159–160, 1964. [Online]. Available: https://link.aps.org/doi/10.1103/PhysRevLett.12.159

[39] M. McElfresh, S. Li, and R. Sager, "Effects of magnetic field uniformity on the measurement of superconducting samples," *technical report*, 1996.

[40] S. Itoh, T. Yokoo, S. Satoh, S. ichiro Yano, D. Kawana, J. Suzuki, and T. J. Sato, "High Resolution Chopper spectrometer (HRC) at J-PARC," *Nucl. Instrum. Meth. A*, vol. 631, no. 1, pp. 90 – 97, 2011. [Online]. Available: https://doi.org/10.1016/j.nima.2010.11.107

[41] S. Itoh, T. Yokoo, D. Kawana, H. Yoshizawa, T. Masuda, M. Soda, T. J. Sato, S. Satoh, M. Sakaguchi, and S. Muto, "Progress in High Resolution Chopper spectrometer, HRC," *J. Phys. Soc. Jpn.*, vol. 82, no. Suppl.A, p. SA033, 2013. [Online]. Available: https://doi.org/10.7566/JPSJS.82SA.SA033

[42] S. Itoh and Y. Endoh, "Neutron Brillouin scattering and low-Q dynamics in condensed matter," *J. Phys. Soc. Jpn.*, vol. 88, no. 8, p. 081004, 2019. [Online]. Available: https://doi.org/10.7566/JPSJ.88.081004

[43] Winn, Barry, Filges, Uwe, Garlea, V. Ovidiu, Graves-Brook, Melissa, Hagen, Mark, Jiang, Chenyang, Kenzelmann, Michel, Passell, Larry, Shapiro, Stephen M., Tong, Xin, and Zaliznyak, Igor, "Recent progress on HYSPEC, and its polarization analysis capabilities," *EPJ Web Conf.*, vol. 83, p. 03017, 2015. [Online]. Available: https://doi.org/10.1051/epjconf/20158303017

[44] O. Arnold, J. Bilheux, J. Borreguero, A. Buts, S. Campbell, L. Chapon, M. Doucet, N. Draper, R. F. Leal, M. Gigg, V. Lynch, A. Markvardsen, D. Mikkelson, R. Mikkelson, R. Miller, K. Palmen, P. Parker, G. Passos, T. Perring, P. Peterson, S. Ren, M. Reuter, A. Savici, J. Taylor, R. Taylor, R. Tolchenov, W. Zhou, and J. Zikovsky, "Mantid—data analysis and visualization package for neutron scattering and μSR experiments," *Nucl. Instrum. Meth. A*, vol. 764, pp. 156 – 166, 2014. [Online]. Available: http://www.sciencedirect.com/science/article/pii/S0168900214008729

[45] B. Bleaney and K. D. Bowers, "Anomalous paramagnetism of copper acetate," *Proc. Roy. Soc. London A*, vol. 214, no. 1119, pp. 451–465, 1952. [Online]. Available: https://royalsocietypublishing.org/doi/abs/10.1098/rspa.1952.0181

[46] J. A. Pople and R. K. Nesbet, "Self-consistent orbitals for radicals," *J. Chem. Phys.*, vol. 22, no. 3, pp. 571–572, 1954. [Online]. Available: https://doi.org/10.1063/1.1740120

[47] T. Amos and L. C. Snyder, "Unrestricted Hartree-Fock calculations. I. an improved method of computing spin properties," *J. Chem. Phys.*, vol. 41, no. 6, pp. 1773–1783, 1964. [Online]. Available: https://doi.org/10.1063/1.1726157

Appendix A: X-ray and neutron powder diffraction data and results of Rietveld fitting combined with the ICP elemental analysis

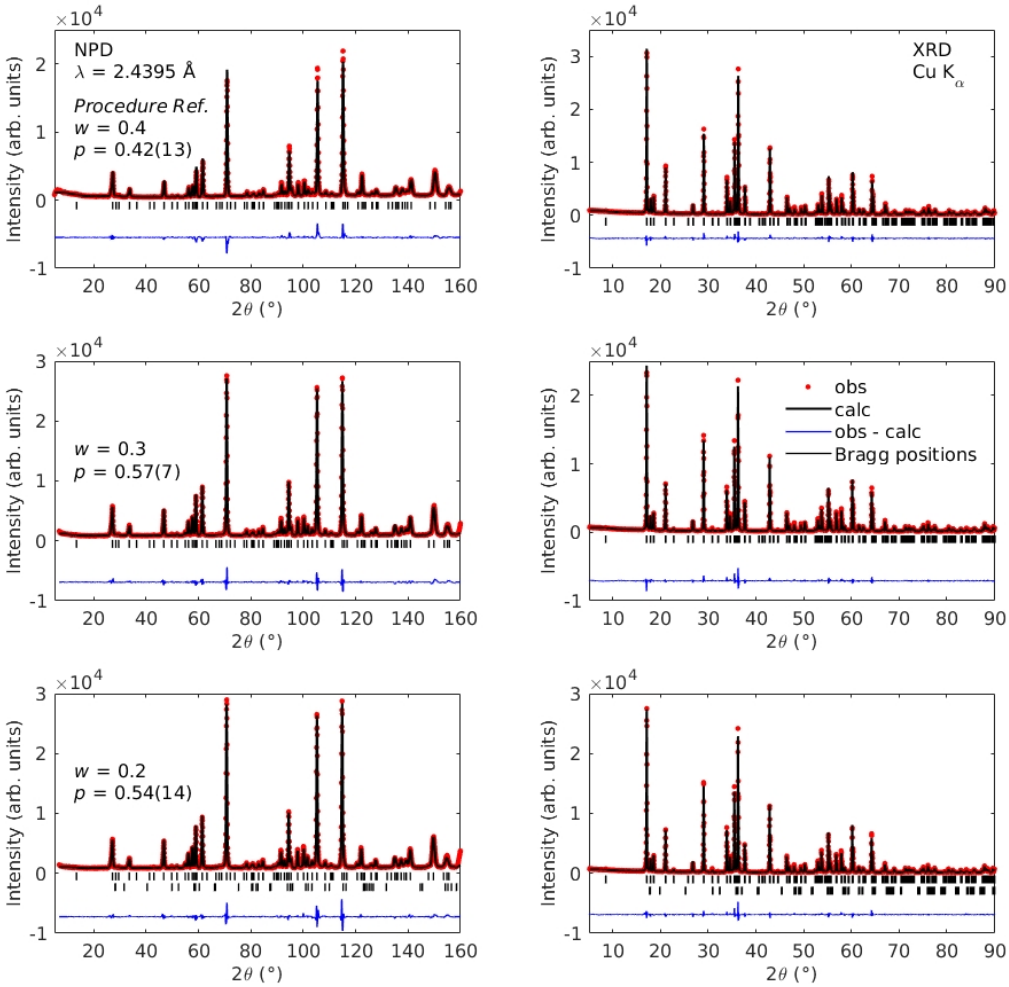

Figure 1: Combined Rietveld analysis on $Li_{1+x}Zn_{2-y}Mo_3O_8$ for $p = 0.42(13)$, 0.57(7), and 0,54(14) (from top to bottom panels, respectively) from high resolution powder diffraction at 300 K on ECHIDNA (left panels) and x-ray diffraction patterns (right panels). The bottom blue lines give the difference between the observed (red dots) and calculated (black line) intensities. Bragg positions are shown as vertical bars in the upper and lower row for the primary and secondary phase, respectively.

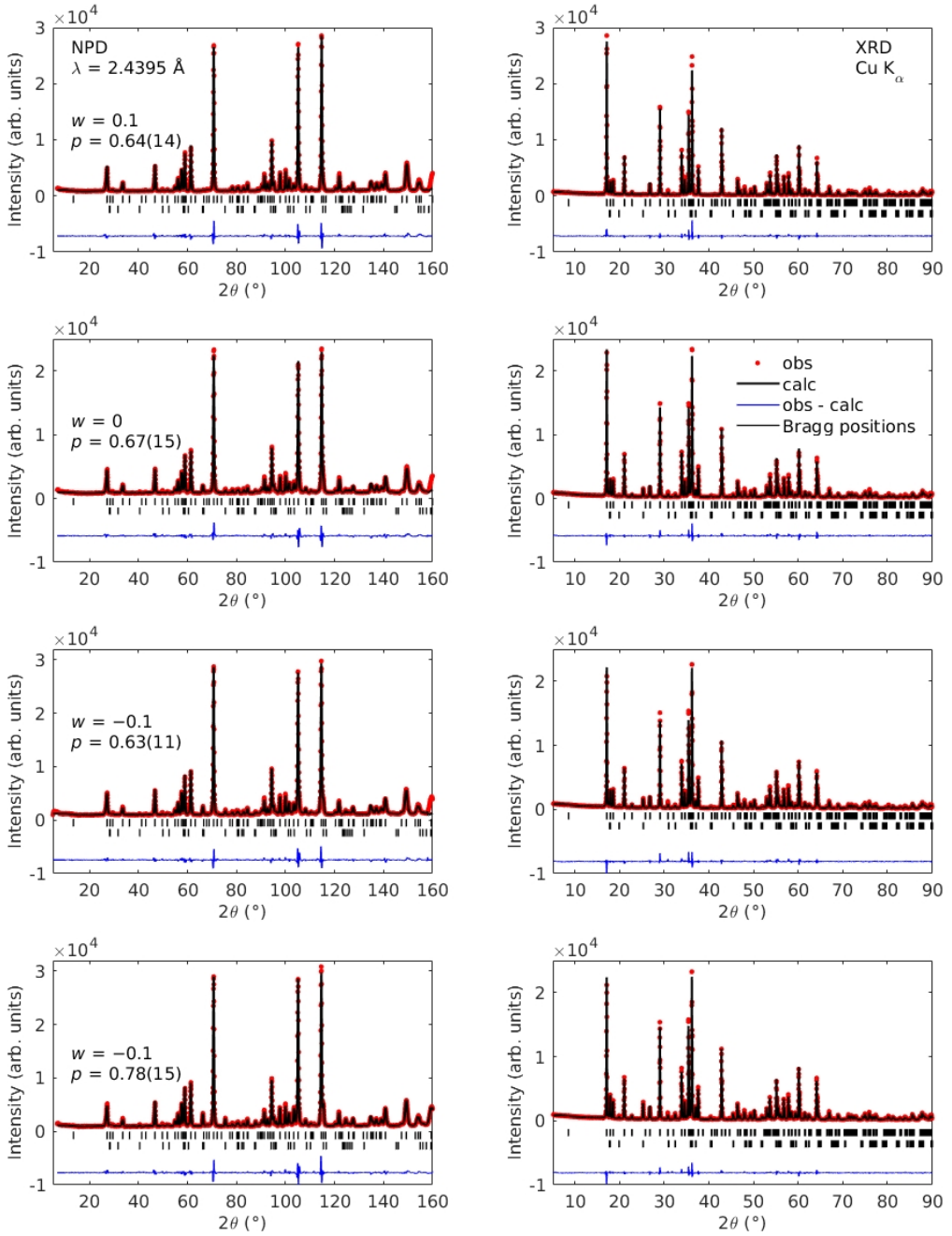

Figure 2: Combined Rietveld analysis on $Li_{1+x}Zn_{2-y}Mo_3O_8$ for $p = 0.64(14)$, 0.67(15), 0.63(11), and 0.78(15) (from top to bottom panels, respectively) from high resolution powder diffraction at 300 K on ECHIDNA (left panels) and x-ray diffraction patterns (right panels). The bottom blue lines give the difference between the observed (red dots) and calculated (black line) intensities. Bragg positions are shown as vertical bars in the upper and lower row for the primary and secondary phase, respectively.

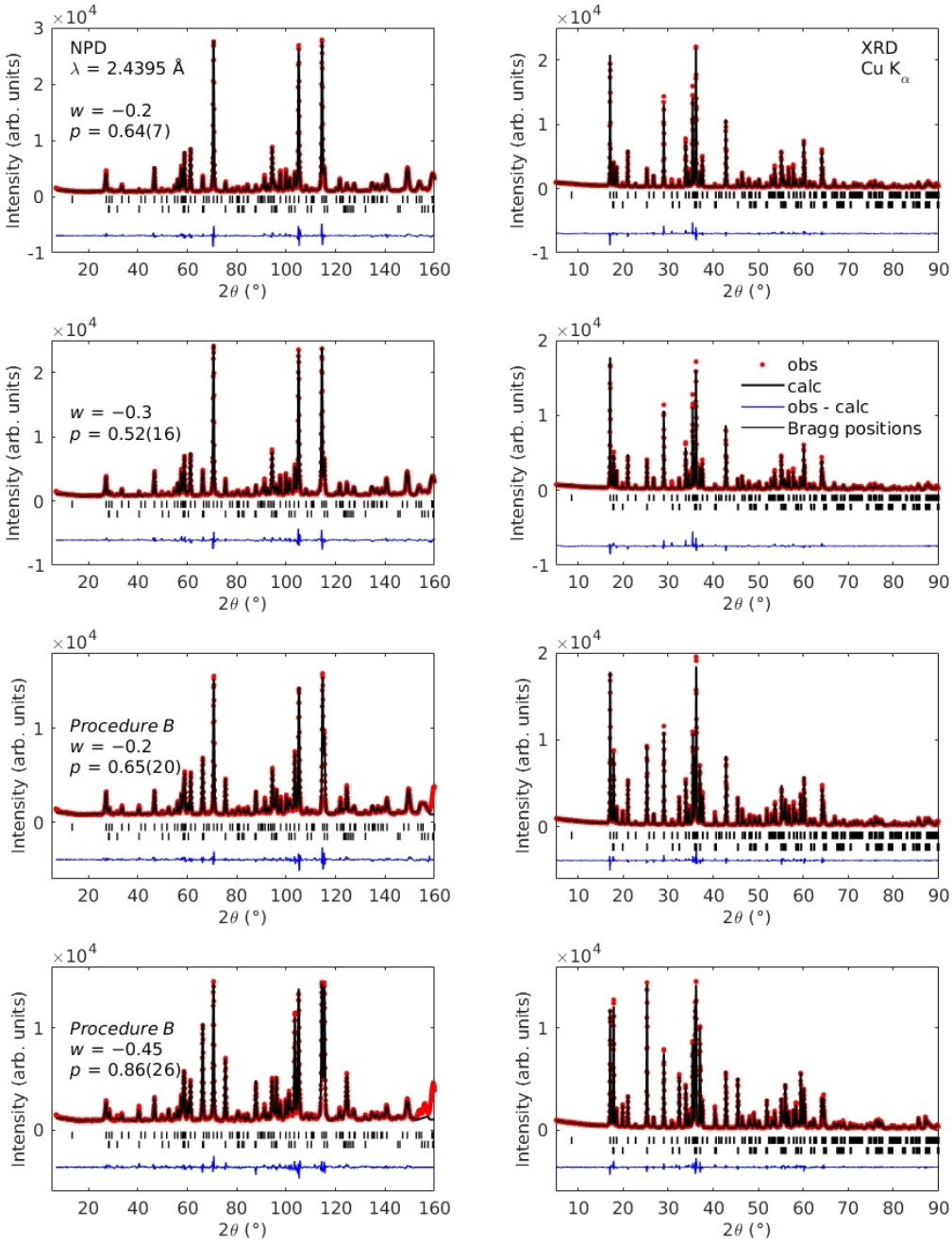

Figure 3: Combined Rietveld analysis on $Li_{1+x}Zn_{2-y}Mo_3O_8$ for $p = 0.64(7)$, 0.52(16), 0.65(20), and 0.86(26) (from top to bottom panels, respectively) from high resolution powder diffraction at 300 K on ECHIDNA (left panels) and x-ray diffraction patterns (right panels). The bottom blue lines give the difference between the observed (red dots) and calculated (black line) intensities. Bragg positions are shown as vertical bars in the upper and lower row for the primary and secondary phase, respectively.

Table 1: Tabulated values for the occupation of Li and Zn sites for all LZMO samples in the range $-0.45 \leq w \leq 4$ and $0.4 < p < 0.8$.

procedure		*Ref*	*A*	*A*	*A*	*A*	*A*
w		0.4	0.3	0.2	0.1	0	−0.1
p		0.42(13)	0.57(7)	0.54(14)	0.64(14)	0.67(15)	0.63(11)
Atom, i	Site			occupancy			
Li1	6c	0.09(3)	0.01(3)	0.00(3)	−0.01(3)	−0.01(3)	0.00(3)
Li2	6c	0.41(3)	0.34(3)	0.27(3)	0.12(3)	0.23(3)	0.18(3)
Li3	3a	0.77(5)	0.78(5)	0.68(4)	0.63(4)	0.61(5)	0.56(4)
Li4	6c	0.51(3)	0.56(3)	0.52(3)	0.48(3)	0.50(3)	0.45(2)
Li5	6c	0.029(18)	−0.003(18)	0.037(17)	0.141(19)	−0.004(19)	−0.001(16)
Zn1	6c	0.850(4)	0.876(4)	0.879(4)	0.910(4)	0.911(4)	0.911(4)
Zn2	6c	0.594(4)	0.664(4)	0.685(4)	0.736(4)	0.746(4)	0.743(4)
Zn3	3a	0.087(6)	0.150(6)	0.188(6)	0.219(6)	0.249(7)	0.304(6)
Zn4	6c	0.012(3)	0.026(3)	0.030(3)	0.045(3)	0.045(3)	0.053(3)
procedure		*A*	*A*	*A*	*B*	*B*	
w		−0.1	−0.2	−0.3	−0.2	−0.45	
p		0.78(15)	0.64(7)	0.52(16)	0.65(20)	0.86(26)	
Atom, i	Site			occupancy			
Li1	6c	0.00(3)	0.00(3)	0.00(3)	−0.01(4)	−0.01(5)	
Li2	6c	0.25(3)	0.19(3)	0.17(3)	0.26(4)	0.17(5)	
Li3	3a	0.48(4)	0.49(5)	0.41(5)	0.68(8)	0.64(8)	
Li4	6c	0.48(2)	0.42(2)	0.45(3)	0.45(3)	0.39(4)	
Li5	6c	−0.003(16)	−0.003(17)	−0.002(20)	0.000(20)	0.000(20)	
Zn1	6c	0.933(4)	0.909(4)	0.884(5)	0.919(5)	0.948(6)	
Zn2	6c	0.759(4)	0.747(4)	0.732(5)	0.728(5)	0.773(6)	
Zn3	3a	0.323(6)	0.347(6)	0.330(7)	0.234(8)	0.367(10)	
Zn4	6c	0.063(3)	0.069(3)	0.076(4)	0.045(4)	0.094(5)	

Appendix B: Details of the quantum chemistry calculation

The GAMESS input files to calculate the molecular orbitals for two $Mo_3O_4(OH)_3$ $(H_2O)_6$ clusters in the bilayer c-direction for spin multiplicity 1 and 3 are presented below. Unrestricted Hartree–Fock density functional theory is used with the PBE0 hybrid functionals. These input files are based on the input file by Sheckelton [25] for a single $Mo_3O_4(OH)_3$ $(H_2O)_6$ cluster.

```
!Multiplicity 1-------------------------------------------------
!
 $CONTRL SCFTYP=UHF RUNTYP=energy MAXIT=200 ICHARG=0 MULT=1
         COORD=UNIQUE UNITS=ANGS EXETYP=RUN DFTTYP=PBE0 $END
 $SYSTEM TIMLIM=525600 MEMORY=10000000 $END
 $BASIS GBASIS=MINI $END
 $GUESS GUESS=HUCKEL MIX=.TRUE. $END
 $SCF DIRSCF=.TRUE. FDIFF=.FALSE. SOSCF=.TRUE. DAMP=.TRUE. $END
 $DATA
2(Mo3O4(OH)3(H2O)6)
Cnv 3
0.0 0.0 0.0 0.0 0.0 1.0
1.0 0.0 0.0 'PARALLEL'
MoA 42.0  1.48725  0.00000  2.59117
MoB 42.0 -1.48725  0.00000 -2.59117
O4A  8.0  0.00000  0.00000  4.04529
O4B  8.0  0.00000  0.00000 -4.04529
O2A  8.0 -1.61790  0.00000  1.3274
O2B  8.0  1.61790  0.00000 -1.3274
O3A  8.0  3.35505  0.00000  1.5538
O3B  8.0 -3.35505  0.00000 -1.5538
O1A  8.0  2.57769  1.3475   3.70919
O1B  8.0 -2.57769 -1.3475  -3.70919
H3A  1.0  3.35505  0.00000  0.58411
H3B  1.0 -3.35505  0.00000 -0.58411
H11A 1.0  2.18474  1.17574  4.57886
H11B 1.0 -2.18474 -1.17574 -4.57886
H12A 1.0  2.66704  2.21202  3.27923
H12A 1.0 -2.66704 -2.21202 -3.27923
 $END
!---------------------------------------------------------------
```

```
!Multiplicity 3-----------------------------------------------
!
 $CONTRL SCFTYP=UHF RUNTYP=energy MAXIT=200 ICHARG=0 MULT=3
         COORD=UNIQUE UNITS=ANGS EXETYP=RUN DFTTYP=PBE0 $END
 $SYSTEM TIMLIM=525600 MEMORY=10000000 $END
 $BASIS GBASIS=MINI $END
 $GUESS GUESS=HUCKEL MIX=.TRUE. $END
 $SCF DIRSCF=.TRUE. FDIFF=.FALSE. SOSCF=.TRUE. DAMP=.TRUE. $END
 $DATA
2(Mo3O4(OH)3(H2O)6)
Cnv 3
0.0 0.0 0.0 0.0 0.0 1.0
1.0 0.0 0.0 'PARALLEL'
MoA 42.0  1.48725  0.00000  2.59117
MoB 42.0 -1.48725  0.00000 -2.59117
O4A  8.0  0.00000  0.00000  4.04529
O4B  8.0  0.00000  0.00000 -4.04529
O2A  8.0 -1.61790  0.00000  1.3274
O2B  8.0  1.61790  0.00000 -1.3274
O3A  8.0  3.35505  0.00000  1.5538
O3B  8.0 -3.35505  0.00000 -1.5538
O1A  8.0  2.57769  1.3475   3.70919
O1B  8.0 -2.57769 -1.3475  -3.70919
H3A  1.0  3.35505  0.00000  0.58411
H3B  1.0 -3.35505  0.00000 -0.58411
H11A 1.0  2.18474  1.17574  4.57886
H11B 1.0 -2.18474 -1.17574 -4.57886
H12A 1.0  2.66704  2.21202  3.27923
H12A 1.0 -2.66704 -2.21202 -3.27923
 $END
!-------------------------------------------------------------
```